Exploring Anomalous Charge Storage in Anode Materials for Next-Generation Li Rechargeable Batteries

Hyunwoo Kim,[†] Woosung Choi,[†] Jaesang Yoon,[†] Ji Hyun Um,[†] Wontae Lee,[†] Jaeyeong Kim,[†] Jordi Cabana[‡] and Won-Sub Yoon[*,†]

[†]*Department of Energy Science, Sungkyunkwan University, Suwon 16419, South Korea*

[‡]*Department of Chemistry, University of Illinois at Chicago, Chicago, IL, 60607, USA*

*** Corresponding author:**

E-mail: wsyoon@skku.edu; Postal Address: Prof. Won-Sub Yoon, Department of Energy Science, Sungkyunkwan University. Natural Sciences Campus, 2066, Seobu-ro, Jangan-gu, Suwon-si, Gyeonggi-do, Korea (16419)

ABSTRACT

To advance current Li rechargeable batteries further, tremendous emphasis has been made on the development of anode materials with higher capacities than the widely commercialized graphite. Some of these anode materials exhibit capacities above the theoretical value predicted based on conventional mechanisms of Li storage, namely insertion, alloying and conversion. In addition, in contrast to conventional observations of loss upon cycling, the capacity has been found to increase during repeated cycling in a significant number of cases. As the internal environment in the battery is very complicated and constantly changing, these abnormal charge storage behaviors are caused by diverse reactions. In this review, we will introduce our current understanding of reported reactions accounting for anode capacities exceeding theoretical values. It includes formation/decomposition of electrolyte-derived surface layer, the possibility of additional storage of charge at sharp interfaces between electronic and ionic sinks, redox reactions of Li-containing species, and unconventional activity occurring at structural defects. We will also discuss how the changes in the anode can induce capacity increase upon cycling. With this knowledge, new insights into possible strategies to effectively and sustainably utilize these abnormal charge storage mechanisms to produce vertical leaps in performance of anode materials will be laid out.

1. INTRODUCTION

With constantly growing concerns over the environment and resource sustainability, market demands are pushing the current energy storage technology to much higher levels of performance to fulfill the stringent requirements for devices consuming even greater energy than modern electronics, such as cars or the electricity grid. Li-ion batteries (LIBs) are the most commonly used energy storage devices due to their superior advantages resulting from the unique beneficial properties of Li. As Li has the lowest reduction potential of any element and is the lightest metallic element with small ionic radius, LIBs demonstrate high operating potential and energy/power density. For these reasons, over the past two decades, LIBs have unquestionably conquered the market of energy storage for numerous applications. Li rechargeable batteries were first designed by Whittinghamin 1976, using TiS_2 as cathode and Li metal as anode.[1] However, motivated by serious safety hazards induced by undesirable Li metal dendrite formation on the anode, Yoshino et al. adopted layered $LiCoO_2$ as cathode and graphite as anode in 1987.[2] Then, LIBs with those materials were first commercialized by Sony in 1991. Until now, carbonaceous materials are used as the standard commercial anode owing to their low-cost and favorable safety features, while various kinds of cathode materials are utilized depending on the purpose of the battery.

Carbonaceous materials can theoretically deliver a capacity of 372 mAh g^{-1} based on the reversible Li intercalation to form LiC_6 ($Li^+ + e^- + C_6 \leftrightarrow LiC_6$). To bring Li storage capacity close to the expected value, considerable efforts have been made in controlling morphology (size, shape, pore size, etc.) and crystallinity (amorphous carbon, crystalline graphite). There are several reports announcing the improved electrochemical performance by surface modification,[3] disordered hard carbon,[4,5] nanofiber[6,7] or meso-carbon micro beads,[8] etc. As the capacity of carbonaceous materials is still not satisfactory for demanding applications like

electric vehicles, various anode materials have been extensively investigated as an alternative to overcome current capacity limitations. Representative examples are materials based on conversion or alloying reactions, such as pure metals, metal oxides or other chalcogenides, which exhibit 2–10 times higher capacity compared to the theoretical capacity of graphite.[9–14] However, the reactions of these materials are quite slow and accompanied by a drastic volume change (sometimes expanding up to 300%), which causes progressive cracking, pulverization of the particles and eventually, induces loss of contact between them.[15–18] To overcome such drawbacks, modern anode materials are tailored at the nanoscale to shorten Li diffusion pathways and buffer volume changes during the electrochemical reactions.[19–25]

Interestingly, some nanoscale engineered transition metal compounds exhibit abnormally high capacity, over the theoretical value based on conventional mechanisms, namely insertion, alloying and conversion reactions.[26–29] Furthermore, in certain conditions, another unusual behavior takes place: an increase in capacity during cycling,[30–35] as opposed to the expected loss due to fatigue. This phenomenon will be named “negative fading” as a contrast with capacity fading in this review. While extensively observed at this stage in time, the origin of these abnormal phenomena has not been clearly identified because they arise from more complex reactions related to not only the bulk of the active materials but also interfaces and electrolyte components, which are highly localized and confined in space, increasing chemical complexity. As a result, most of the specific reaction mechanisms are still the object of continued debate. It is often believed that the LIB concept is approaching ite limits, especially in terms of energy density suggesting, the need for so-called “beyond LIB” systems like metal-air and metal-sulfur. However, the close examination of LIBs suggests that it is not the limitation of the concept itself but the limitation of the specific electrode chemistries in it. Consequently, exploring novel electrode materials with new storage mechanisms will give us an opportunity to overcome the current performance limitations.

In this review, we first focus on our understanding of the proposed reactions accounting for extra capacity, and the changes in cell environment that result in capacity increase upon cycling. We then present emerging strategies to effectively and sustainably utilize these novel storage mechanisms. Thus, we expect that this review will provide guidance for developing high-performance electrode materials for next-generation LIBs breaking current barriers in energy density and durability.

2. OVERVIEW ON ABNORMAL CHARGE STORAGE BEHAVIORS

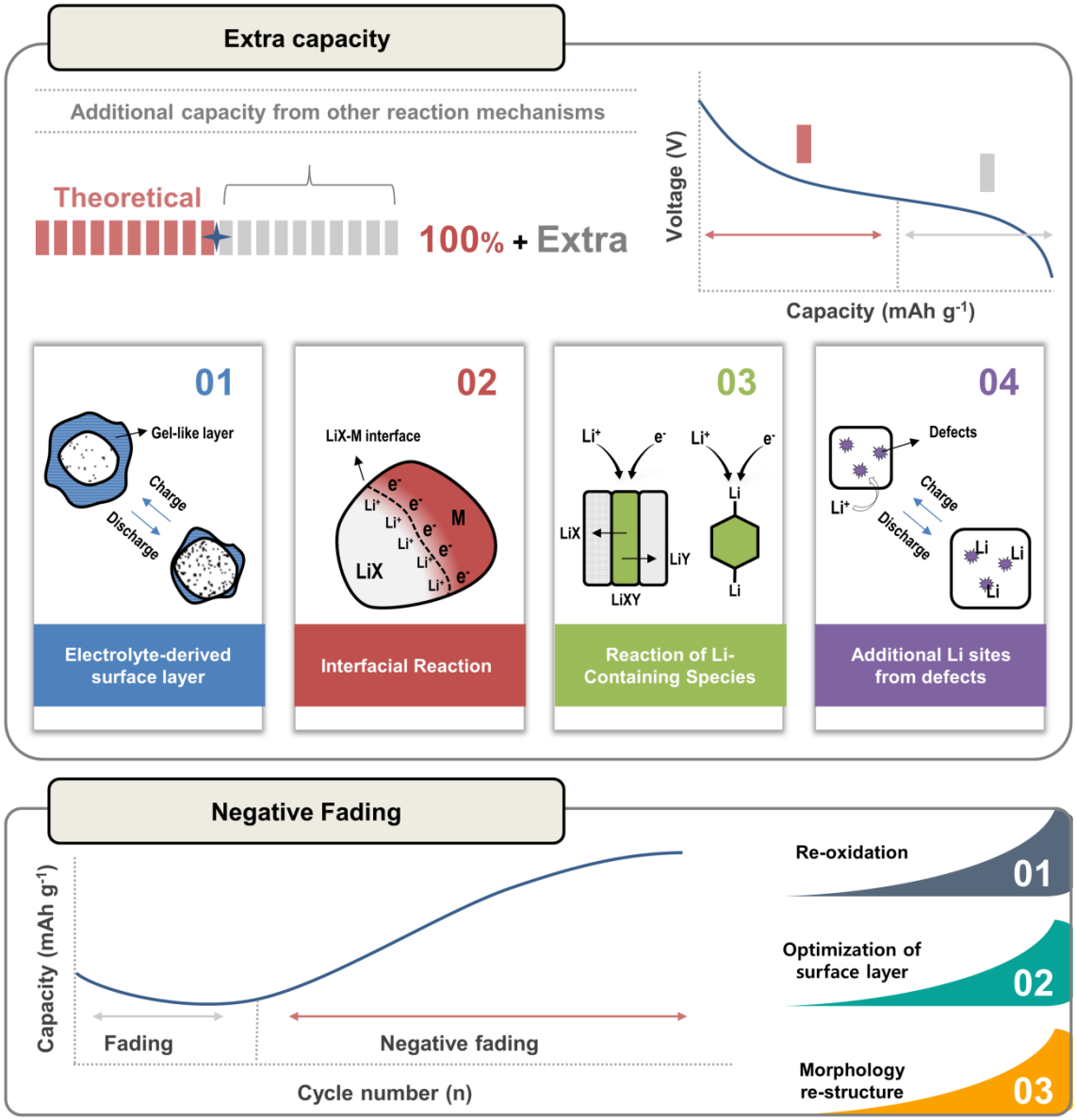

Figure 1. Sketch of two types of abnormal charge storage phenomena in anode materials, extra capacity and negative fading, and proposed origins.

Traditionally, reactions of Li storage in electrode materials are classified into three mechanisms: insertion (or intercalation), alloying and conversion. Lithiation in electrodes based on insertion reactions occurs into available crystallographic sites within their crystal structure ($M_aX_b + nLi^+ + ne^- \leftrightarrow Li_nM_aX_b$). Since the crystal framework is not destroyed or severely re-arranged during the insertion reaction, the reversibility of the reaction is high and, as a result, the cycling performance is relatively stable. However, a low density of active sites

limits the capacity. In alloying reactions, Li can be accommodated with formation of a Li_nM alloy ($M + nLi^+ + ne^- \leftrightarrow Li_nM$), where n depends on the specific M and can be very high (i.e., $n>1$). Lastly, metal compounds, M_aX_b, undergo conversion reactions during lithiation, with formation of metal nanoparticles and Li_nX ($M_aX_b + (b\cdot n)Li^+ + (b\cdot n)e^- \leftrightarrow aM + bLi_nX$). When their reaction mechanism is known, the theoretical capacity of electrode materials can be calculated. For example, the theoretical capacity of TiO_2 is 335 mAh g^{-1} for 1 mol equivalents of Li insertion ($TiO_2 + Li^+ + e^- \leftrightarrow LiTiO_2$), while that of MnO_2 is 1233 mAh g^{-1} based on conversion reaction ($MnO_2 + 4Li^+ + 4e^- \leftrightarrow Mn + 2Li_2O$).

However, numerous reports have shown that the reversible capacity of various electrode materials can exceed their theoretical value based on the above reactions. The excess amount over the theoretical value is generally described as extra capacity, or capacity from abnormal charge storage. The observed reversible capacity and theoretical value of anode materials that are reported to exhibit this unusual phenomenon in recent work are summarized in **Table 1**, together with proposed origins for the additional capacity. With the contribution of extra capacity, values above 1000 mAh g^{-1} can be reversibly delivered in many different materials, even as high as 1500 mAh g^{-1} in some cases. In addition, some electrode materials exhibit more than twice their theoretical value. These results clearly demonstrate that there are additional charge storage reactions beyond the three general mechanisms above.

In 2002, Laruelle et al. observed high extra capacity in transition metal oxides undergoing conversion reactions. They ascribed the extra capacity to be originated from the formation and decomposition of surface polymeric/gel-like film (PGF) from electrolyte decomposition.[36] Since then, this mechanism has been widely considered as a reason for extra capacity. Nonetheless, numerous efforts have been made to further pinpoint the specific reasons for the abnormally high capacity. As described in **Figure 1**, the extra capacity is generally delivered at very low potentials, after the conventional reaction in the bulk is

finished. At these stages, the system is notably more complicated than at the start due to changes in the electrode and electrolyte, induced by extensive lithiation. As analytical science and technology advances, real-time observation of dynamic changes of the electrode material in LIBs and element-specific observation on target species in the material have become possible.[37–39] The sophisticated investigation of a complex system that consists of surface layer derived from electrolyte decomposition, nanoparticles induced by electrochemical reactions and the electrolyte unveiled various new paradigms of charge storage. To date, formation/decomposition of electrolyte-derived surface layer, interfacial charge storage, and redox reaction of compounds like LiOH are most widely cited to explain the extra capacity. Furthermore, other reactions such as contribution of defects, surface reactions, and redox reactions of other Li-containing species have been proposed. A detailed description of the proposed working mechanisms leading to abnormal charge storage reactions is provided in sections 3.1–3.4. Given the value of achieving ever increasing capacity at low potential, a complete understanding of additional charge storage reactions is required for developing electrode materials where these capabilities are employed in the most efficient and sustainable manner, thus going beyond the current limitations of LIB technology in addition to exploring novel electrochemical reactivity. **Table 1** also exemplifies cases where capacity increase has been observed after extended cycling. The changes generating the new environments within electrode affecting negative fading will be discussed in section 3.5.

Table 1. Theoretical value and actual charge storage capacity at the first charge and at the prolonged cycle in various anode materials exhibiting extra capacity, with suggested origins of additional capacity

Sample	Theoretical capacity (mAh g^{-1})	Reversible capacity (1st charge) (mAh g^{-1})	Origin of additional capacity	Long-term cycle behavior (cycle, current (A g^{-1}))	Ref.
Hollow mesoporous $Co(PO_3)_2$@Carbon Polyhedra	600	696	- Electrolyte-derived surface layer - Reduction of Li_2CO_3 in SEI layer	517 (50^{th}, 0.2), 601 (500^{th}, 1)	40
Recticulate dual-nanowire aerogel (carbon nanotube (CNT) /FeS_2)	894	1000	- Electrolyte-derived surface layer - Double-layer capacitance	1031 (100^{th}, 0.1)	41
Rice-panicle-like γ-Fe_2O_3@C nanofibers	1005	1414	- Electrolyte-derived surface layer	1827 (50^{th}, 2)	42
$Fe_{2.76}Sn_{0.24}O_4$/rGO	905 or 1019	1150	- Electrolyte-derived surface layer	1428 (100^{th}, 0.2)	43
Co_3O_4/C nanofibers	890	922	- Electrolyte-derived surface layer	1491.5 (180^{th}, 0.2)	44
Porous $MnCO_3$	466	1190	- Electrolyte-derived surface layer - surface absorption	783 (200^{th}, 0.5)	45
Graphene-wrapped porous $MnCO_3$	466	1735		1168 (200^{th}, 0.5)	
α-Fe_2O_3 nanocrystals	1007	1054	- Electrolyte-derived surface layer	1160 (300^{th}, 1)	46
Li_2MnO_3-CNTs composite	917	1006	- Electrolyte-derived surface layer - Interfacial charge storage	930.3 (50^{th}, 0.1)	47
Porous yolk-shell $ZnCo_2O_4$ spheres	900	1171	- Electrolyte-derived surface layer	1214.5 (100^{th}, 0.2)	48
$NiCo_2O_4$ nanoparticles	890	1144	- Electrolyte-derived surface layer - Interfacial charge storage	661 (500^{th}, 0.5)	49
Hollow porous λ-MnO_2	1233	1400	- Electrolyte-derived surface layer - Interfacial charge storage	1050 (50^{th}, 0.2)	50
SiO_x/Fe_3O_4 (Fe_xSi_y) heterojunction nanoparticles	>926	940	- Electrolyte-derived surface layer	1357.2 (550^{th}, 1)	51
Porous Fe_3O_4/carbon microspheres	926	999	- Electrolyte-derived surface layer - Interfacial charge storage - Redox reaction of LiOH	1317 (130^{th}, 0.1)	52
Porous MoO_2-Cu/C/Graphene nano-octahedrons quadruple nanocomposites	838	938	- Electrolyte-derived surface layer - Interfacial charge storage	1114.8 (100^{th}, 0.1)	53
Nanostructured α-Fe_2O_3	1007	851	- Electrolyte-derived surface layer - Interfacial charge storage	1239.2 (500^{th}, 1)	54
MnO-doped Fe_3O_4@C	924	939	- Electrolyte-derived surface layer - Interfacial charge storage	1297.5 (200^{th}, 0.2)	55
MoO_3 nanosheets on graphene	1117	1548	- Electrolyte-derived surface layer - Redox reaction of Li_2CO_3 - Redox reaction of LiOH	1533 (50^{th}, 0.050) 750 (1000^{th}, 1)	56
Mesoporous RuO_2	807	1130	- Interfacial charge storage		57
Fe_3O_4@polyaniline yolk-shell micro/nanospheres	926	1182	- Electrolyte-derived surface layer	982 (50^{th}, 0.1)	58
MnO/C Hybrids	756	1165	- Electrolyte-derived surface layer	1120 (50^{th}, 0.3)	59

Sample	Theoretical capacity (mAh g^{-1})	Reversible capacity (1st charge) (mAh g^{-1})	Origin of additional capacity	Long-term cycle behavior (cycle, current (A g^{-1}))	Ref.
			- Oxidation to high valence Mn		
Ultrathin layered $Co(Ac)_{0.48}(OH)_{1.52}\cdot 0.55H_2O$ anchored to graphene nanosheets	462	1216	- Redox reaction of LiOH, LiAc	1050 (200^{th}, 1), 780 (300^{th}, 1)	60
Fe_3S_4 nanoparticles wrapped in an reduced graphene oxide (rGO) matrix	725	916	- Electrolyte-derived surface layer	950 (100^{th}, 0.1), 720 (800^{th}, 1)	61
Nanocrystalline $NiFe_2O_4$,	916	1190	- Electrolyte-derived surface layer	786 (100^{th}, 0.5)	62
Fe_3O_4 on defective rGO	922	1045	- Defects on rGO	240 (1000^{th}, 2.5)	63
RGO–MnO–RGO sandwich nanostructures	756	658	- Oxidation to high valence Mn	1116 (200^{th}, 1), 947 (500^{th}, 5)	64
Hierarchical MnO nanorods/carbon	756	884	- Electrolyte-derived surface layer	667 (500^{th}, 0.5), 300 (3000^{th}, 4)	65
Graphene-mimicking 2D porous Co_3O_4 nanofoils	890	1007	- Electrolyte-derived surface layer	1279.2 (50^{th}, 0.089)	66
Hollow-porous α-Fe_2O_3	1005	1125	- Electrolyte-derived surface layer - Reversible redox reaction of Li_2CO_3	1150 (1000^{th}, 1)	67
γ-Fe_2O_3 nanoparticles	1008	1100	- Electrolyte-derived surface layer	1370 (50^{th}, 0.05)	68
CoO–graphene hydrogel	715	980	- Electrolyte-derived surface layer	1010 (100^{th}, 0.1)	69
SnO_2 nanospheres on rGO	1494	900	- Electrolyte-derived surface layer - Interfacial charge storage	1335 (500^{th}, 0.5)	70
Co@Co_3O_4/CNTs nanocomposite	890	747	- Interfacial charge storage	820 (250^{th}, 0.2) 760 (350^{th}, 1) 529 (600^{th}, 2)	71
NiCo-$NiCo_2O_4$@CNTs	890	800	- Interfacial charge storage	1405 (500^{th}, 0.2) 1324 (1000^{th}, 0.5)	72
Fe_2O_3-carbon fiber composites	607	938	- Interfacial charge storage	634 (150^{th}, 0.05)	73
Graphene nanosheets@$NiCo_2O_4$	890	928	- Interfacial charge storage	1024 (200^{th}, 0.5), 648 (200^{th}, 3)	74
Co_3O_4 nanofibers@rGO	871	1105	- Electrolyte-derived surface layer - Interfacial charge storage	1371 (200^{th}, 1), 615 (600^{th}, 4)	75
$ZnMn_2O_4$ with different porous architectures	784	870	- Electrolyte-derived surface layer - Interfacial charge storage - Oxidation to high valence Mn	1600 (100^{th}, 0.1)	76
Mn_3O_4/nitrogen-doped porous carbon fiber hybrids	937	1058	- Electrolyte-derived surface layer - Interfacial charge storage	840(500^{th}, 0.3)	77
α-Fe_2O_3 nanorods	1007	1019	- Electrolyte-derived surface layer - Interfacial charge storage	728(2000^{th}, 0.332)	78
Fe_2O_3 nanoparticles confined in CNTs Fe_2O_3 nanoparticles coated on CNTs	1007	1143 1092	- Electrolyte-derived surface layer - Interfacial charge storage - Redox reaction of LiOH		79

Sample	Theoretical capacity (mAh g^{-1})	Reversible capacity (1st charge) (mAh g^{-1})	Origin of additional capacity	Long-term cycle behavior (cycle, current (A g^{-1}))	Ref.
Co/CoO@N-C	718	881	- Electrolyte-derived surface layer - Interfacial charge storage - Li storage in carbon	1115 (125^{th}, 0.2)	80
hierarchical pinecone-like $CoCO_3$ sub-microspheroids	466	1078	- Electrolyte-derived surface layer - Redox reaction of Li_2CO_3	1475 (500^{th}, 0.5)	81
Micro/nano porous spheres $ZnCo_2O_4$	900	1120	- Electrolyte-derived surface layer - Interfacial charge storage - Li storage in carbon	950 (90^{th}, 0.976)	82
$MnCO_3$/multi-walled CNT nanocomposite	466	770	- Reversible redox reaction of Li_2CO_3 - Double layer capacitance from carbon	704 (110^{th}, 0.1)	83
Porous MnCO3 hierarchical micro/nano cubes	466	762.2	- Redox reaction of Li_2CO_3	834 (100^{th}, 0.466)	84
$CoCO_3$/graphene	466	1273	- Redox reaction of Li_2CO_3	602 (100^{th}, 0.2)	85
$Ni_xMn_{1-x}CO_3$ submicrospheres at different x values	466	825	- Redox reaction of Li_2CO_3	709 (500^{th}, 1), 549 (1000^{th}, 2)	86
rGO-coated $Co_2(OH)_2CO_3$ nanosheet array	716	2109	- Interfacial charge storage - Formation of alloy - Redox reaction of Li_2CO_3	1600 (100^{th}, 1)	87
Acanthosphere $FeCO_3$	462.7	997	- Redox reaction of Li_2CO_3	587 (100^{th}, 0.1)	88
Core-shell structured $MnCO_3$@C	466	1616	- Redox reaction of Li_2CO_3	1115 (230^{th}, 0.1)	89
$Co_2(OH)_2CO_3$–GO nanocomposites	1644	1262	- Redox reaction of Li_2CO_3 - Redox reaction of LiOH	1046 (300^{th}, 0.2)	90
Fe_2O_3@C/Co_3O_4	1000	1236.3	- Electrolyte-derived surface layer - Redox reaction of LiOH	1035 (350^{th}, 0.2)	91
Colloidal silica-assisted $Co(OH)_2$	577	1112	- Contribution of LiOH	1019 (30^{th}, 0.0577)	92
Fe_2O_3/rGO nanocomposite	1007	1212	- Redox reaction of LiOH	1064 (100^{th}, 0.2)	93
Hollow-structured oxygen-vacancy-rich Fe_2O_3/MnO_2 nanorods	1007–1232	1187	- Electrolyte-derived surface layer - Interfacial charge storage - Redox reaction of LiOH	706 (2000^{th}, 5)	94
Ordered mesoporous MoO_2	838	1308	- Formation of metallic Li-rich phase	1594 (50^{th}, 0.08)	95
1T-MoS_2/graphene	670	1200	- Li absorption in Mo precipitates	1800 (800^{th} , 1)	96

3. PHENOMENA PROPOSED TO GIVE RISE TO ABNORMAL REVERSIBLE CAPACITY

3.1. Formation and Decomposition of Electrolyte-Derived Surface Layers

In the most widely commercialized LIBs using graphite anode materials and organic electrolyte, reduction of the electrolyte occurs at the anode surface at low potential.[97–100] The resulting products form a passive layer at the interface. This layer was termed solid electrolyte interphase (SEI) by E. Peled due to its similar characteristics with a solid electrolyte,[101] as it allows transport of Li ions during electrochemical cycling while blocking both electrons, which prevents further electrolyte degradation, and solvent co-intercalation. Being a protective layer, the quality of the SEI layer significantly affects battery cycle life, rate capability and even safety.[102–107] There have been extensive studies targeting the formation mechanism and identification of the SEI layer, with modern analytical science enabling the observation of even nanoscale changes. Consequently, while highly dependent on cell operating conditions, the SEI layer is generally accepted to consist of various inorganic/organic compounds such as Li_2O, Li_2CO_3, LiF and/or $ROCO_2Li$, among oligomeric/polymeric compounds from the electrochemical decomposition of Li salts or the organic solvent in the electrolyte.[102,104,108–116] The SEI layer is mostly formed during the first lithiation, and slowly grows until fully developed. Once it is formed, further growth and decomposition of the SEI layer is restricted. Despite the beneficial role of SEI as mentioned above, its formation entails a noticeable capacity loss due to the irreversibility of the formation.[103,104,117]

Contrary to the conventional common knowledge that the developed cathodic reaction layers on electrode surfaces can rarely be decomposed, Poizot et. al first reported that such layers could be consumed upon charge after being formed during lithiation through

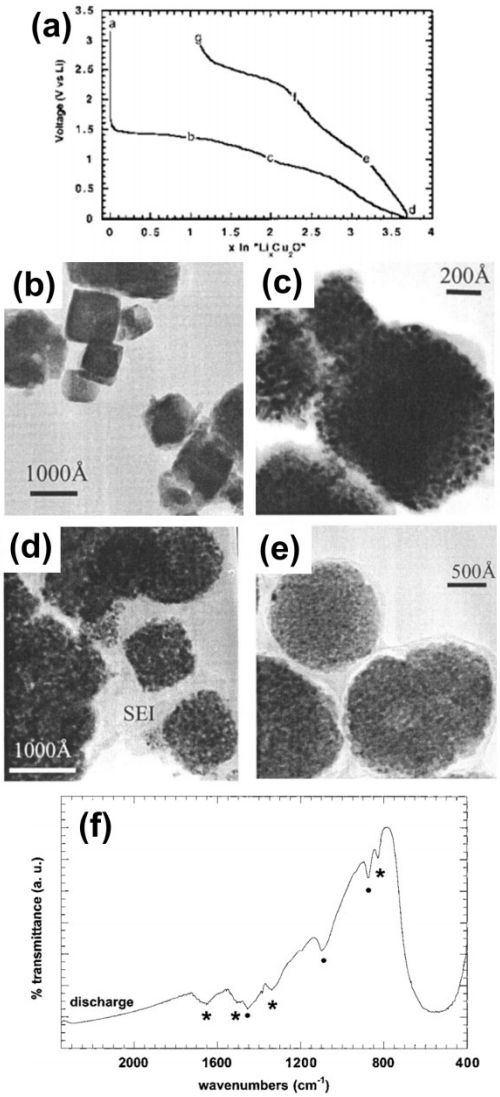

Figure 2. (a) Voltage profile of Cu_2O electrode. TEM images of the electrodes (b) at OCV, (c) after 2 mol equivalents of Li reaction, (d) at full discharge and (e) at full charge. (f) IR spectra of full discharged Cu_2O electrode. (Reproduced with permission from Ref. xx, copyright (xxxx) xxxxx)

conversion of metal oxide anodes.[118] This phenomenon is exemplified for Cu_2O in **Figure 2**.[119] The electrochemical response in **Figure 2(a)** indicated that two sloping voltage ranges appear at 1.4–1.0 V and 1.0–0.02 V during the first discharge delivering capacities corresponding to 2 and 1.7 mol equivalents of Li, respectively. In total, ~3.7 mol equivalents of Li reacted during the first discharge and ~2.6 mol during the first charge, compared to the theoretical amount of 2 mol based on conversion to Cu metal. To observe the structural changes during the electrochemical reaction, transmission electron microscope (TEM) images

at different states of charge were collected (**Figure 2(b)–(e)**). After reaction with 2 mol equivalents of Li, the particles were significantly pulverized from ~100 nm to ~5 nm while the overall shape of square platelet morphology remained with the formation of very thin layer at the surface. At full discharge, the nanograins were completely surrounded by large veil-like coatings as described in **Figure 2(c)**. Infrared (IR) spectra of this electrode, in **Figure 2(f)**, reveal that the layer was composed of Li_2CO_3 and $ROCO_2Li$, similar to the SEI layer on carbonaceous anodes. Surprisingly, the very thick organic layer almost completely disappeared after the subsequent delithiation, and only a thin (~80 Å) coating remained, indicating that the surface layer can be decomposed. It was proposed that the metallic Cu nanograins generated from the conversion of Cu_2O facilitate both the reaction with electrolyte to form thick surface layers at low potential, and their dissolution upon charge.

Thereafter, identical phenomena were reported in the CoO/Li cell.[36] As described in **Figure 3(a)**, the voltage remained constant in a process accumulating ~2 mol equivalents of Li during the first discharge, where the conversion reaction of CoO occurred. Afterwards, additional ~1.5 mol equivalents of Li were accumulated between 1.7 and 0.02 V. The electrochemical process at this range presented a capacitive nature as opposed to the clearly

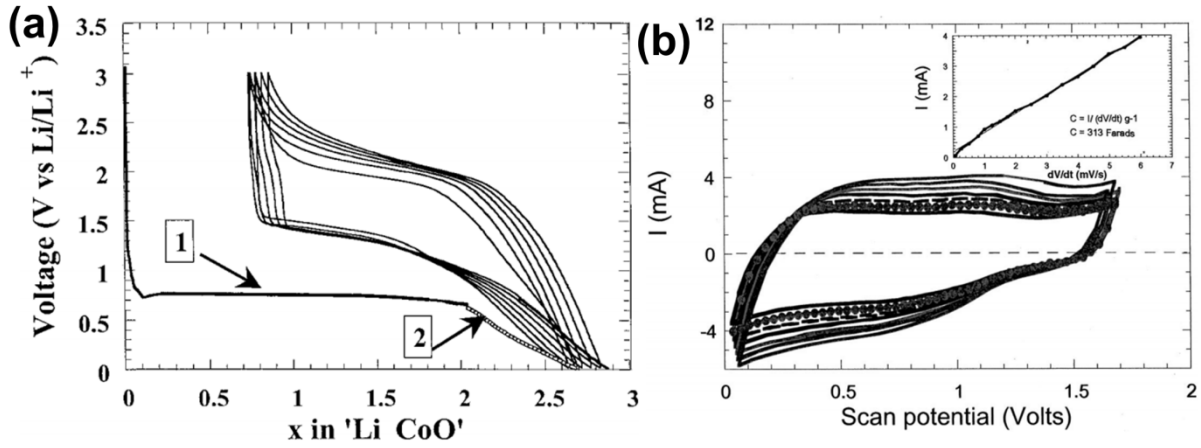

Figure 3. (a) Voltage profile and (b) CV curve of CoO electrode (Reproduced with permission from Ref. xx, copyright (xxxx) xxxxx)

faradaic process of the conversion reaction, which could be inferred from the rectangular shape of cyclic voltammetry and linear variation of I as a function of dV/dt in **Figure 3(b)**. However, the charging of the electrical double layer on metallic cobalt cannot deliver such large capacity, even considering the high surface area of nanometric particles. They proposed that the extra capacity at the low potential region is originated from growth and dissolution of thick surface layer covering thin SEI layer. They first designated the layer as PGF. However, the distinction between SEI layer and PGF remained vague despite significant analytical efforts, because the components are similar in both cases, and which ones actually decompose during charge is the object of controversy. Nowadays, a few different terms are used to describe the large surface layer beyond "PGF film",[36,120] including polymeric-like SEI,[121,122] polymeric surface layer,[123–125] dissolution of the SEI layer, or gel-type layer. Thus, we will not distinguish the PGF and SEI layer, and just refer to it as "electrolyte-derived surface layer" hereafter.

The decomposition of the electrolyte-derived surface layer is thought to originate from a catalytic process by the extremely small metallic nanoparticles formed after conversion. To confirm the role of nanosized transition metal, Su et. al prepared Fe@C composite materials and compared electrochemical behaviors with pure carbon as shown in **Figure 4**.[126] Despite negligible oxygen contents (1.8 wt%) and the fact that Fe does not form alloys with Li, Fe@C composite electrodes exhibited high capacities of 1379 and 601 mAh g^{-1} during first discharge and charge, respectively, while a pure carbon electrode delivered only 667 and 310 mAh g^{-1} (**Figure 4(a)**). As shown in **Figure 4(b)**, there were no obvious changes in the X-ray diffraction (XRD) patterns after electrochemical cycling except for the appearance of a broad peak at 20–25º from lithiated carbon and SEI components. Thus, oxidation to FeO_x and subsequent reduction can be neglected. However, as shown in **Figure 4(c) and (d)**, the cyclic voltammetry (CV) of the Fe@C composite electrode showed additional broad peaks at 0.3–

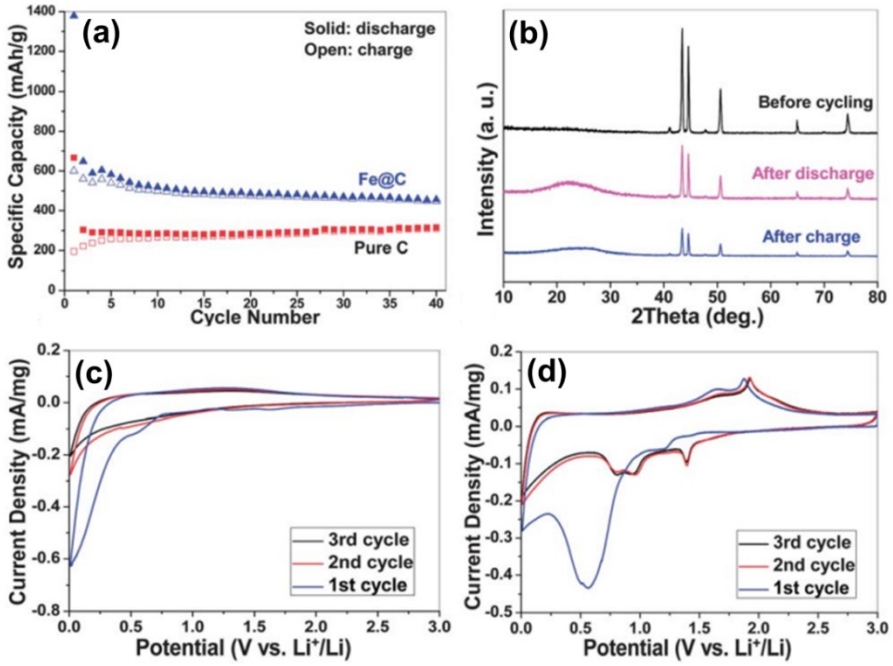

Figure 4. (a) Cycling performance of Fe@C composite and pure carbon electrode, (b) XRD patterns of Fe@C electrodes before cycling and after the initial discharge/charge. CV curves of (c) pure carbon electrode and (d) Fe@C composite electrode for the initial 3 cycles. (Reproduced with permission from Ref. xx, copyright (xxxx) xxxxx)

0.8 V during the first anodic scan which were not observed in pure carbon. These peaks were associated with the appearance of new broad XRD peaks from the formation of the surface layers to a much greater extent compared to the carbon electrode. During the subsequent charge, two oxidation peaks were visible at ~1.6 and 1.9 V. They hypothesized that these peaks originated from the decomposition of the surface layer components, and that metal nanoparticles could catalyze the formation/decomposition of surface layers from interactions between electrolyte and electrode.

Currently, the formation and decomposition of the surface layer is most widely considered as the origin of additional capacity in conversion reaction-based anode materials and has been observed in various materials through diverse methods of analysis method. As exemplified above, TEM is one of the most effective techniques to visualize its formation and decomposition (**Figure 5(a)–(d)**).[32,36,118,119,127–130] Atomic force microscopy (AFM) is also useful to investigate the reversibility of the formation of surface layers, by observing the

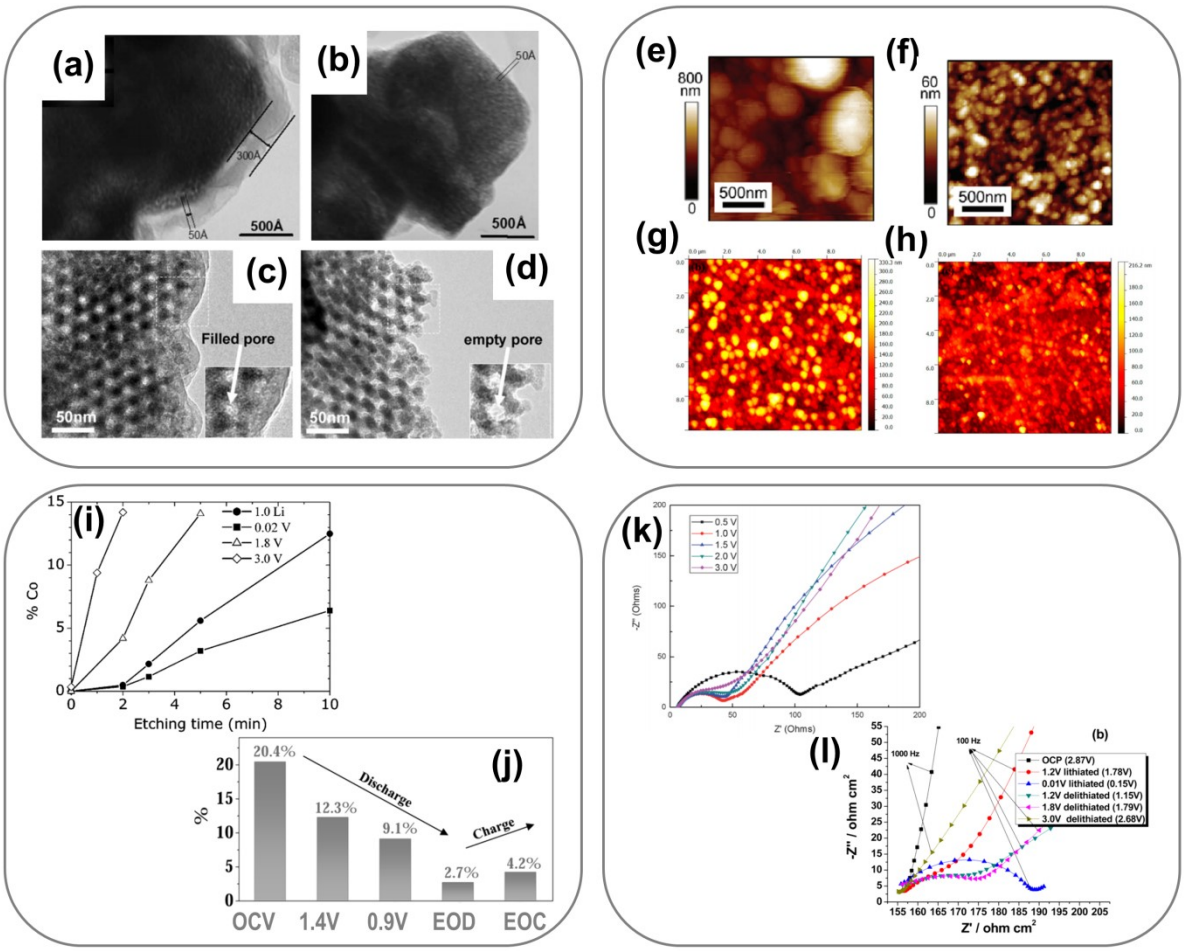

Figure 5. HRTEM images of (a),(b) Cu_3N and (c),(d) mesoporous C_2O_3, and AFM images of (e),(f) MnO and (g),(h) Fe_2O_3 electrodes at the fully discharged and fully charged states, respectively. Changes of (i) Co atomic percentages in CoO during cycling as a function of etching time and (j) intensity ratio of a peak corresponding to carbon black in C 1s XPS spectra in Fe_2O_3 at different state of charge. (k),(i) Variation in EIS spectra of Fe_2O_3 electrode at selected potentials. (Reproduced with permission from Ref. xx, copyright (xxxx) xxxxx)

changes of surface topology.[131–134] In **Figure 5(e)**, the surface grain size, shown in the bright area, was measured to be ~200 nm for a fully discharged MnO electrode formed with ~20 nm particles. The enormous increase of surface grain size could not be accounted for by the volume expansion inherent to the bulk conversion (theoretically, 169%), leading to the hypothesis that it could result from the growth of surface layers. Subsequently, after delithiation, the grain size and surface roughness significantly decreased as shown in **Figure 5(f)**, indicating decomposition of such surface layers.[131] Similar swelling and shrinkage of the grain was observed in a Fe_2O_3 anode as in **Figure 5(g) and (h)**. Surface sensitive analyses

techniques such as X-ray absorption spectroscopy (XPS) and soft X-ray absorption spectroscopy (soft XAS) are also useful tools for observing formation and decomposition of the surface layer.[122,135–139] The atomic percent of Co from XPS spectra during electrochemical cycling of CoO anode as a function of etching time with argon ion sputtering is shown in **Figure 5(i)**. More etching time was needed to detect cobalt at the surface as discharge progressed, indicating the surface layer thickened. At full lithiation, ~10 min of etching time was needed to observe 5 % of cobalt, which corresponds to a ~100 Å surface layer. In contrast, the etching time significantly decreased upon subsequent delithiation, supporting the dissolution of surface layers.[135] The variation in the relative intensity of the carbon black component, used as a conductive additive, measured from the C 1s spectra of Fe_2O_3 electrode during cycling is provided in **Figure 5(j)**. It provides another proxy for the growth of interphases. As the surface layer thickened during discharge, the relative intensity of carbon black components decreased. Again, this trend was reversed upon full charge.[122] The formation and decomposition of the surface layer can be also confirmed by monitoring electrochemical impedance spectroscopy (EIS) since the diameter of the measured semicircle is commonly ascribed to the resistance from the electrode-electrolyte interface.[137,140,141] The diameter increases during lithiation and decreases during delithiation, as seen in **Figure 5(k) and (l)**. Other analysis techniques such as thermogravimetry and mass spectrometry (TG-MS),[142] time-of-flight secondary ion mass spectrometry (SIMS),[133,134,137] Fourier transform infrared spectroscopy (FTIR),[143] and infrared reflection absorption spectroscopy (IRRAS)[136] have also been used to demonstrate the formation and decomposition of electrolyte-derived surface layer.

Some of these techniques were also used to unveil which components are formed in the surface layers during lithiation and decomposed during delithiation. Dedryvère et al. conducted XPS analysis of the surface of CoO anode during electrochemical cycling in 1M

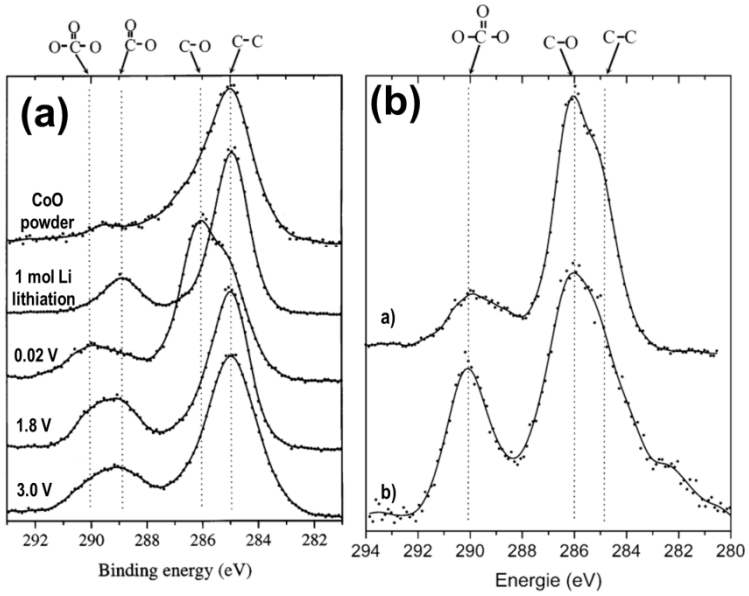

Figure 6. C 1s XPS spectra of CoO electrode recorded (a) at different state of charge and (b) at full discharged samples in a) powder state and b) sintered pellet. (Reproduced with permission from Ref. xx, copyright (xxxx) xxxxx)

$LiPF_6$ in EC/DMC 1:1.[135] The C 1s XPS spectra measured without etching are presented in **Figure 6(a)**. All spectra show a large peak at 285.0 eV which can be assigned to hydrocarbon from contamination. After reaction with 1 mol equivalents of Li, a peak assigned to COO- components at 289.0 eV. Then, at full discharge, the main components were assigned to the presence of CO- species inferred from the intense peak observed at 286.0 eV. Also, peaks from Li_2CO_3 and $ROCO_2Li$ components can be observed at 290.0 and 289.0 eV. **Figure 6(b)** compares the C 1s XPS spectra of a fully discharged sample in both powder form and as sintered pellet scraped under ultrahigh vacuum. After mechanically scraping the sintered pellet, the intensity of the peak at 290.0 eV increased, indicating that the surface layer at greater depths is rich in Li_2CO_3 and $ROCO_2Li$ and the outer surface layer is mainly composed of organic species, probably polymers or oligomers with $(CH_2CH_2O)_n$ units, or related. After charge to 1.8 and 3.0 V, the intense peak from the organic component at 286 eV disappeared while the peaks assigned to inorganic components of Li_2CO_3 and $ROCO_2Li$ at 290.0 and 289.0 eV remained, showing that the inorganic compounds closer to the electrode

surface remain stable and only the organic components at outer depths are decomposed during charge.

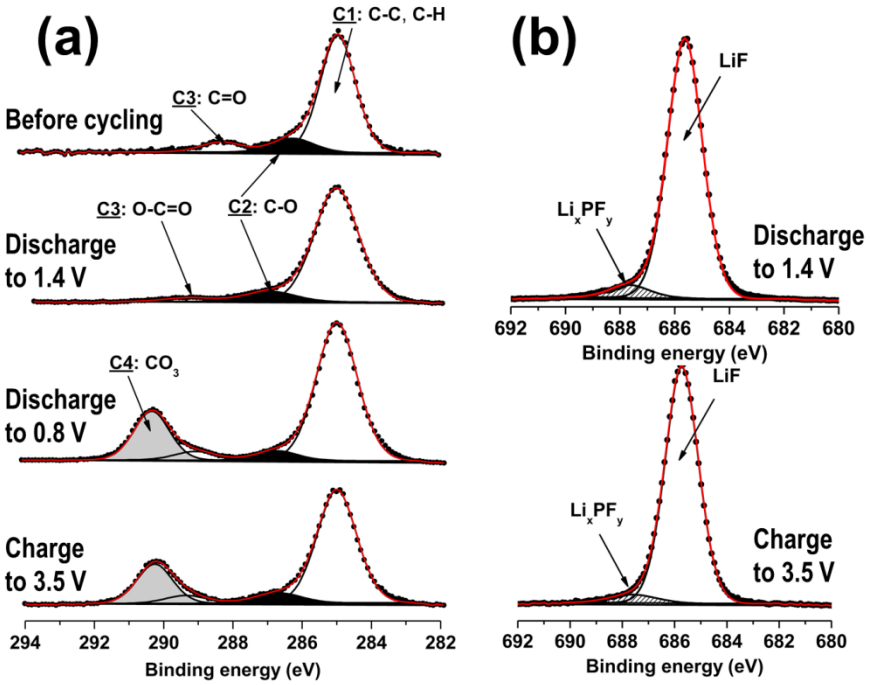

Figure 7. (a) C 1s and (b) F 1 XPS spectra of CuO thin film electrodes at different states of charge during the first cycle. (Reproduced with permission from Ref. xx, copyright (xxxx) xxxxx)

In contrast, Martin et al. observed decomposition of inorganic Li_2CO_3 species in CuO thin film electrode with 1 M $LiPF_6$ dissolved in 1:1:3 EC/PC/DMC solvent.[132] The C 1s and F 1s XPS spectra of the CuO electrode collected during the first cycle are provided in **Figure 7(a) and (b)**, respectively**.** In the pristine state, the largest C 1s peak at 285.0 eV corresponds to hydrocarbons due to contamination in the measurement chambers, which were also detected in the XPS spectra of the other samples. After the reaction with 0.7 mol equivalents of Li per CuO (discharge to 1.4 V), the C 1s XPS spectra did not change much, while the F 1s XPS spectra show a large peak at 685.6 eV that can be assigned to LiF. This result shows that LiF is formed at the beginning of the discharge, from the decomposition of $LiPF_6$ salts in the electrolyte. After reaching 0.8 V, the LiF peak totally disappeared, and a new peak at 290.3 eV, from -CO_3 compounds, appeared in C 1s XPS spectra. As the intensity of the peak from

C-O bond at 286.7 eV remained low, the new peaks at 290.3 eV could not be attributed to $ROCO_2Li$, where the number of carbon atoms in C-O and in $–CO_3$ is same. Thus, they proposed that the new peaks were generated from the growth of Li_2CO_3 at surface. The appearance of Li_2CO_3 and disappearance of LiF at the surface in this stage show that LiF first grows at the surface of electrode at the initial stages of discharge and, then, Li_2CO_3 covers the LiF layers during further discharge. During subsequent charge to 2.6 V, the C 1s and F 1s spectra remained unchanged demonstrating that the composition of outer surface layer was not modified. However, after charging to 3.5 V, LiF could be observed again. In addition, they observed that the atomic concentration of carbon in $-CO_3$ environment decreased from 8.3 % to 2.1 %, demonstrating the partial dissolution of Li_2CO_3 in the outer surface layer.

By using the different probing depth of total electron yield (TEY) and total fluorescence yield (TFY) modes of soft XAS, the depth-dependent composition changes of the surface

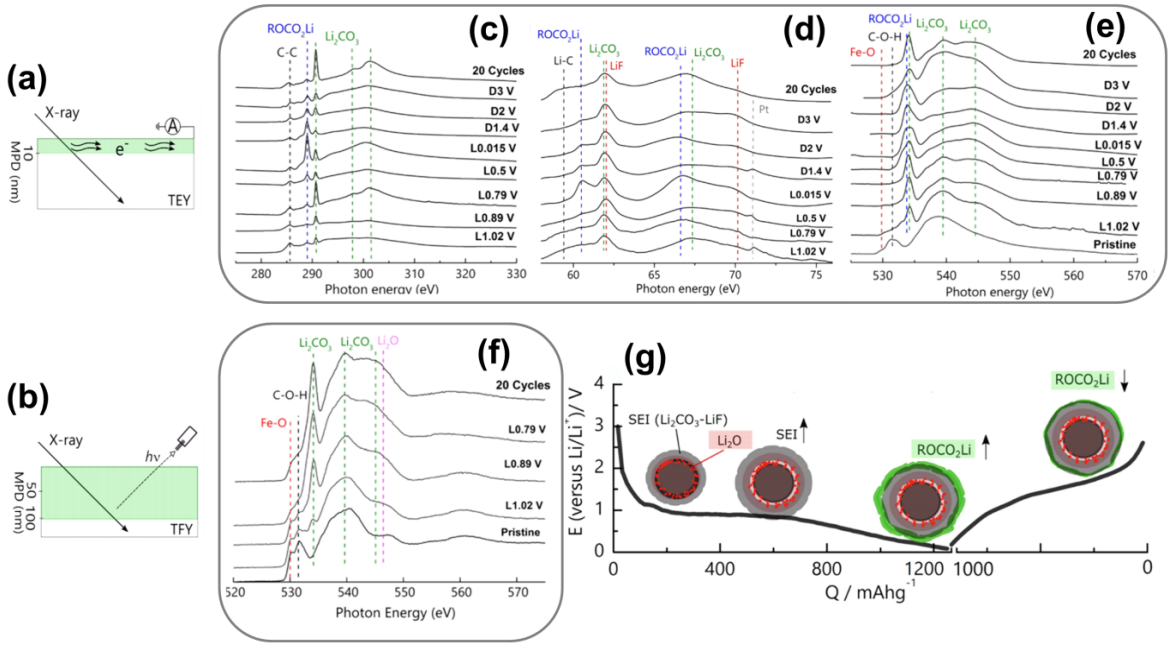

Figure 8. Illustration of different penetration depth in (a) TEY and (b) TFY soft XAS experiments. Variation of (c) C K-edge, (d) Li K-edge and (e) O K-edge TEY spectra, and (f) O K-edge TFY spectra of $ZnFe_2O_4$-C composite electrodes at specified points. (g) Sketch of the surface layer evolution process during a cycle on a C-coated $ZnFe_2O_4$ electrode. (Reproduced with permission from Ref. xx, copyright (xxxx) xxxxx)

layer on carbon-coated $ZnFe_2O_4$ anodes was inspected.[138] The TEY and TFY detectors measure emitted electrons from the excited state and emitted photons, respectively. Due to the different mean free path of electrons and photons, the effective probing depths of TEY and TFY are 2–10 nm and 50–100 nm as illustrated in the schematic in **Figure 8(a) and (b)**. Here, the electrochemical experiment was conducted with electrolyte of $LiPF_6$ salt dissolved in EC/DMC 1:1 solvent. Gradual growth of a sharp peak at 291 eV was noted in the C K-edge TEY spectra after discharge to 0.79 V (denoted as L0.79 V in **Figure 8(c)**), that corresponds to Li_2CO_3. The intensity of the Li_2CO_3 peak decreased at lower potential, being replaced by a peak at 289 eV, assigned to $ROCO_2Li$. During the subsequent charge, the intensity of the $ROCO_2Li$ peak was reduced. The growth and decrease of the peak intensity of $ROCO_2Li$ was also observed in the Li K-edge TEY spectra, with other signals corresponding to Li_2CO_3 and LiF after the first discharge, as shown in **Figure 8(d)**. The increasing alkyl carbonate signal with respect to LiF/Li_2CO_3 at low potential and its disappearance during subsequent charge indicates that the alkyl carbonate is formed on top of the LiF/Li_2CO_3 layer at low potential during discharge and dissolved during charge. In the O K-edge TEY spectra in **Figure 8(e)**, the initial peaks assigned to C-O-H bonds in the binder, at 531.5 eV, and Fe-O bond from $ZnFe_2O_4$, at 529.6 eV, disappeared at the initial stages of lithiation, giving way to peaks at 533.7, 539.4 and 544.5 eV ascribed to Li_2CO_3, supporting that the surface of $ZnFe_2O_4$ is firstly covered by Li_2CO_3. Insight from deeper discharge were collected from the O K-edge TFY spectra in **Figure 8(f)**. Peaks from Fe-O and C-O-H bonds were clearly shown even after lithiation. Lithiation resulted in growth of Li_2CO_3 without showing peaks from $ROCO_2Li$. The absence of peaks corresponding to $ROCO_2Li$ in the O K-edge TFY spectra, which can be clearly observed in the TEY spectra, indicates that the phase exists at the outermost surface. The combined TEY and TFY soft XAS results clearly show that the formation of the surface layer occurs in two steps as summarized in **Figure 8(g)**. Firstly,

Li_2CO_3 and LiF preferentially formed at the surface of the electrode. Then, Li_2CO_3 is partially replaced by $ROCO_2Li$ at the outermost surface. During subsequent charge, $ROCO_2Li$ at the outer layer is mainly decomposed, leading to reversible capacity.

Table 2 summarizes the composition of the surface layer upon discharge and the decomposable components in various anode materials with different electrolytes. It is generally accepted that electrolyte reduction products such as Li_2CO_3, $ROCO_2Li$, and other organic species are found at the surface layer, which can be also observed in the SEI layer of carbonaceous materials. However, there are discrepancies among different reports in the literature over which components contribute to the reversible extra capacity during cycling, as listed in **Table 2**. For example, some suggest that only organic carbonaceous components can be decomposed during delithiation,[135,142] while others claim that inorganic components (Li_2CO_3 and/or $ROCO_2Li$) are also active.[126,132,138] Therefore, further detailed investigations of electrolyte-derived surface layers depending on specific conditions are needed.

Table 2. Components of electrolyte-derived surface layer and the decomposable components among them in various types of anode materials.

Materials	Electrolyte	Components	Decomposable components	Ref.
CoO	1M $LiPF_6$ in EC/DMC 1:1	Inner : Li_2CO_3, $ROCO_2Li$, RCO_2Li, Outer : $(CH_2CH_2O)_n$	$(CH_2CH_2O)_n$	135
Cr_2O_3	1M $LiClO_4$ in PC	Li_2CO_3, small $ROCO_2Li$		136
Cr_2O_3	1M $LiPF_6$ in EC/DMC 1:1	organic/polymer species, $ROCO_2Li$	organic, polymer species	142
CuO	1M $LiPF_6$ in EC/PC/DMC 1:1:3 with (2% VC)	Inner : LiF, outer : Li_2CO_3	Li_2CO_3	132
CuO	1M $LiPF_6$ in EC/DMC 1:1	LiF, Li_2CO_3		144
CuO	1M $LiPF_6$ in EC/DMC 1:1	Inner : carbonates, outer : hydrocarbons		145
Fe_2O_3	1M $LiClO_4$ in PC	Li_2CO_3, small $ROCO_2Li$		137
Fe_2O_3	1M $LiClO_4$ in PC	Li_2CO_3, $ROCO_2Li$, RCH_2OLi		134
Fe_2O_3	1M $LiClO_4$ in EC/DEC 2:1	Inner : Li_2CO_3, minor $ROCO_2Li$ Outer : hydrocarbons		122
$Cr_xFe_{2-x}O_3$	1M $LiClO_4$ in PC	Li_2CO_3, $ROCO_2Li$/RCH_2OLi		133
Fe_3O_4	1M $LiPF_6$ in EC/DMC 3:7	large LiF, small Li_2CO_3/$ROCO_2Li$		146
	1M $LiPF_6$ in FEC/DMC 3:7	small LiF, large Li_2CO_3/$ROCO_2Li$		
$Mn_{0.33}Co_{0.67}C_2O_4$	1M $LiPF_6$ in EC/DMC 1:1	$ROCO_2Li$		143
$ZnFe_2O_4$-C	$LiPF_6$ in EC/DMC 1:1	Li_2CO_3, LIF, $ROCO_2Li$	$ROCO_2Li$	138

3.2. Interfacial Charge Storage

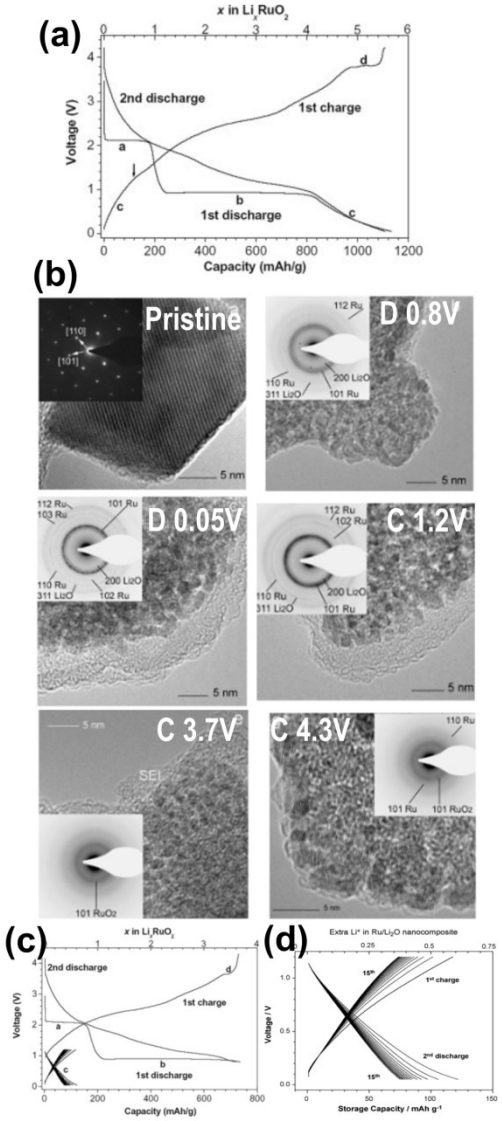

Figure 9. (a) Voltage profile of RuO_2 electrode with cutoff condition of 0.05–4.3 V. (b) HRTEM images of the RuO_2 electrode at specified potential. Voltage profile with cutoff condition of (c) 0.8–4.3 V and (d) 0.05–1.2 V. (Reproduced with permission from Ref. xx, copyright (xxxx) xxxxx)

In 2003, Balaya et al. investigated the electrochemical reaction mechanism of RuO_2, which stored 5.6 mol equivalents of Li over a wide voltage range of 0.05–4.3 V, as shown in **Figure 9(a)**.[147] During the first discharge, two plateau regions appeared at ~2.1 V (region a) and ~0.9 V (region b), followed by a long sloping region at low potential, region c. During subsequent charge, a relatively short plateau (region d) was observed at a high potential of ~3.8 V. Using XRD, it was confirmed that regions a and b arose from Li insertion to RuO_2 and its

subsequent conversion reaction, respectively. However, the electrochemical reactions in regions c and d could not be identified. Complementary high-resolution transmission electron microscopy (HRTEM) and selected area electron diffraction (SAED) measurements in **Figure 9(b)** confirmed that the conversion reaction of RuO_2 was completed after the reaction of ~4 mol of Li at 0.8 V (end of region b), forming metallic Ru and Li_2O. At this stage, only a thin surface film was observed. Then, after a full discharge to 0.05 V, a thick electrolyte-derived surface layer was observed without changing the Ru/Li_2O composite. The thick surface layer and metallic Ru/Li_2O composite still remained during charging up to 1.2 V, leading to the hypothesis that the capacity of ~120 mAh g^{-1} at this region was not solely delivered from the decomposition of the surface layer and oxidation of Ru. After reaching 3.7 V and 4.3 V, the metallic Ru was fully oxidized to RuO_2 and the thick surface layer almost disappeared. When the cycling window was constrained to 0.8–4.3 V, i.e., without the sloping region at low potential, it is noticeable that the plateau region d at 3.8 V was significantly reduced (**Figure 9(c)**), indicating that it might be ascribed to the decomposition of the surface layer. However, in **Figure 9(a)**, much smaller capacity was delivered in region d (where they hypothesized decomposition of surface layer occurred) compared to region c (where formation of surface layer might occur), again suggesting there might be an additional reaction at low potential, beyond the formation of electrolyte decomposed surface layer. As shown in **Figure 9(d)**, they found that electrochemical cycling between 0.05–1.2 V showed behavior reminiscent of capacitive systems. Based on the above results and the fact that neither Ru nor Li_2O can store Li, they proposed a new mechanism of interfacial charge storage which occurs at the interphase between nanosized metal and Li_2O grains through charge separation. In addition to oxides, similar behavior was claimed to occur in metal fluorides.[148,149]

The concept of interfacial charge storage mechanism is schematically described in **Figure**

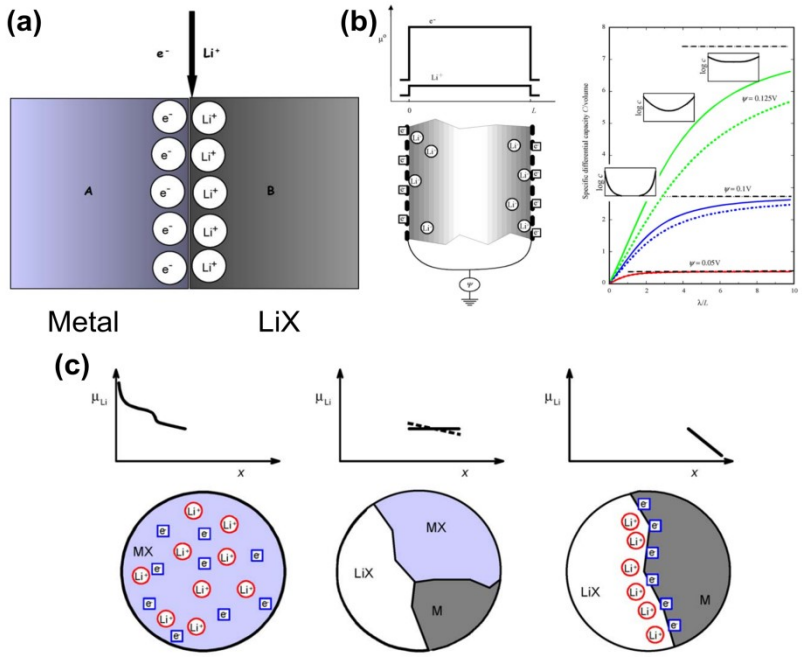

Figure 10. Schematic representation of (a) the interfacial charge storage mechanism. (b) Heterostructure metal/ionic conductor/metal and prediction of differential capacity per volume as a function of inverse spacing length. (Dashed line indicates the value in case of volume insertion) (c) Illustration of the three sequence of Li storage in electrode particle by turns of insertion, phase separation and interfacial charging. (Reproduced with permission from Ref. xx, copyright (xxxx) xxxxx)

10(a). According to this model, Li^+ can be accumulated at the Li_2O side of the boundary and the electrons are stored in the metal side only where the metal and Li_2O phase are in intimate contact. It occurs until μ_{Li} becomes equal to the chemical potential of metallic Li. Since the electronegativity difference between metal and Li becomes very small if the metal alloys with Li, this interfacial charge storage would preferentially occur in non-alloying metals. Also, as it resembles the characteristics of double-layer capacitance, it is highly affected by the particle size through the electrochemically active surface area. In **Figure 10(b)**, a sketch of the cell considered for calculations of space charge capacitance and the corresponding specific differential capacity per unit of volume as a function of inverse interfacial spacing is provided. The specific capacity increases linearly with 1/L when the particle size is relatively large. However, at smaller scales, the thickness dependence disappears, and the specific differential capacity reaches a saturation value, close to the value of insertion reaction. Thus,

they proposed that interfacial effects could play a dominant role in nanostructured solids. Overall, the reaction is proposed to follow the sequence in **Figure 10(c)**. Firstly, Li is homogeneously inserted into the bulk, followed by conversion to form phase separated metal and LiX. At low potential, further lithiation occurs at the interfaces, showing capacitive behavior.[150,151]

Zhukovskii et al. also conducted *ab initio* density functional theory (DFT) calculation on model Ti/Li_2O interfaces to explore the consequences of this interfacial storage mechanism.[152] As shown in **Figure 11**, they considered different positions for extra Li: on the Li_2O slab surface opposite to the Ti/Li_2O interface, at deep internal layers and at the interface between Ti and Li_2O slab. It should be noted that the other conditions such as electrolyte or surface layer were not considered to simplify this calculation. The calculated relative energies for those configurations manifested that the extra Li atoms prefer to be localized at the Ti/Li_2O interface as well as at the free Li_2O surface rather than inside the slab. The extra charge storage at the interface between Ti and Li_2O is feasible since free surface of Li_2O is not applicable site in real cell environment. In addition, by observing the changes in charge, they clarified that the Li_2O surface would need to serve as host for Li while Ti serves as an

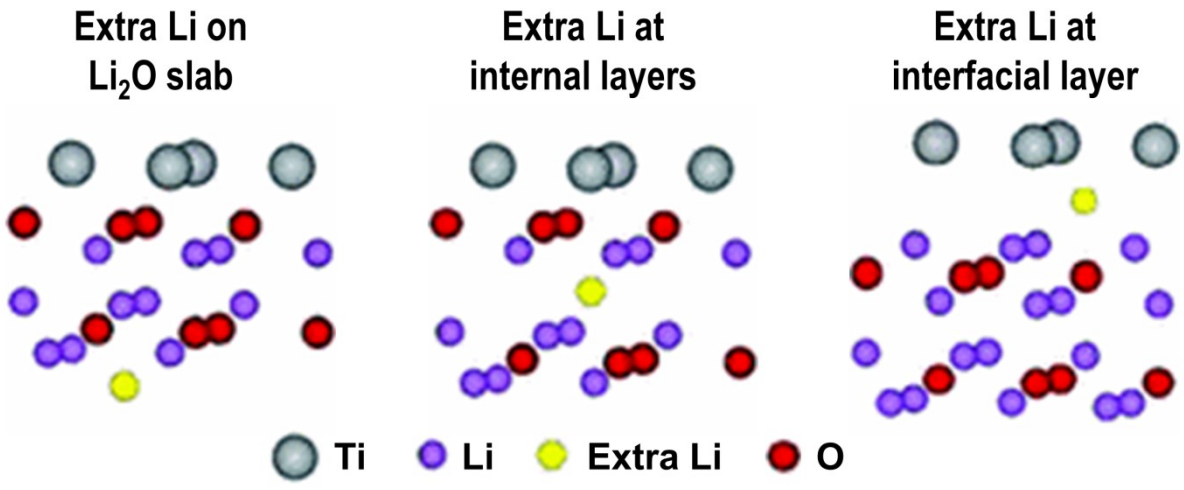

Figure 11. Graphical images of interfacial cross section of extra Li located at different position. (Reproduced with permission from Ref. xx, copyright (xxxx) xxxxx)

electron sink in this mechanism. By this process, Ti/Li_2O interface can store at least a monolayer of additional Li per interface. Similar behavior was predicted for Ru/Li_2O and Co/Li_2O interfaces.[153]

Hassan et al. further supported the interfacial charge storage mechanism by conducting DFT calculations of fully relaxed structures of $(RuO_2)_8$ upon addition of Li atoms.[154] The optimized structures with various amounts of Li are presented in **Figure 12(a)**. After addition of 1 mol Li per Ru (8 mol of Li in $(RuO_2)_8$ working cell), Li atoms were intercalated into the RuO_2 lattice, maintaining the original rutile structure with little disruption. Further lithiation generated significant distortions of the original crystal structure, especially after reaching a Li:Ru ratio of 3:1. The Ru atoms started to aggregate, and Li and O atoms were separated into relatively Ru-free domains at a Li:Ru ratio of 4:1, which is an indicator of the conversion of RuO_2. The sequential insertion and conversion reactions in RuO_2 are consistent with experimental observations. In cells containing islands of 8 Ru atoms surrounded by Li_2O with Li:Ru ratio of 4:1, described in **Figure 12(b)**, led to the prediction of extra charge storage in

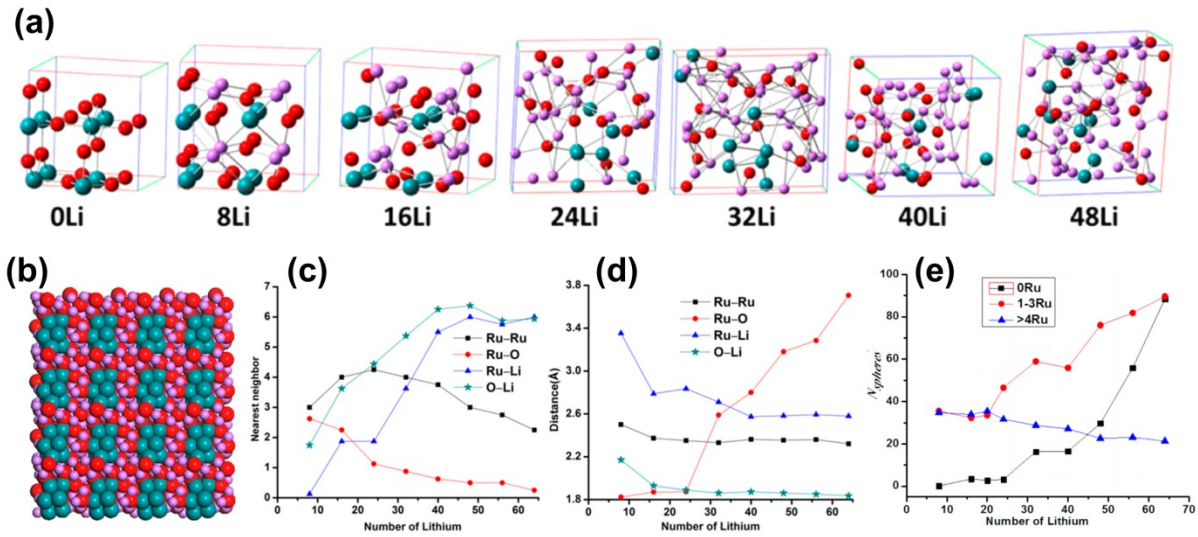

Figure 12. (a) Optimized structures of $(RuO_2)_8$ with varying numbers of lithium atoms added. (b) Three-dimensional image of optimized structures of a Ru_8 island in Li_2O. Ru : green, O : red, Li : purple. (c) Number of nearest neighbors, (d) average bond distance between coordinated atoms and (e) number of spheres in different regions as the number of lithium atoms increases. (Reproduced with permission from Ref. xx, copyright (xxxx) xxxxx)

the Ru + Li_2O system. It must be noted that the computation was conducted without electrolyte present. To investigate how the extra charge storage occurs in this configuration, they calculated the variation of the number of nearest neighbors and bond distances among Ru, O, and Li as displayed in **Figure 12(c) and (d)**. The number of Ru-Ru nearest neighbors gradually increased to maximum value after 3 mol of Li reaction and then continuously decreased at higher Li content. On the other hand, the number of Ru-O nearest neighbors significantly decreased during lithiation and almost approached to zero at higher Li concentration, and the distance between them increased above 3 mol of Li per Ru. Subsequently, the number of Li-O and Li-Ru nearest neighbors gradually increased until the Li:Ru ratio reached 5:1 and did not change much during further lithiation, showing that Li atoms appeared to form clusters at higher concentration. Also, the Ru-Li bond distance decreased with higher Li contents, indicating that the extra Li atoms would have a preference to insert between the Ru and Li_2O. **Figure 12(e)** shows the free volume without nearby Ru atoms, at the surface of Ru cluster, and in the core of Ru. During lithiation, the free volume fully isolated from Ru atoms (0Ru) and that near the surface of Ru clusters (1–3Ru) increased drastically, while the free volume in Ru metal (>4Ru) decreased gradually, further supporting that extra Li in such a system would favor the interfacial site between metallic Ru and Li_2O phase.

Bekaert et al. used ^6Li nuclear magnetic resonance (NMR) to probe the products of the electrochemical reaction of RuO_2 as shown in **Figure 13(a)**.[155] After 0.5 Li lithiation, two broad peaks at 9 and 0 ppm were observed, which can be assigned to $LiRuO_2$ and the formation of electrolyte reaction layers, respectively. After lithiation to 4 mol equivalents, the ^6Li NMR spectra changed significantly and then remained similar after full discharge and at the initial stages of delithiation. As shown in **Figure 13(b)**, the NMR spectrum for the fully discharged sample can be decomposed to three peaks at 0.48, 2.70 and 3.93 ppm. The intense

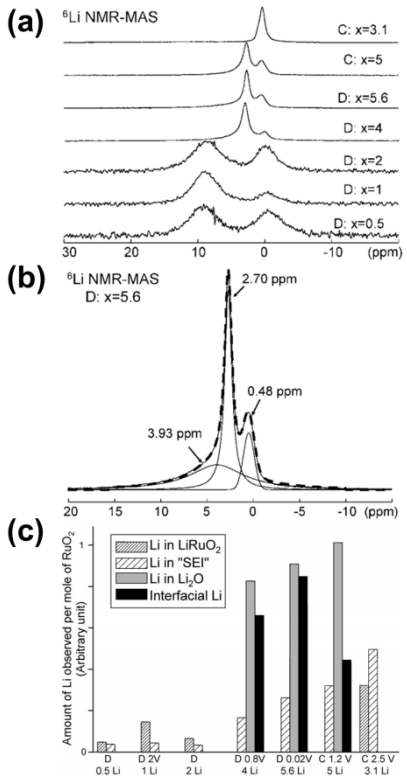

Figure 13. (a) ^{6}Li NMR spectra for RuO_2 electrode at different state of charge. x represent amount of Li per RuO_2. (b) Peak deconvolution of ^{6}Li NMR spectra at full discharged state. (c) Amount of Li observed by NMR per mass of samples in each signal for the various samples. (Reproduced with permission from Ref. xx, copyright (xxxx) xxxxx)

peak at 2.70 ppm corresponds to Li_2O formed by the conversion reaction, while the peak at 0.48 ppm was assigned to the electrolyte decomposition layer observed after initial lithiation. Another signal at 3.93 ppm could not be assigned to any Li-containing phase. The authors proposed that this signal emerged from the interfacial storage of Li. Based on the NMR results, they quantified the amount of Li from various components as shown in **Figure 13(c)**. The amount of Li_2O did not largely increase during lithiation from 4 to 5.6 mol equivalents of Li, while the new signal from the Li at the interface increased. During subsequent delithiation, this signal gradually decreased and totally disappeared at the full charged state, indicating reversible behavior.

Yu et al. prepared LiF/Ti nanocomposite thin films with 1:1 ratio and compared their electrochemical behavior with pure LiF and pure Ti.[156] As can be seen in **Figure 14(a)–(c)**,

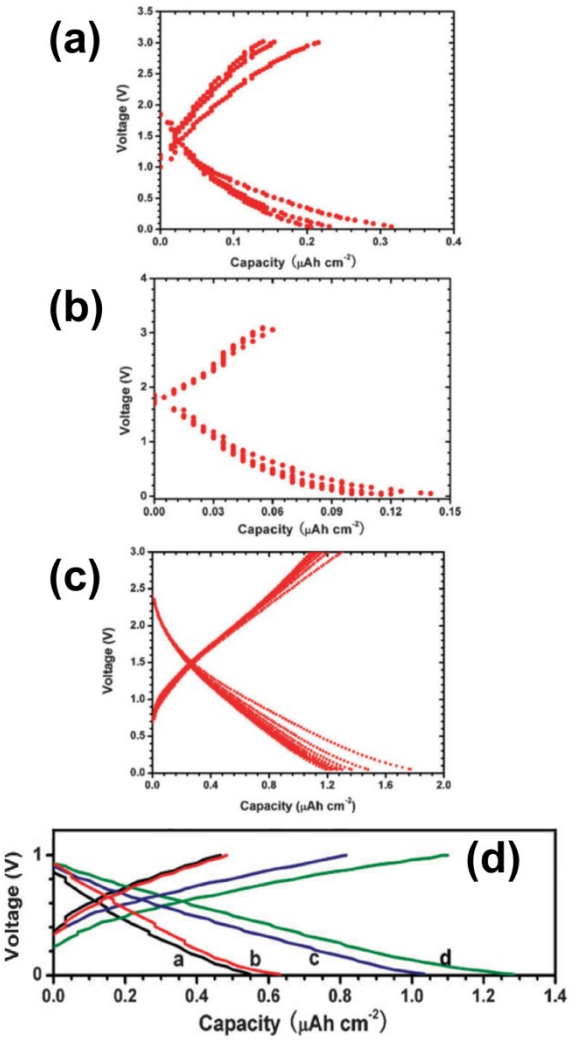

Figure 14. Voltage profiles of (a) Ti thin film (b) LiF thin film and (c) LiF/Ti (1:1) thin film on Ti pellet electrode with cutoff potential of 0.01–3.0 V . (d) Voltage profiles of LiF/Ti thin film with different deposition period of 30, 45, 60 and 90 min (a, b, c, d). (Reproduced with permission from Ref. xx, copyright (xxxx) xxxxx)

the LiF/Ti nanocomposite thin film exhibited 5–10 times higher capacity than single phase LiF and Ti thin film electrodes although the thickness and area of electrodes were the same for the three electrodes. In addition, the specific areal capacity of LiF/Ti thin film electrodes increased as their thickness increased as shown in **Figure 14(d)**. As the increase in thickness should not lead to an increase in surface area in a dense thin film, this dependence on thickness could not be explained by the formation and decomposition of electrolyte-derived surface layer. All this evidence was taken to suggest that the interfacial charge storage at regions between LiF and Ti phase can enhance the reversible capacity. The thickness

dependence was explained by the fact that the number of interfacial regions between the two phases increases as the thickness of the LiF/Ti electrode increases. They speculated that the capacity from interfacial charge storage could not be trivial when the interfacial area is substantially large enough, as in conversion reaction-based anode where the LiX/M phase coexists at small scale after completion of conversion reaction.

Guo et al. also discovered that reversible capacity is delivered in Fe/Li_3PO_4 nanocomposites, which were fabricated by discharging $LiFePO_4$ to 0.005 V.[157] The Fe and Li_3PO_4 nanograins remained inactive during subsequent charge to 4.2 V, as confirmed through HRTEM and XRD experiments. However, after the first process of nanocomposite formation, a capacity of ~220 mAh g^{-1} was reversibly delivered when the potential range was limited between 0.005 and 1.7 V as shown in **Figure 15(a)**. In contrast, a pure Li_3PO_4 electrode displayed only negligible capacity and the Fe remain as a metallic phase during charge/discharge. Furthermore, FTIR results showed that the surface layer components did not change until charging to 1.7 V. These observations led to the hypothesis that the reversible capacity is not delivered by electrolyte-derived surface layer decomposition, but from the interfacial charge storage between Fe and Li_3PO_4 phases. The capacitive behavior of Fe/Li_3PO_4 at low potentials, deduced from the shape of CV curves in **Figure 15(b)**, was reminiscent of the

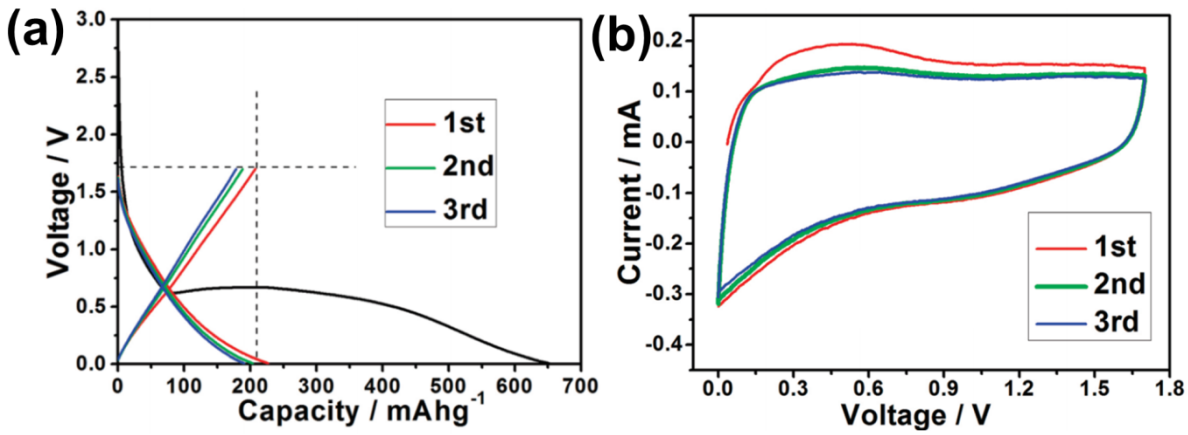

Figure 15. (a) The voltage profile and (b) CV curve of Fe/Li_3PO_4 between 0.005 and 1.7 V. (Reproduced with permission from Ref. xx, copyright (xxxx) xxxxx)

interfacial charge storage behavior.

Kim et al. investigated the charge storage mechanism of RuO_2 anodes and probed the possibility of interfacial charge storage using synchrotron-based *in situ* XRD and X-ray absorption spectroscopy (XAS) techniques with TEM, XPS, and galvanostatic intermittent titration technique (GITT).[158] Although RuO_2 can theoretically accommodate only 4 mol equivalents of Li (806 mAh g^{-1}) based on the conversion reaction, ~1130 mAh g^{-1} of capacity was delivered. The *in situ* XRD experiment showed that the original RuO_2 phase firstly transformed into the intermediate tetragonal Li_xRuO_2 phase during 0.65 mol equivalents of Li insertion. After insertion of 1 mol equivalents of Li, only orthorhombic $LiRuO_2$ was observed, indicating that the insertion occurred during the initial stage of discharge. Then, the peaks from $LiRuO_2$ steadily decreased until ~4 mol equivalents of Li was stored while a weak broad peak appeared that correspond to metallic Ru. The *in situ* XAS results also clearly showed the gradual rise of metallic Ru phase in this stage due to the conversion reaction. At the last stage of discharge where extra ~1.1 mol equivalents of Li was stored, the XRD pattern and XAS spectra remained unchanged. TEM results in **Figure 16(a)–(d)** show that the surface film layer from electrolyte decomposition began to form at 2.0 V and continuously grew as the discharge proceeded. However, the increase of thickness during discharge from 0.8 V to 0.05 V was considered not to be proportional to ~1.1 mol equivalents of Li storage, which would mean that the capacity in the sloping region at low potential cannot be fully ascribed to the growth and decomposition of the electrolyte-derived surface layer. Through GITT, as shown in **Figure 16(e)**, it was observed that the Li diffusion coefficient was relatively low during the conversion reaction region at 0.8 V plateau owing to its slow reaction, but it increased steadily again and reached steady-state maximum at the end of discharge where the extra charge storage occurred without the redox reaction of Ru. Based on the fact that the diffusion of Li into the Ru/Li_2O grain boundary naturally offers faster

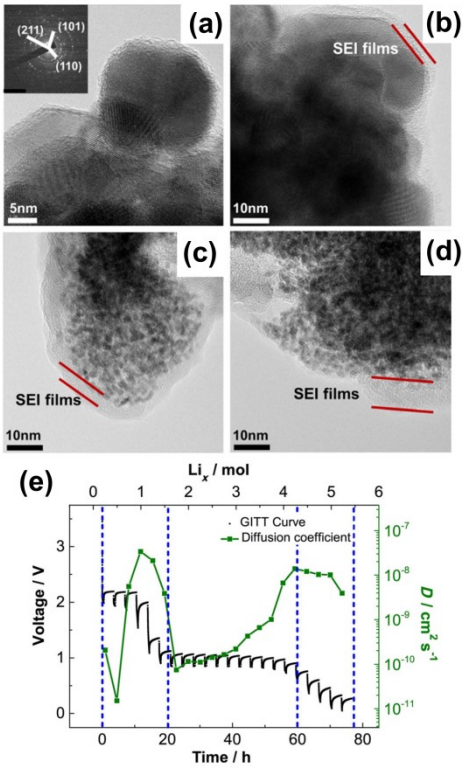

Figure 16. TEM images of (a) pristine RuO_2 powder, (b) discharged to 2.0 V, (c) discharged to 0.8 V and (d) full discharged to 0.05 V. (e) GITT curve and the calculated diffusion coefficient of RuO_2 electrode. (Reproduced with permission from Ref. xx, copyright (xxxx) xxxxx)

kinetics compared to a conversion reaction involving Li atoms, the authors proposed that the extra capacity at low potential region was delivered by the interfacial charge storage reaction.

In addition to the interfacial region of LiX/M derived from conversion reactions, interfacial charge storage has been proposed to occur if an electron accepting and a Li accepting phase are in contact at the atomic scale.[159–167] Shin et al. compared the electrochemical charge storage of nanoporous TiO_2 to commercial TiO_2 materials with the particle size of ~200 nm and 5–10 nm as shown in **Figure 17 (a)**.[159] As the particle size decreased, the total capacity increased due to an increase in activity below 1.5 V. However, in TiO_2, no conversion reaction can occur at these potentials, so Li_2O/Ti interfaces could not be formed. In this system, they hypothesized that the Li-inserted TiO_2 phase would serve as Li accepting phase and carbon additives or SEI layers would act as an electron acceptor. This mechanism was also suggested to operate in TiO_2/graphene and TiO_2/$Li_4Ti_5O_{12}$ composite electrodes as shown in **Figure 17(b) and (c)**. In the former, TiO_2 and graphene work as ion and electron

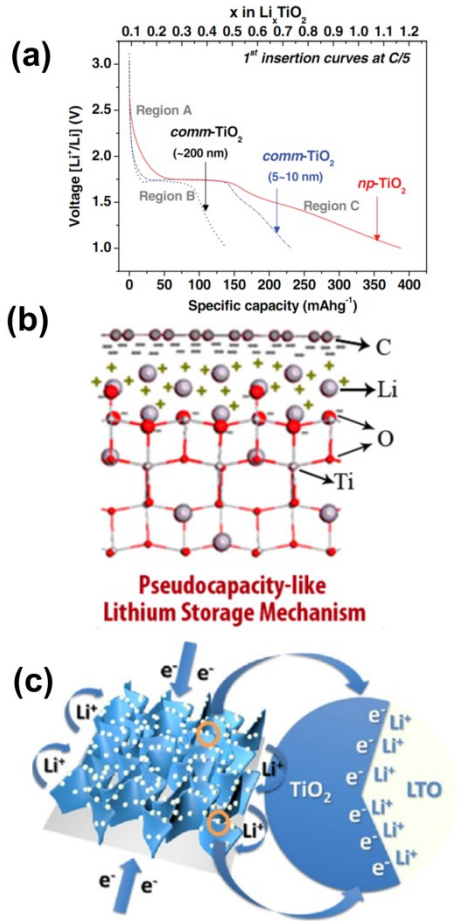

Figure 17. (a) Voltage profiles for two types of commercial TiO_2 particles with different grain sizes (~200, and 5–10 nm) and for nanoporous TiO_2. Sketch of Li storage at the interfaces between (b) graphene sheet and TiO_2 and (c) TiO_2 and $Li_4Ti_5O_{12}$. (Reproduced with permission from Ref. xx, copyright (xxxx) xxxxx)

acceptor, respectively.[162] However, it was proposed that TiO_2 might take electrons at the interface in the case of $TiO_2/Li_4Ti_5O_{12}$ composite while $Li_4Ti_5O_{12}$ takes Li^+ ions.[160]

The interfacial storage of charge is subject to significant controversy, with studies assessing that this mechanism cannot fully explain such large additional capacity beyond the theoretical value. In one example, Ponrouch et al. estimated the relative amount of available charge from the interfacial reaction mechanism by calculating the changes in volume and surface area after the conversion reaction.[168] Experimentally, Co_3O_4 anode materials delivered extra capacity of ~600 mAh g^{-1} beyond what would be expected from conversion, at low potential. Based on the calculations that the specific surface area of Co/Li_2O after conversion reaction of Co_3O_4 is ~100 m^2 g^{-1}, the capacitance of nanosized Co metal should be 2160 μF g^{-1} to deliver ~600 mAh g^{-1} of additional capacity solely from interfacial charge storage. However,

the maximum capacitance at the metal surface is only ~30 μF g^{-1}, which is significantly lower. Thus, they concluded that the interfacial reaction would be a negligible contributor to additional capacities beyond conversion. Further studies would clearly be needed to evaluate the experimental feasibility of this mechanism.

3.3. Redox Reactions of Li-Containing Species

In 2000, the report by Poizot et al. of the reversible electrochemical activity of nanosized transition metal oxides when reduced to their metallic state created a new paradigm by unveiling the fact that Li_2O formed by this conversion reaction, hitherto considered an inactive species, can be reversibly decomposed.[9] Similarly, years later, redox reactions were observed of other Li-containing species which had previously been considered as final products or electrochemically inactive species, delivering extra capacity.

In the midst of controversy over the origin of additional capacity in conversion reactions, Hu et al. suggested another possible mechanism accounting for it in RuO_2 electrodes using

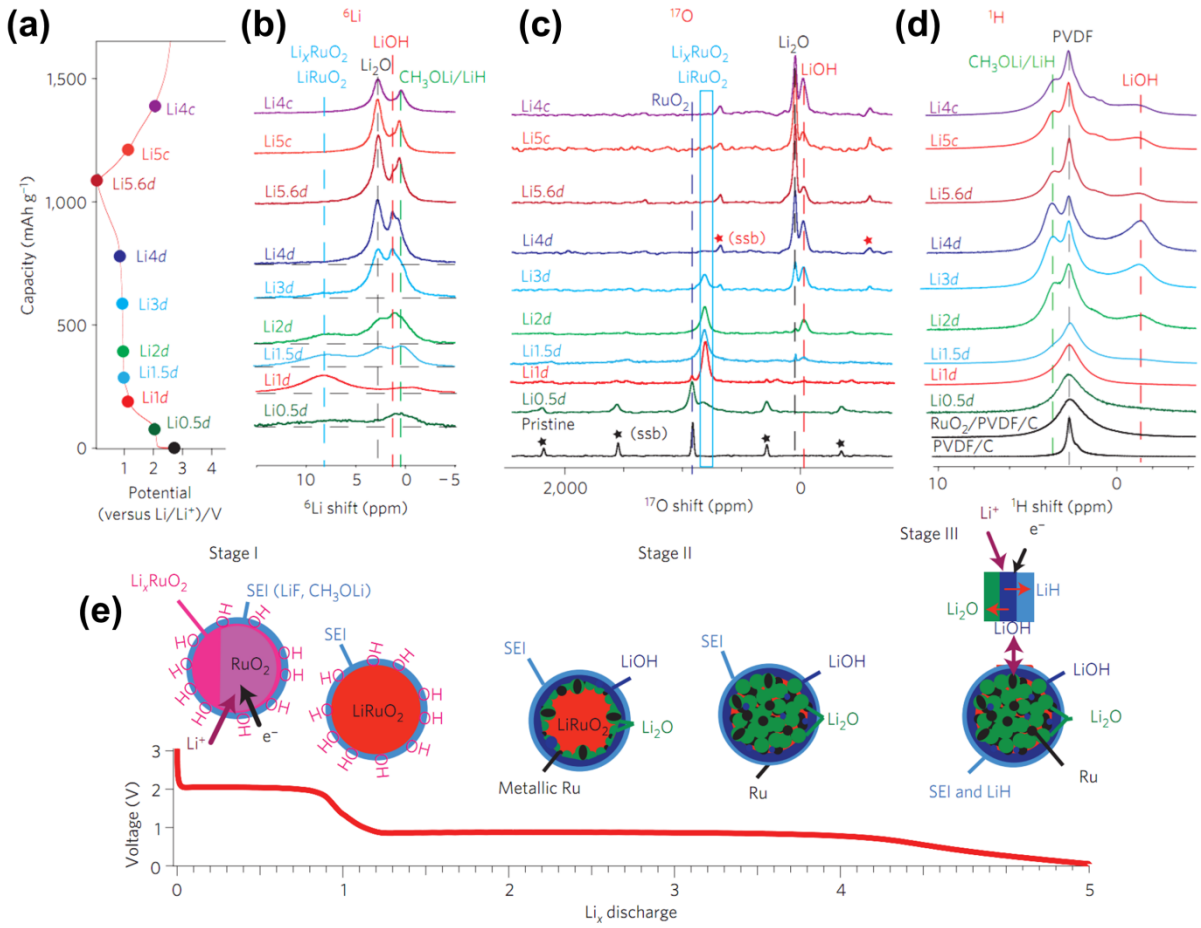

Figure 18. (a) Voltage profile of RuO_2 electrode. (a) ^6Li, (b) ^{17}O and ^1H NMR spectra of RuO_2 electrode cycled to various state of charge. (e) Sketch of Li storage performance representing the phase distribution at each stage of discharge (Reproduced with permission from Ref. xx, copyright (xxxx) xxxxx)

coupled NMR and synchrotron-based analyses: the generation of LiOH at the surface and its subsequent reversible reaction with Li to form Li_2O and LiH.[27] *Operando* pair distribution function (PDF) and XAS described that Li was inserted to RuO_2 to form tetragonal Li_xRuO_2 after reaction of 1.3 mol equivalents of Li. Then, in the plateau region at ~0.8 V, conversion occurs to form metallic Ru. At the low-potential sloping region after the plateau, where additional ~1.4 mol equivalents of charge storage occurred, both PDF and XAS data remained almost unchanged. To discover the origin of extra capacity at low potential, NMR analysis was conducted as described in **Figure 18(b)–(d)**. After 1 mol equivalents of Li was reacted, peaks appeared in ^{6}Li and ^{17}O NMR spectra which were assigned to Li_xRuO_2, consistent with PDF and XAS results. During further lithiation, these peaks gradually decreased while Li_2O peaks increased, as expected from a conversion reaction in this region. Simultaneously, ^{6}Li, ^{17}O, and ^{1}H NMR revealed the onset and growth of peaks corresponding to LiOH. This product was proposed to arise from the reaction of extra Li with –OH groups adsorbed at the surface of RuO_2/Li_xRuO_2. At the end of discharge, the intensity of these peaks decreased again, giving way to Li_2O and LiH peaks, suggesting that the capacity at low potential is originated from the reaction of LiOH ($LiOH + 2Li^+ + 2e^- \leftrightarrow Li_2O + LiH$). During subsequent charging, the LiOH peak intensity reversibly increased. The suggested lithiation mechanism of RuO_2 is summarized in **Figure 18(e)**.

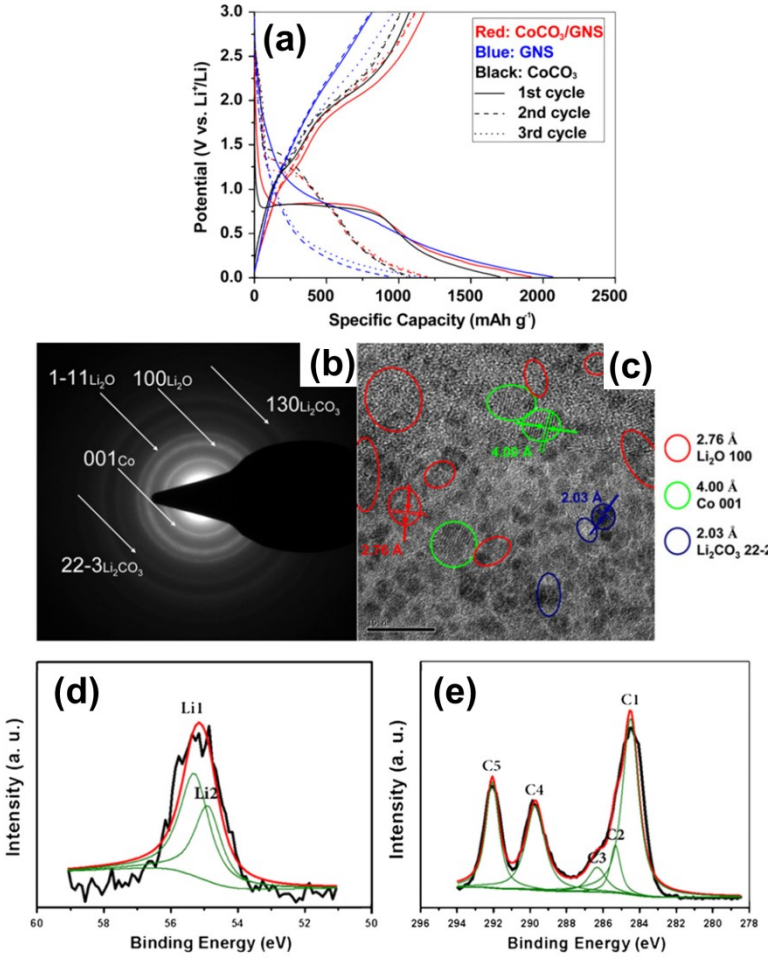

Figure 19. (a) Voltage profiles of $CoCO_3$/graphene, graphene and bare $CoCO_3$ electrodes. (b) SAED patterns, (c) HRTEM image, (d) Li 1s and (e) C 1s XPS spectra of full lithiated $CoCO_3$-PTFE electrode. (Reproduced with permission from Ref. xx, copyright (xxxx) xxxxx)

The electrochemical activity of Li-containing species formed during conversion reaction was also observed in other transition metal compounds. Traditionally, the final products of conversion reaction in MX are known as metallic phase (M) and Li_aX. However, some recent reports suggest that the Li_aX phase can additionally react with Li, delivering extra capacity. In carbonate-based anode materials ($M^{2+}CO_3$), much higher reversible capacity was delivered compared to its theoretical value corresponding to 2 mol Li accommodation.[169–172] To explore the origin of additional capacity in transition metal carbonates, Su et al. prepared $CoCO_3$ submicrocube/graphene composite electrodes and observed a capacity of 1317 mAh g^{-1}, greatly exceeding its theoretical value for a conventional conversion reaction ($CoCO_3 + 2Li^+ + 2e^- \leftrightarrow Co + Li_2CO_3$, ~450 mAh g^{-1}).[173] The authors proposed that C in Li_2CO_3 was reduced

to lower valence, leading to two stages of reduction reflected on the voltage profiles in **Figure 19(a)**: 1) reduction of Co^{2+} to Co^0 with the formation of Li_2CO_3 (plateau at ~0.8 V) and 2) reduction of C in Li_2CO_3 (sloping region below 0.8 V). After the first cycle, the plateau shifted toward 1.0–1.5 V. In charge, two oxidation peaks appeared at ~1.3 V and ~2.2 V, which is proposed to be close to the reversible oxidation potential of Li_2CO_3 and $CoCO_3$ based on their DFT calculation. To identify the electrochemical reaction products, HRTEM and XPS experiments were conducted with $CoCO_3$/PTFE electrode after full lithiation. The SAED pattern, HRTEM image and Li 1s XPS spectra in **Figure 19(b)–(d)** show that Li_2O coexists with conversion reaction products (Li_2CO_3 and Co metal phase). The C 1s XPS spectra after lithiation in **Figure 19(e)** shows a strong peak at 292.0 V from C=C bonds. They proposed that these results arose from reduction of C in Li_2CO_3 forming Li_2O and lower valence C. According to this mechanism, the theoretical capacity is considerably increased to ~1350 mAh g^{-1} by the reaction with 6 mol equivalents of Li.

Not long after this new reaction mechanism was proposed, Ding et al. fabricated $CoCO_3$–polypyrrole composites for anode materials, and observed a high reversible capacity of ~1382.6 mAh g^{-1} at the first charge, being as high as 1787 mAh g^{-1} in certain conditions.[174] They hypothesized that more Li can be inserted to low valence C in addition to reduction of C in Li_2CO_3, which might totally deliver 7 mol equivalents of Li (~1451 mAh g^{-1}). They also ascribed the excess capacity over the new theoretical value to the mechanisms of formation/decomposition of surface layers and interfacial charge storage described at 3.1 and 3.2. These studies have opened the possibility that Li_2CO_3 could be employed as a secondary redox center to provide extra capacity in transition metal carbonate anodes.[81,86,175–181]

If the additional reaction of Li_2CO_3 can be achieved, despite the same oxidation state and higher molecular weight, transition metal carbonates ($M^{2+}CO_3$) can deliver higher reversible

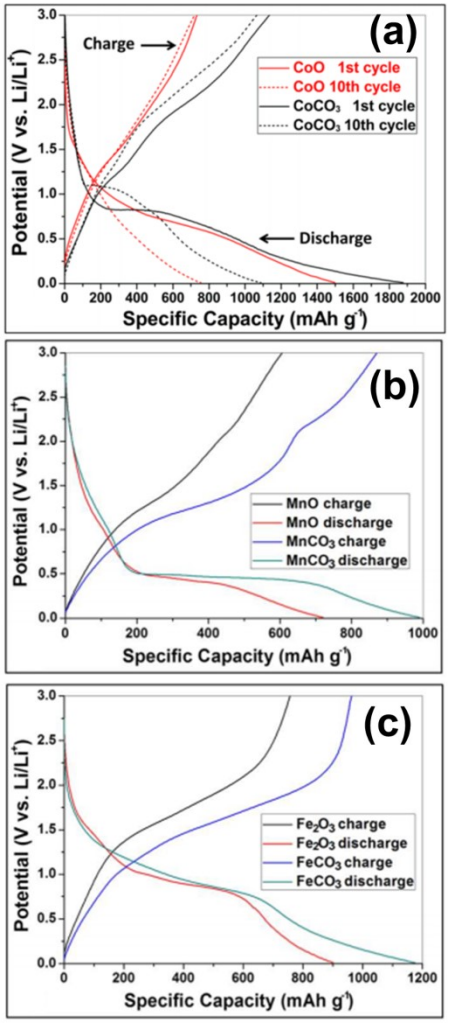

Figure 20. Voltage profile of (a) CoO and $CoCO_3$, (b) MnO and $MnCO_3$ electrodes, and Fe_2O_3 and $FeCO_3$. (Reprinted with permission from Ref. xx, copyright (xxxx) xxxxx).

capacity than transition metal oxides ($M^{2+}O$). To compare the electrochemical performance between them, Wang et al. quantified this comparison by evaluating $M^{2+}O$ and $M^{2+}CO_3$ micro-spindles prepared with similar morphology.[182] Electrochemical data for CoO and $CoCO_3$ in **Figure 20(a)** shows that the latter exhibited larger capacities of 1875 and 1135 mAh g^{-1} during first discharge and charge than the former (1497 and 804 mAh g^{-1}), with higher coulombic efficiency (60.5 % vs. 53.7 %). During repeated cycling, the specific capacity of $CoCO_3$ remained higher than CoO, demonstrating that the additional reaction continuously participates in $CoCO_3$. Similarly, $MnCO_3$ electrodes exhibited higher reversible

capacity than MnO as displayed in **Figure 20(b)**. In addition, despite the lower Fe oxidation

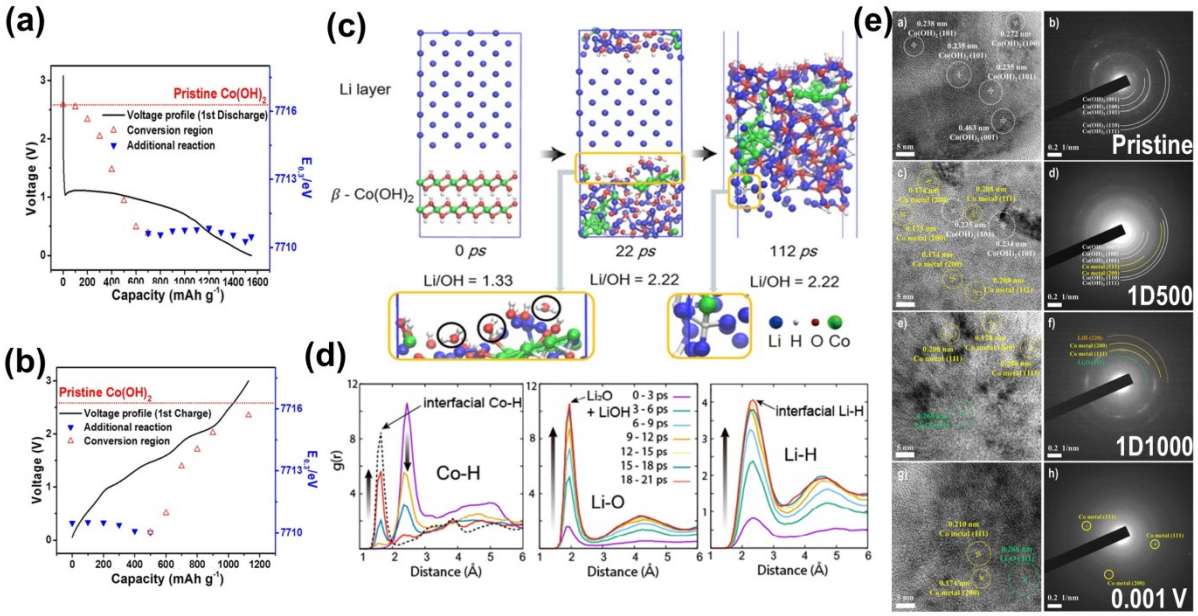

Figure 21. Changes in Co K-edge position with corresponding voltage profiles during (a) first discharge and (b) first charge. (c) Structure changes during lithiation obtained from molecular dynamics. (d) RDFs of Co-H, Li-O and Li-H. (e) HRTEM images and SAED patterns of electrode at the pristine state, after 500 mAh g^{-1} and 1000 mAh g^{-1} of capacity was delivered during discharge, and at full discharge. (Reproduced with permission from Ref. xx, copyright (xxxx) xxxxx).

state, larger capacity was delivered in $FeCO_3$ than Fe_2O_3 **(Figure 20(c))**.

Kim et al. discovered the exceptionally high reversible capacity of $Co(OH)_2$ (1112 mAh g^{-1}) far exceeding the theoretical value predicted based on a conversion reaction (577 mAh g^{-1}).[92] In the Co K-edge X-ray absorption near edge structure (XANES) acquired to investigate the origin of extra charge storage as shown in **Figure 21(a)**, the edge position decreased until ~700 mAh g^{-1} of capacity was delivered during discharge, due to the reduction of Co^{2+} to metallic Co. Then, below ~1.0 V, the edge position showed negligible shifts. During the subsequent charge, shown in **Figure 21(b)**, the opposite trend was observed. Initially, the Co K-edge remained almost unchanged, and it shifted toward higher energy due to oxidation of metallic Co through a reversible conversion reaction only after 500 mAh g^{-1} was delivered. Therefore, it was confirmed that the storage capacity at low potential was not related to the

redox process of Co atoms in $Co(OH)_2$. To get further insight into this process, ab initio molecular dynamics (AIMD) simulation was conducted with a multilayer geometry of $Co(OH)_2$ and metallic Li described in **Figure 21(c)**, which produced the radial distribution function (RDF) shown in **Figure 21(d)**. As reaction started, Li–OH bonds were predicted to form first, simultaneously breaking Co–OH bonds and inducing formation of small Co clusters, indicating the conversion reaction of $Co(OH)_2$. Further lithiation after the conversion reaction was confirmed to be originated from the migration of hydrogen in LiOH toward adjacent Co atoms, which resulted in the gradual increase of a peak due to the Co–H bond in the RDF. Since the hydrogen atoms bonded to Co cluster have roughly -1 charge state, an ionic bond could be formed between hydrogen anions and Li cations to form Li–H bonds at the interphase. Also, some portion of hydrogen seemed to move directly from OH to LiH. To further confirm the hydride reaction, HRTEM images and SAED patterns were collected as in **Figure 21(e)**. The images of the sample discharged up to 500 mAh g^{-1} shows metallic Co and LiOH, as expected from the conversion reaction of $Co(OH)_2$. After discharge to 1000 mAh g^{-1}, Co metallic clusters are dispersed in the Li_2O matrix, and the SAED patterns revealed the reflections of Li_2O and LiH as well as the metallic Co. The appearance of Li_2O and LiH suggests the reaction between Co metal and LiOH at low potential. At the end of discharge, due to total amorphization of the materials, SAED patterns reflected the characteristic amorphous halos. Based on the AIMD simulation and the experimental results including XAS and TEM, the overall sequential reactions were proposed as follows:

$$Co(OH)_2 + 2Li^+ + 2e^- \leftrightarrow Co + 2Li(OH) \quad (1)$$

$$Co + LiOH + Li^+ + e^- \leftrightarrow Co_xH_y(\text{interfacial}) \quad (2)$$

$$\alpha LiOH + 2\alpha Li^+ + 2\alpha e^- \leftrightarrow \alpha Li_2O + \alpha LiH \ (0 < \alpha < 1) \quad (3)$$

$$Co_xH_y\ (\text{interfacial}) + zLi^+ + ze^- \leftrightarrow Co_xH_{y-z} + zLiH \ (0 < z < y) \quad (4)$$

According to these reactions, three times higher capacity can be delivered compared to a conventional conversion. However, since the hydrogen anions can be formed only at the interphase between Co clusters and Li_2O/LiOH, and the larger Co clusters formed in the actual experiment would be less active, only ~4 mol Li was practically reacted reversibly in $Co(OH)_2$ anode.

Wu et al. tested graphene-covered and carbon-encapsulated $CoSO_4$ nanoparticles as anode materials.[183] According to the traditional conversion reaction, the metallic Co and Li_2SO_4 are expected as final reaction products after a full discharge process, accumulating 2 mol of Li. However, a reversible capacity equivalent to about 4 mol of Li was observed with $CoSO_4$ anode. In discharged electrodes, Li_2S, S clusters and Li_2O were reported by XRD and HRTEM images after the full discharge in **Figure 22(a)**. Thus, they suggested that Li_2SO_4 formed by the conversion reaction further reacted with Li to form Li_2S and Li_2O. By the sequential reactions, up to 8 mol equivalents Li could be accommodated with $CoSO_4$ as follows:

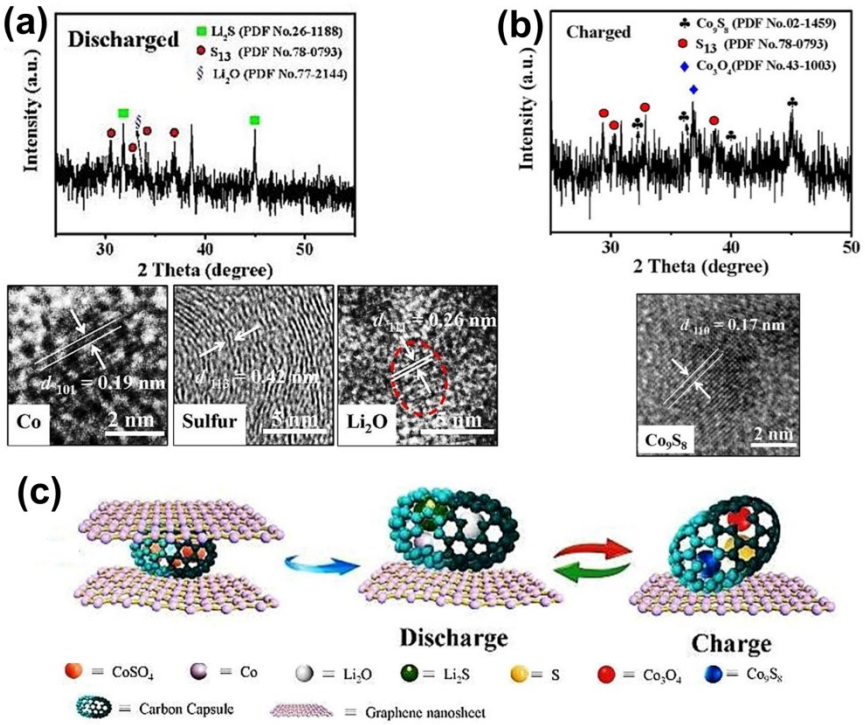

Figure 22. XRD patterns and TEM images of the samples after (a) the first discharge and (b) the first charge. (c) Schematic illustration of the Li storage behavior in graphene-covered and carbon-encapsulated $CoSO_4$ nanoparticles. (Reproduced with permission from Ref. xx, copyright (xxxx) xxxxx).

$$CoSO_4 + 2Li^+ + 2e^- \rightarrow Co + Li_2SO_4 \quad (5)$$

$$Li_2SO_4 + 8Li^+ + 8e^- \rightarrow Li_2S + 4Li_2O \quad (6)$$

After charge, Co_3O_4 and Co_9S_8 were detected as in **Figure 22(b)** instead of restoring the original phase, leading to the proposed reactions:

$$9Co + 8Li_2S \leftrightarrow Co_9S_8 + 16Li^+ + 16e^- \quad (7)$$

$$3Co + 4Li_2O \leftrightarrow Co_3O_4 + 8Li^+ + 8e^- \quad (8)$$

$$Li_2S \leftrightarrow 1/x\ S_x + 2Li^+ + 2e^- \quad (9)$$

At maximum, 2.67 mol Li per Co would be expected to react during charge, which is higher than the amount based solely on the conversion reaction mechanism. The proposed reaction mechanism of the graphene-covered and carbon-encapsulated $CoSO_4$ nanoparticles is summarized in **Figure 22(c)**.

At this stage, the electrochemical activity of the non-metallic product of the conversion reaction, Li_nX_b, has been demonstrated in a variety of chemical systems. Beyond those mentioned above, metal acetates, which can convert to metal and Li acetate (LiAc), followed by further reaction of the latter with Li to form CH_3CHO and Li_2O, delivering extra

capacity.[60] Also, simultaneous reaction of other products of conversion reactions was observed in transition metal compounds possessing multiple ligands such as $Co_2(OH)_2(CO)_3$,[90,184,185] $Co(Ac)_{2-x}(OH)_x$[60] and $Ni(HCO_3)_2$.[186–188]

Complex versions of these compounds worthy of further discussion are metal-organic frameworks (MOFs). Very recently, MOFs have been the focus of extensive investigation as anode materials due to unique properties such as controlled pore size, redox activity, structural diversity and well-established post-process methode.[189–201] In analogy to transition metal oxides, the conversion reaction occurs in MOFs inducing the reduction of transition metal and formation of Li-containing organic species as final products.[194,201,202] In 2015, however, Lee et al. discovered that further charge was passed after completion of the conversion reaction at nickel(II) terephthalate (NiTP), delivering a high capacity of ~1100 mAh g^{-1}.[195] This value is remarkably higher than the theoretical capacity of ~240 mAh g^{-1} based on an expected two-electron conversion reaction. The mechanism of lithiation of NiTP was probed using Ni K-edge XAS and ^{13}C NMR experiment, as shown in **Figure 23(a)–(c)**. Ni K-edge XANES spectra in **Figure 23(a)** revealed that the initial Ni^{2+} state completely reduced to Ni^0 during discharge to 1.1 V, demonstrating that the following conversion reaction was completed at the initial stage of discharge.

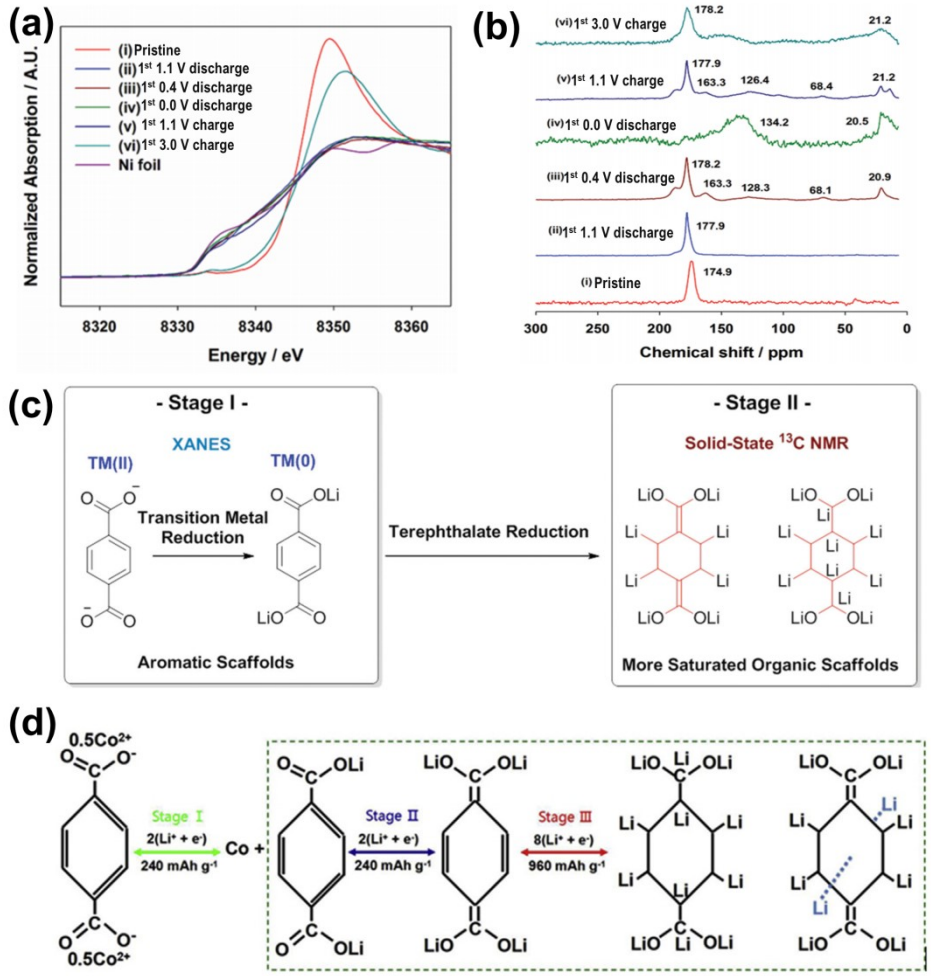

Figure 23. (a) Ni K-edge XANES spectra and (b) solid state ^{13}C NMR spectra of NiTP electrodes during the first cycle. Proposed reaction mechanism in (c) transition metal terephthalate electrodes in ref xx and (d) CoTP in ref xxx. (Reproduced with permission from Ref. xx, copyright (xxxx) xxxxx)

$$NiC_8H_4O_4 + 2Li^+ + 2e^- \leftrightarrow Ni + Li_2C_8H_4O_4$$

The redox state of Ni remained almost unchanged upon further discharge and until re-charging to 1.1V. After further re-charging to 3.0 V, the re-oxidation of Ni was observed. Thus, there were additional reactions accounting for the extra capacity below 1.1V. They were inspected using ^{13}C NMR, as provided in **Figure 23(b)**. During discharge to 1.1 V, where the conversion reaction occurred, no obvious changes were observed. After discharge to 0.4 V, a new peak at 163 ppm was observed, which could be ascribed to a highly conjugated enolate. At 0.0 V, two broad bands at 134.2 and 20.5 ppm were observed, corresponding to more saturated structures. Thus, they speculated that the organic ligand in Li containing organic compounds generated by the conversion reaction act as redox center to form saturated organic scaffolds, similar to what was also observed in organic electrodes.[189,203–207] FeTP also showed similar voltage profile and behavior.[195] Overall, the

general lithiation to transition metal terephthalates can be summarized as **Figure 23(c)**. First, the reduction of transition metal occurs through a conversion reaction, then, extra Li is stored at the organic ligands to develop saturated organic scaffolds. The second lithiation step can be sub-divided into two-steps in some cases, namely, enolization of carboxyl group (stage II) and vinyl to complete saturated bond (stage III) as described in **Figure 23(d)**.[193,198,199] Similar activity of other organic ligands was also observed after the conversion reaction of the corresponding transition metal-organic frameworks.[192,193,196,198,199]

In summary, **Table 3** lists the known electrochemical reactions of various Li-containing species. Similar to the formation/decomposition of electrolyte-derived surface layer, the redox reactions of Li-containing species are generally considered to be facilitated by the catalytic effects of metal nanoparticle. Thus, it can be inferred that governing the metal side will affect the abnormal charge storage behavior. With the participation of Li-containing species in redox reactions induced by the generation of metal nanoparticles during cell operation, the theoretical capacity of electrode materials can be largely expanded. Given the value of exceeding capacity of the anode through this mechanism, this prospect should be further explored in follow-up research. Nonetheless, the experimental studies on the redox reaction of Li-containing species available so far are usually focused on the 1st cycle behavior. The reversible redox process of Li-containing species should be further confirmed for extended cycling.

Table 3. Brief summary of reactions of Li-containing species observed in various anode materials.

Starting materials	Electrochemical reaction	Ref
H_2O at RuO_2 surface	$LiOH_{surface} + 2Li^+ + 2e^- \leftrightarrow Li_2O + LiH$	27
Li_2CO_3 after conversion reaction of $CoCO_3$	$Li_2CO_3 + (4 + 0.5x)Li^+ + (4 + 0.5x)e^-$ $\leftrightarrow 0.5Li_xC_2$ (x = 0, 1, 2) + $3Li_2O$	173,174
Li_2SO_4 after conversion reaction of $CoSO_4$	$Li_2SO_4 + 6Li^+ + 6e^- \rightarrow S + 4Li_2O$ $S + 2Li^+ + 2e^- \rightarrow Li_2S$	183
LiOH after conversion reaction of $Co(OH)_2$	$Co + LiOH + Li^+ + e^- \leftrightarrow Co_xH_{y\ (interfacial)}$ $\alpha LiOH + 2\alpha Li^+ + 2\alpha e^- \leftrightarrow \alpha Li_2O + \alpha LiH$ $(0 < \alpha < 1)$ $Co_xH_{y\ (interfacial)} + zLi^+ + ze^- \leftrightarrow Co_xH_{y-z} + zLiH$ $(0 < z < y)$	92
LiAc after conversion reaction of $Co(Ac)_{0.48}(OH)_{1.52}\cdot 0.55H_2O$	$LiAc + Li^+ + e^- \leftrightarrow CH_3CHO + Li_2O$	60
Metal-organic-frameworks (MOFs)	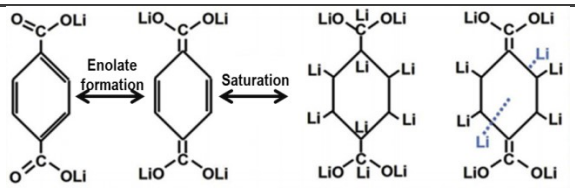	192,193,196,198,199

3.4. Li storage in defects and metallic cluster-like Li storage

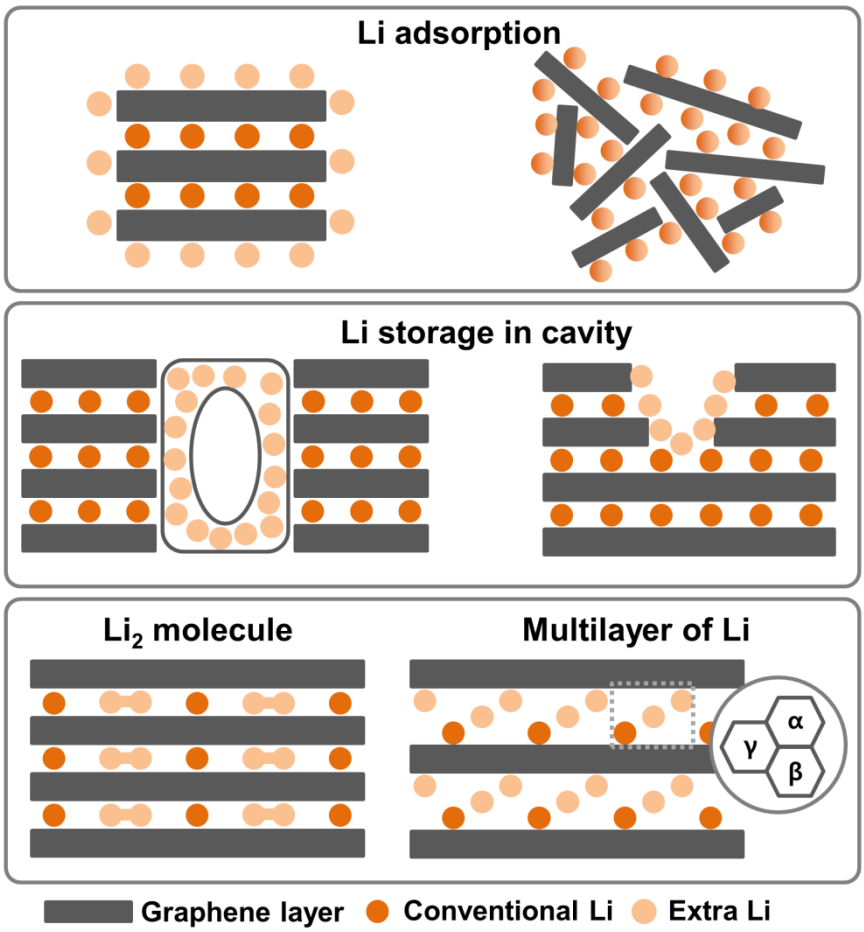

Figure 24. Unconventional extra Li storage mechanism in carbonaceous anode materials (Reproduced with permission from Ref. xx, copyright (xxxx) xxxxx)

There have been numerous reports that the practical capacity of certain modified carbonaceous anode materials exceeds the theoretical value of 372 mAh g^{-1}.[6,7,208–216] Different models based on microstructural effects have been proposed to explain the extra capacity in those electrodes as displayed in **Figure 24**. In carbonaceous materials, it was reported that the extra Li atoms could be accommodated in defects such as surface and pores, or by forming metallic Li-rich phase. Some reports suggest that additional Li can be absorbed at the surface and edge of graphite,[217–219] or toward hydrogen-terminated edges.[216,220] In disordered carbonaceous materials, Liu et al. proposed that Li can be adsorbed on both sides of the randomly arranged single-layered sheets named as "house of cards".[6,221] In addition, mechanisms that Li could be accommodated in microcavities were also suggested.[211,222]

Other reports proposed that multilayers of metal-like Li or Li_2 covalent molecules can be stored between graphene sheets with significantly increased interslab distance, instead of classical Li accommodation to form monolayers in cationic state.[7,223] However, it was also reported that the Li storage capacity of single-layer graphene sheets is inferior to the graphite due to the repulsion between the Li absorbed on both side of graphene sheets,[224,225] and that the reaction of Li with functional groups in carbonaceous materials is irreversible,[226] raising issues on the feasibility and reversibility of those mechanisms.

Morphology-controlled nanomaterials generally exhibit enhanced cycle and rate characteristics compared to bulk counterparts.[50,227–229] In addition, defect sites and pore structures introduced when materials are tailored at the nanoscale can act as extra redox centers, providing additional Li accommodation sites. The additional charge storage from defects is commonly observed in intercalation electrode materials. Especially, reducing size in nanoscale provide significantly enlarged electrolyte/electrode contact area where the electrochemical reaction takes place, greatly improving the reaction kinetics and facilitating the surface reaction.[230–237] As electrode materials are increasingly prepared at the nanoscale to improve electrochemical performance, surface and grain boundaries become more prominent compared to bulk counterparts. This effect can result in electrochemical properties that are notably different.

As a classical example, bulk anatase TiO_2 cannot be fully lithiated to $LiTiO_2$ because the Li ion diffusion is interrupted by the full occupation of the octahedral sites. However, transformation to this same $LiTiO_2$ phase could be possible in near the surface of TiO_2 owing to the short diffusion pathway.[238,239] As a result, TiO_2 synthesized at the smallest possible sizes, where the surface contribution to the ensemble average of material is very large, is converted to $LiTiO_2$ while larger TiO_2 particles only show orthorhombic $Li_{\sim 0.5}TiO_2$ after full lithiation (**Figure 25(a)**). As a result, the Li storage capability can be extended from ~0.5 to 1

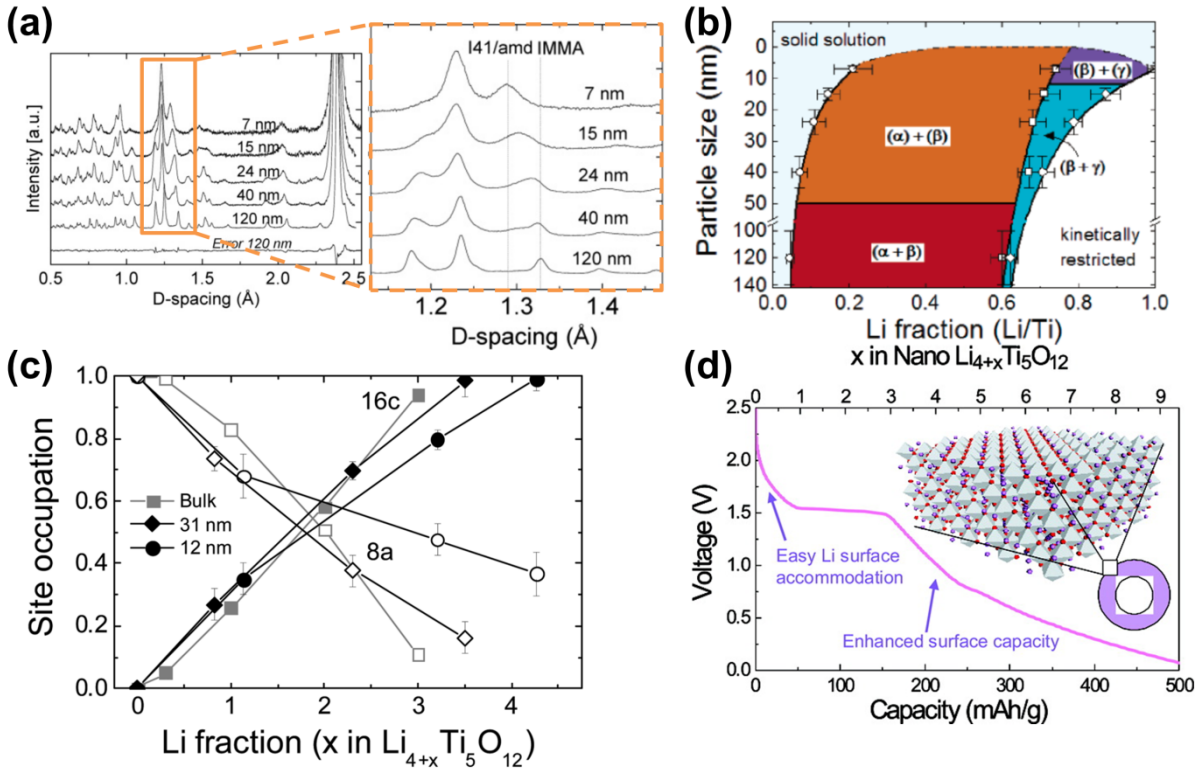

Figure 25. (a) Neutron diffraction patterns of full lithiated Li_xTiO_2 for different particle sizes (b) Solubility limits in anatase Li_xTiO_2 where α, β, and γ represent anatase, Li-titanate, and $LiTiO_2$ respectively. (c) Li occupancy of the 8a (closed symbols) and 16c (open symbols) sublattices in spinel $Li_{4+x}Ti_5O_{12}$. (d) Illustration of the Li storage behavior in nanosized $Li_4Ti_5O_{12}$ with voltage profile (Reproduced with permission from Ref. xx, copyright (xxxx) xxxxx)

in nanosized TiO_2 as described in **Figure 25(b)**. Similar behavior was observed in $Li_4Ti_5O_{12}$. In the pristine state of microsized $Li_4Ti_5O_{12}$, all the tetrahedral 8a sites are completely filled by Li, resulting in $(Li_3)_{8a}[Li_1Ti_5]_{16d}(O_{12})_{32e}$ structure. Upon discharge to 0.01 V, Li ions are inserted into the octahedral 16c site and Li ions in the tetrahedral 8a site of the pristine $Li_4Ti_5O_{12}$ also moved to the octahedral 16c site forming $Li_7Ti_5O_{12}$ phase at full lithiation, where the 16c sites are fully occupied ($[Li_6]_{16c}[Li_1Ti_5]_{16d}(O_{12})_{32e}$) and the 8a sites remain empty. The remaining 8a site become energetically unfavorable for accommodating Li ion due to the short Li-Li distances of $Li_7Ti_5O_{12}$ phase.[239–241] However, some nanosized $Li_4Ti_5O_{12}$ exhibited higher Li accommodation.[239,240,242–244] The fractional Li occupation in 8a and 16c sites in $Li_4Ti_5O_{12}$ depending on particle size is shown in **Figure 25(c)**.[240] It clearly shows that the 8a sites were partially occupied in the fully discharged state in the case of the smallest

particles, whereas only 16c sites were occupied in micron-sized $Li_4Ti_5O_{12}$. Due to the short diffusion pathways, additional Li can be inserted in the energetically unfavorable 8a site only at nanosized $Li_4Ti_5O_{12}$ where there are many more atoms in near-surface environments compared to bulk materials. At deeper levels of lithiation, simultaneous Li occupation in both 8a and 16c site will hinder diffusion pathway, and thus Li is inserted only to 16c site. At the nanoscale, however, additional Li can be stored in the 8a site after filling 16c site as the surface contribution increases, exhibiting higher capacity as described in **Figure 25(d)**.

Boundaries between crystalline grains, as depicted in **Figure 26(a)**, can also offer sites for unconventional Li storage. They act as channel for Li ions and atoms in the grain boundary

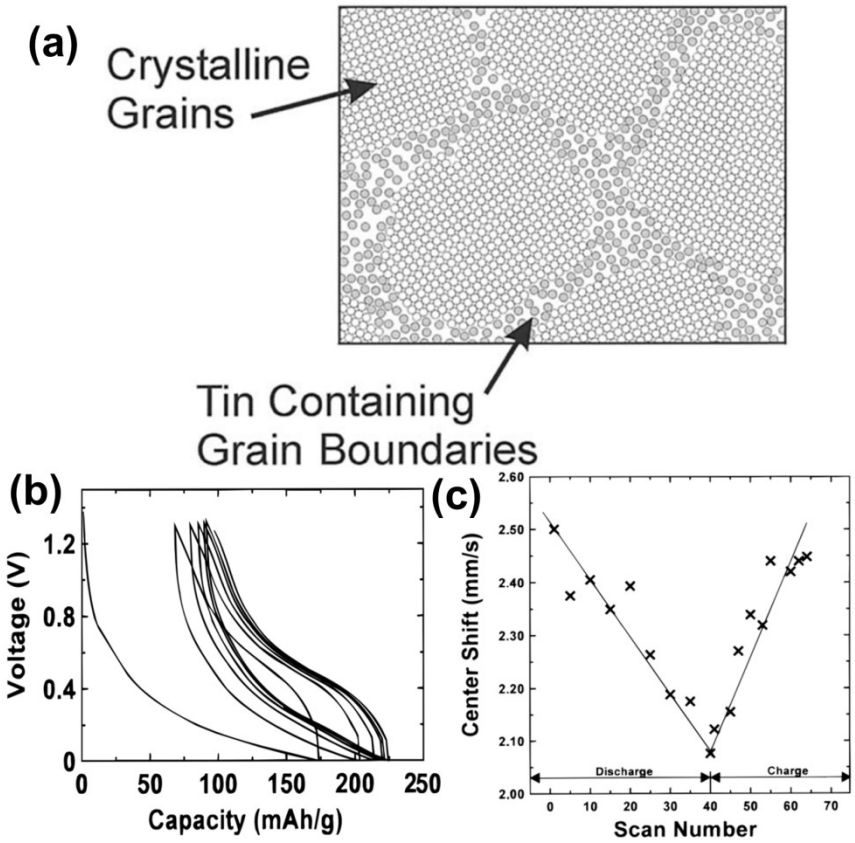

Figure 26. (a) Sketch of nanostructured materials with crystalline grains and atoms in the grain boundaries. (b) Voltage profiles of nanocrystalline $SnMn_3C$ electrode. (c) Changes in center shift for grain boundary Mössbauer absorption peak during the first cycle. (Reproduced with permission from Ref. xx, copyright (xxxx) xxxxx)

can also react with them.[245] $SnMn_3C$ offers an example of this reactivity. Although it is known to be inactive toward Li, nanostructured $SnMn_3C$ that composed of small grains (~12 nm) delivered reversible capacity of ~150 mAh g^{-1} corresponding to 1.5 mol of Li insertion as in **Figure 26(b)**. The changes in center shift of the peak assigned to Sn existing at the grain boundary at Mössbauer absorption spectra during first cycle are shown in **Figure 26(c)**. It changed from ~2.5 mm s^{-1} to lower value during discharge and changed in opposite direction during subsequent charge, while the Sn at crystalline grains and surface contaminated SnO_x phase did not change during cycling. Thus, the *in situ* Mössbauer spectra results show that the Li only reacted with Sn at grain boundaries, which could be reversibly delithiated.

Disordered phases also form an additional Li pathway to convert inactive sites into

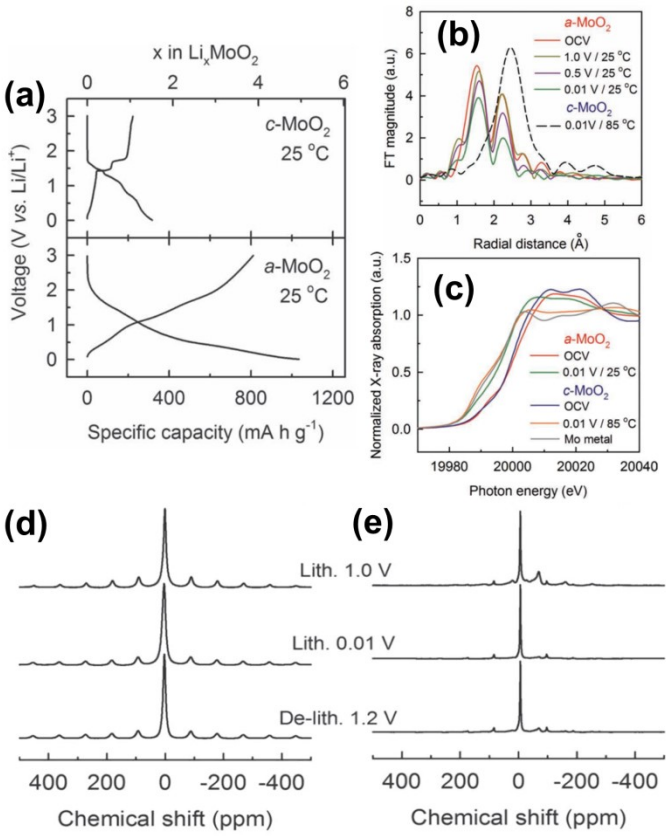

Figure 27. (a) The voltage profiles of c-MoO_2 and a-MoO_2 during the first cycle. Variations of (b) Fourier transform magnitude of EXAFS, (c) XANES spectra with lithiation. Changes in ^6Li MAS NMR data of (d) a-MoO_2 and (e) c-MoO_2 harvested at different points during cycling. (Reproduced with permission from Ref. xx, copyright (xxxx) xxxxx)

energetically favorable sites. Ku et al., proposed that the additional Li can be reversibly stored at structural vacant sites in amorphous metal oxides.[246] As shown in **Figure 27(a)**, amorphous MoO_2 (a-MoO_2) accommodated much higher Li amount and the voltage profile was quite different from that of crystalline MoO_2 (c-MoO_2). The plateaus in the voltage profile of a-MoO_2 are significantly diminished to give a rather sloping profile in the whole potential range, indicating that the Li^+ storage sites are not discrete and electrochemically nonequivalent in amorphous phases. Although the XAS experiments in **Figure 27(b) and (c)** clearly demonstrated Mo metal phase in full discharged c-MoO_2 electrode when operated at 85 °C, Fourier transform of extended X-ray absorption fine structure (EXAFS) spectra of lithiated a-MoO_2 did not show the signal from metallic Mo although the oxidation state of Mo was close to (but not perfectly) 0. The XAS results described that the conversion reaction did not occur in a-MoO_2 even if the reversible capacity was close to the theoretical value of conversion reaction. They describe the high capacity in a-MoO_2 by Li accommodation at the structural defects while the Mo^{4+} ions act as redox center. There were numerous structural defects to host such a large amount of Li ions in a-MoO_2. As the defects are electrochemically non-equivalent, the electrochemical result showed wide range of lithiation potential. The different Li accommodation site in a-MoO_2 compared with c-MoO_2 can be identified by magic angle spinning ^{7}Li NMR spectra in **Figure 27(d) and (e)**. While only a few discrete sites existed in c-MoO_2 represented by one sharp peak with some weaker ones, a single broad peak appeared in a-MoO_2 demonstrating wide distribution of Li storage site. Similar to a-MoO_2, amorphous V_2O_5 (a-V_2O_5) shows non-equilibrium (de)lithiation with a largely featureless voltage profile, in contrast to crystalline materials (c-V_2O_5) as shown in **Figure 28(a)**.[247] In a-V_2O_5, the relatively randomly arrangement of atoms is predicted to make a high population of defects available, including vacancies or interstitial sites. The Li can subsequently and reversibly be inserted into these sites without phase transitions, as

illustrated in **Figure 28(b)**. As a result, a-V_2O_5 exhibited better cycle performance and higher reversible capacity compared to c-V_2O_5, where an irreversible phase transition from layered structure to rock-salt structure occurs and leads to failure.

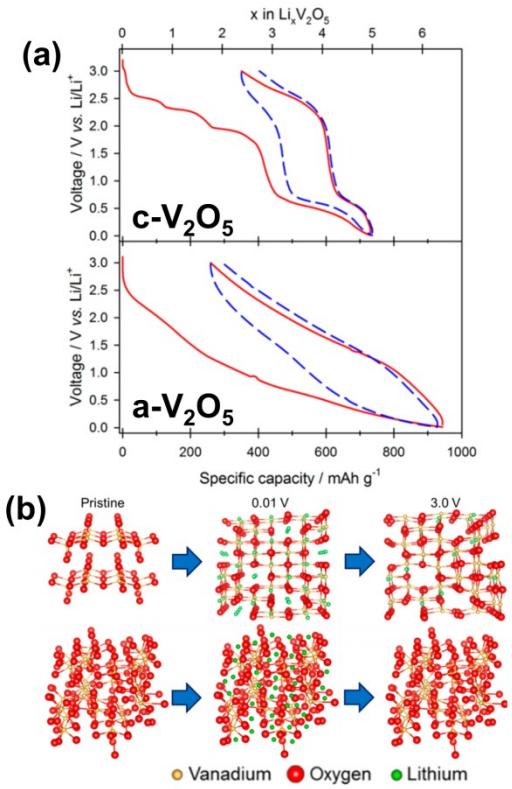

Figure 28. (a) Voltage profiles of crystalline and amorphous V_2O_5 and (b) Schematic representation of structural changes upon cycling (Reproduced with permission from Ref. xx, copyright (xxxx) xxxxx)

As mentioned earlier, additional Li ions are gathered and form metallic cluster in cavities or pores between graphene layers in some carbonaceous materials, as well as Li insertion between graphene layers. Likewise, Shon et al. observed that extra Li storage occurred as a form of metallic Li cluster during lithiation in ordered mesoporous MoO_2.[95] Previously, it was reported that ~1 mol equivalents of Li insertion reaction firstly occurs with reduction of

Mo^{4+} to Mo^{3+} and then conversion reaction occurs to form metallic Mo and Li_2O.[248,249] Thus, theoretical capacity based on the above mechanism is ~838 mAh g^{-1} corresponding to 4 mol equivalents of Li reaction. However, mesoporous MoO_2 exhibited a huge capacity of 1,814 mAh g^{-1} for the first discharge, more than twice of its theoretical value based on conversion reaction. The reversible capacity of 1,308 mAh g^{-1} during first charge also exceeded the theoretical capacity. The origin of extra capacity was explained by using *in situ* synchrotron-based analyses, TEM with electron energy loss spectroscopy (EELS) and computational modeling. Although the Mo K-edge position shifted toward lower energy, the conversion reaction products, metallic Mo phase and Li_2O phase, were not observed in EXAFS and XRD patterns during cycling. **Figure 29(a)** describes Li accommodation in mesoporous MoO_2 based on DFT calculation. Up to reaction of 1.5 mol equivalents of Li, the insertion reaction occurred with relatively small expansion of original monoclinic MoO_2 phase. Further Li insertion results in phase separation of Li inserted monoclinic MoO_2 phase into the lithiated crystalline MoO_2 phase and Li-rich amorphous phase. During the phase separation, additional Li atoms go near the Li position of Li-rich amorphous phase. This near-neighbor Li site is

more energetically favorable as a new position than a random position. With increasing depth of Li layers, interatomic distances between Li atoms tend to decrease suggesting the formation of Li metallic clusters. The HRTEM and EELS studies on the fully lithiated and delithiated MoO_2 electrode supported the idea of metallic Li cluster storage. In the HRTEM images in **Figure 29(b)**, three regions can be observed; crystalline phase (D_{CP}), amorphous phase (D_{AP}) and SEI phase (D_{SEI}). The EELS spectra of each region are shown in **Figure 29(c)**. While the EELS at D_{CP} were assigned to Li_xMoO_2, metallic Li phase was observed in D_{AP}, indicating existence of Li-rich region. The Li cluster storage mechanism of mesoporous MoO_2 is summarized as in **Figure 29(d)**.

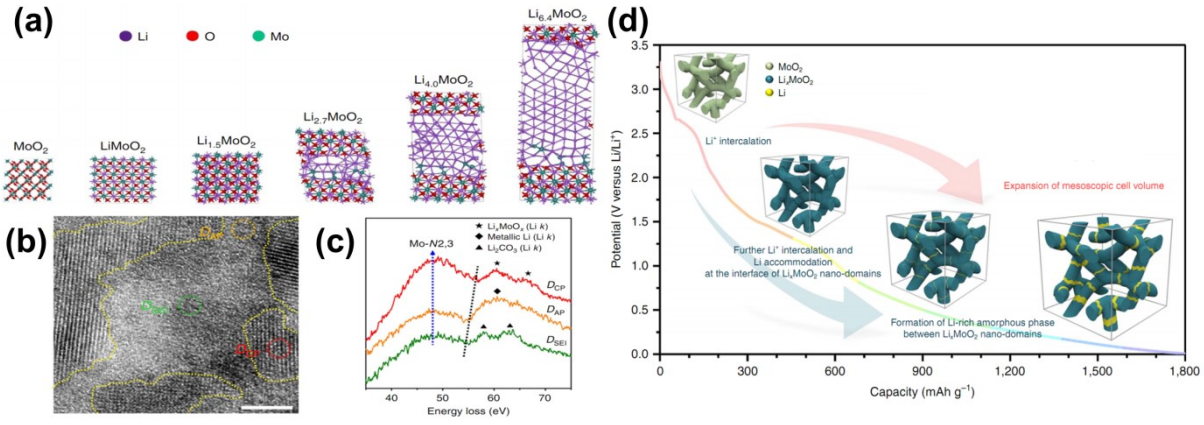

Figure 29. (a) Snapshots of the ordered mesoporous MoO_2 electrode with the increase of Li inserted, calculated by DFT. (b) HRTEM image of the full discharged ordered mesoporous MoO_2 demonstrating the formation of three different phases: crystalline (D_{CP}), amorphous (D_{AP}) and SEI region (D_{SEI}), and (c) EELS spectra taken from areas D_{CP}, D_{AP} and D_{SEI}. (d) Schematic diagram of reaction pathway and the resulting products of ordered mesoporous MoO_2 with respect to the amount of Li ion inserted. (Reproduced with permission from Ref. xx, copyright (xxxx) xxxxx)

3.5. Increasing Capacity upon Cycling, or "Negative Fading"

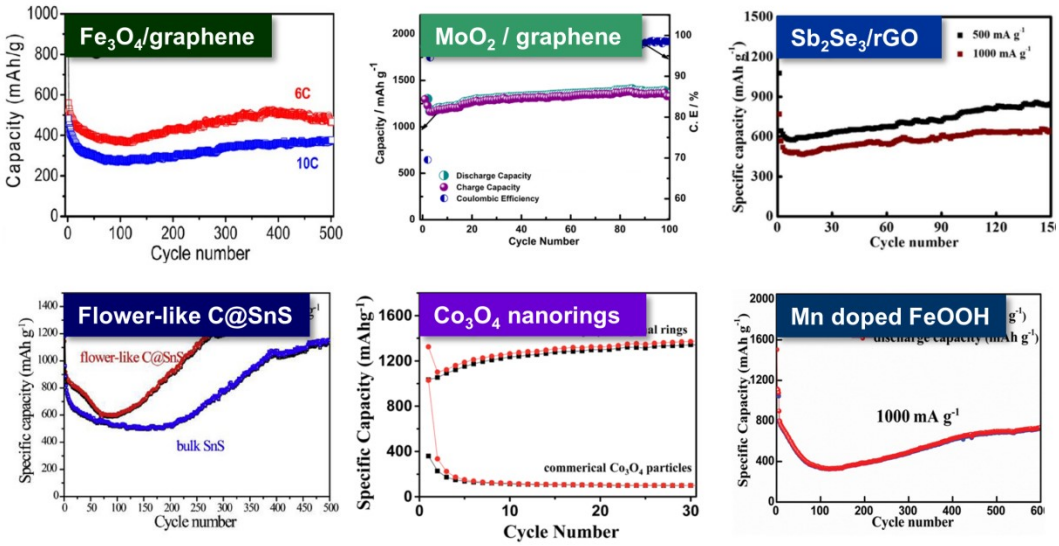

Figure 30. Negative fading in various types of anode materials. (Reproduced with permission from Ref. xx, copyright (xxxx) xxxxx. Ref. xx, copyright (xxxx) xxxxx. Ref. xx, copyright (xxxx) xxxxx. Ref. xx, copyright (xxxx) xxxxx. Ref. xx, copyright (xxxx) xxxxx. Ref. xx, copyright (xxxx) xxxxx.)

Electrode materials in LIBs are generally subjected to chemical and mechanical degradation that results in capacity fading during repeated cycling. Thorough understanding of the underlying mechanisms and means to alleviate this aging process has been an important target of research to predict the state of health of LIBs and extend their cycle life. To date, capacity fading is known to occur for a variety of reasons, such as Li plating, growth of SEI layer, transition metal dissolution, mechanical cracking and electrolyte depletion.[250,251] However, defying this convention, some electrode materials show an abnormal recovery in specific capacity as cycling progresses, as shown in **Figure 30** and **Table 1**.[31,252–256] In some cases, the capacity after repeated cycles even exceeds the reversible capacity in the first cycle. Sun et al. described the uncommon capacity increase phenomenon as lithiation-induced reactivation,[257] Huang et al. designated it as capacity recovery,[258] and most of other groups expressed it as simply capacity increasing.[43,44,54,55,68] In this paper, we named overall capacity increasing phenomenon as "negative fading". Various explanations have been suggested to

explain this phenomenon, yet it is still controversial. Based on previous reports, we can classify the proposed reasons for negative fading into three main categories: i) enhanced utilization of the conversion reaction, ii) optimization of electrolyte-derived surface layers, and iii) changes in morphology.

i) Enhanced utilization of the conversion reaction

As described in 3.4, the (de)lithiation mechanism of bulk and nanomaterials can be quite different. The dramatically increased charge transfer kinetics in nanomaterials enables new reactions that were not possible in bulk materials, and the expanded surface area enables inactive domains to participate in charge transfer.[228,259–262] Since the large particles undergo pulverization during repeated cycling in a conversion mechanism, their domain size can be reduced, leading to the creation of new electrochemically active sites, which, in turn, increases the specific capacity.

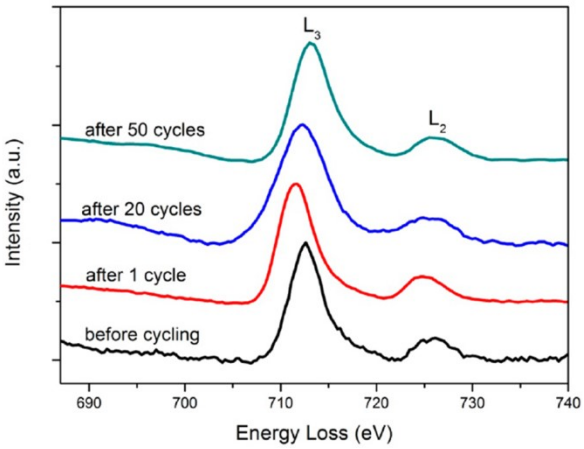

Sample	White line intensity ratio (L3/L2)	Oxidation state
before cycling	5	3
after 1 cycle	4.3	2
after 20 cycles	4.6	+2, +3
after 50 cycles	4.8	close to +3

Figure 31. EELS spectra of Fe-$L_{2,3}$ edges of pristine γ-Fe_2O_3@CNTs and cycled samples (upper) and white line intensity ratio (L_3/L_2) and corresponding average oxidation sate of Fe (lower). (Reproduced with permission from Ref. xx, copyright (xxxx) xxxxx)

Lv et al. clearly demonstrated the reactivation of Fe nanoparticles after cycling of maghemite (γ-Fe_2O_3) nanoparticles deposited on CNTs.[263] The reversible capacity of the γ-Fe_2O_3@CNT composite decreased during the initial few cycles from an incomplete conversion reaction ($Fe_2O_3 + 6Li^+ + 6e^- \leftrightarrow 2Fe + 3Li_2O$), seemingly due to the poor conductivity of Fe_2O_3. However, it gradually increased as the cycling continued. The origin of the unconventional cycle performance was unveiled by EELS. Based on the Fe-$L_{2,3}$ edge spectra in **Figure 31**, the oxidation states of Fe were calculated for pristine and charged electrodes after the 1st, 20th, 50th cycle, using both the ratio of L_3/L_2-edge white line intensity and the absolute energy position. Compared to the sample before cycling, the white line ratio (L_3/L_2) decreased from 5.0 to 4.3 after the first cycle, representing a decrease in oxidation state of Fe from Fe^{3+} to Fe^{2+}. Then, the white line ratio gradually increased to 4.6 and 4.8 after the 20th and 50th cycle, which implies that the amount of Fe^{3+} gradually increased toward that of the initial Fe_2O_3 after 50th cycles. Thus, it was confirmed that the decrease of reversible capacity of this Fe_2O_3 anode material after the first cycle is related to inefficient utilization of the complete redox transition of Fe, and the negative fading can be described by the re-activation of Fe to the efficient reconstitution of Fe^{3+}.

In some cases, the reversible capacity upon cycling even surpasses the capacity at the initial step.[264–266] Chu et al. observed much enhanced utilization after repeated cycles in MnO@Mn_3O_4/N-doped porous carbon composites electrodes.[264] Using electrochemical analysis, they confirmed that the oxidation state of Mn was as high as 3+ or 4+ after repeated cycling, compared to ~2+ in the pristine state. As a result of the increase in oxidation state, higher capacity was produced after cycling. Jiang et al. found that the reversible capacity of Mn_3O_4@C composite electrodes increased during the first 100 cycles, coinciding with the onset of a new anodic process at 2.1 V which was not observed in the first cycle.[265] The new anodic peak indicates the oxidation of the Mn compound to a higher valence state. After 500th

cycles, it was observed to be activated to $Mn^{3.5+}$ through XPS. It is worth noting that it is not clear how this increase of cationic charge is compensated, and how the necessary anions are generated during cycling. These questions should be the object of further research.

As the capacity increases were linked to the extent of changes in electronic states compared to the initial state, it is also worthwhile to understand the accompanying changes in crystal and local structure. Um et al. systematically analyzed the negative fading of Fe-based materials, a series of Sn doped ferrite/rGO composites ($Fe_{3-x}Sn_xO_4$/rGO) where the Sn^{4+} is totally incorporated into the Fe_3O_4 (Fe^{2+}, Fe^{3+}) structure.[43] As shown in **Figure 32(a)**, the negative fading phenomenon in the initial 50 cycles was found to be proportional to the Sn content. This observation was explained by the larger volume expansion of Sn than Fe_3O_4, inducing morphological reorganization and thereby increasing the opportunities to generate new contacts between the reduced metal and Li_2O. For the latter 50 cycles, rapid capacity

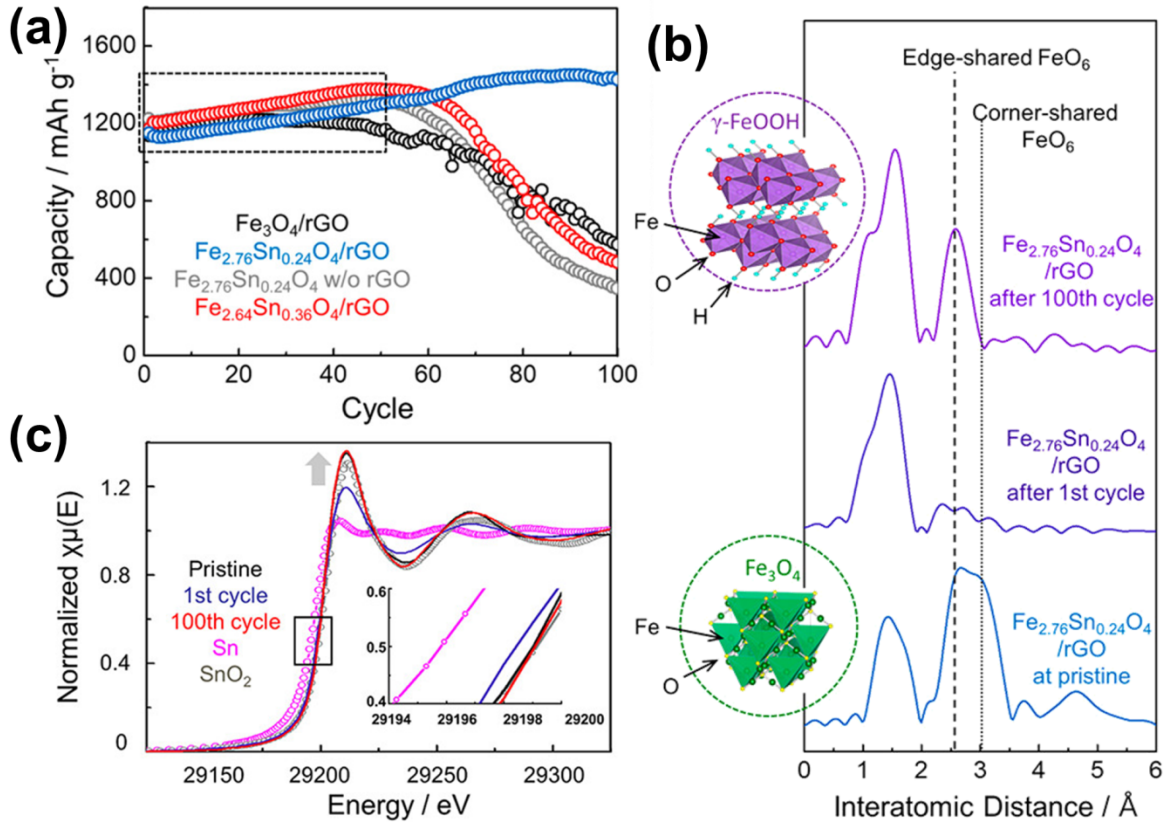

Figure 32. (a) Cycle performance of $Fe_{3-x}Sn_xO_4$/rGO composites and the $Fe_{2.76}Sn_{0.24}O_4$ composite without rGO. (b)Fourier transform magnitudes of Fe K-edge EXAFS spectra and (c) Sn K-edge XANES spectra of $Fe_{2.76}Sn_{0.24}O_4$/rGO composite in the pristine state and after the 1st and 100th4 cycled states (Reproduced with permission from Ref. xx, copyright (xxxx) xxxxx)

degradation occurred in $Fe_{2.64}Sn_{0.36}O_4$/rGO with the highest Sn content, implying both the destructive effect of pulverization from the high-capacity alloy and the beneficial effect of structural rearrangement by Sn substitution. Surprisingly, the observed oxidation state of Fe^{3+} after 100 cycles was higher than in the pristine state, $Fe^{2+, 3+}$. The structural insight into the Fe environment from EXAFS spectra in **Figure 31(b)** demonstrated that the initial magnetite phase in the $Fe_{2.76}Sn_{0.24}O_4$/rGO composite is transformed into γ-FeOOH upon extensive cycling. Simultaneously, the complete oxidation to SnO_2 after 100 cycles was confirmed by the Sn K-edge XANES spectra in **Figure 31(c)** although the oxidation state of Sn after the first cycle was lower than that. In addition, the authors suggested that formation and decomposition of the electrolyte-derived surface layer also contributed to some portion of increased capacity upon cycling. Thus, the negative fading phenomenon of Sn doped ferrite composite, $Fe_{2.76}Sn_{0.24}O_4$/rGO, can be explained by the complete utilization of conversion reaction of Sn into SnO_2 upon cycling along with the enhanced contribution of electrolyte-derived surface layer formation reaction. Overall, the electrochemical storage reaction after 100 cycles was described as γ-FeOOH + SnO_2 + (7+z)Li ↔ Fe + Li_zSn + LiOH + $3Li_2O$. Besides the recovered reversibility of conversion reaction of Sn into SnO_2 upon cycling, this work suggests a cycle-dependent mechanism in iron-based composites evolving from the conventionally expected formation of iron oxide in early cycles to a novel reaction involving iron oxyhydroxide upon extensive cycling, based on the reactivity of metal nanoparticles formed, during conversion, toward the SEI layer.

ii) Optimization of electrolyte-derived surface layers

The pulverization undergone by electrode materials during electrochemical cycling leads to an increase in specific surface area. Since the formation of the electrolyte-derived surface layer is enhanced by the catalytic contribution of metal nanoparticles formed upon a conversion reaction, as previously mentioned in 3.1, increasing the contact area between

electrolyte and active materials during cycling as a result of microstructural formatting could facilitate its growth, thus resulting in increased capacity.

Li et al. synthesized Fe_2O_3 with a 3D structure and investigated the cause of negative fading during the cycling.[141] The initial discharge and charge capacities were 1176.6 and 891.8 mAh g^{-1} at 0.2 C between 0.02–3.0 V, respectively. After the first cycle, the capacity gradually decreased up to the 10th cycle, and subsequently increased again. At the 100th cycle, a high capacity of 1105.6 mAh g^{-1} was delivered. In order to investigate the cause of this increase, the difference in capacities between the 10th and 100th cycle and the derivative of the electrochemical profiles versus voltage is provided in **Figure 33(a)**. It clearly shows that the negative fading resulted from enhancement in capacity at low potential, which they suggested was delivered from growth of the electrolyte-derived surface layer resulting from an increase in surface area as the electrode was pulverized into nanoparticles during cycling. EIS data collected at various voltages during the 2nd and 100th discharge, in **Figure 33(b) and (c)**, shows the evolution of a single broad semicircle into two semicircles. The second semicircle

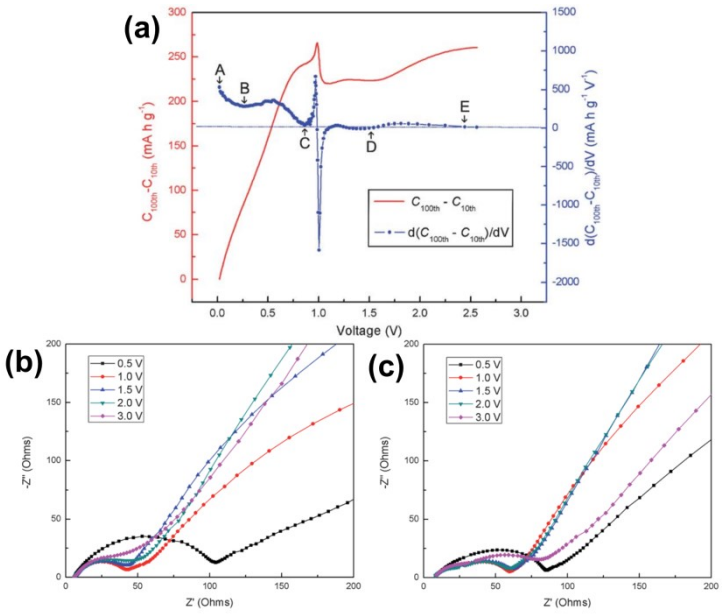

Figure 33. (a) Difference of capacity between the 10th and 100th cycle and their derivatives vs. potential. Nyquist plots of Fe_2O_3 electrode at various potential during (b) 2nd discharge and (c) 100th discharge. (Reproduced with permission from Ref. xx, copyright (xxxx) xxxxx)

is attributed to the growth of a surface layer, whose contribution to the total resistance is very low in the 2nd cycle, demonstrating the higher contribution of growth of surface layer in the 100th cycle. Considering all these observations, they concluded that only a small amount of activation of the bulk conversion reaction of Fe_2O_3 contributed to the capacity increment.

Similarly, Tang et al. observed a capacity increase in Fe_2O_3 nanoparticles after cycling and ascribed it to the growth of a surface layer using electroanalysis.[68] As displayed in **Figure 34(a)**, the specific capacity in same current density increased after 45 cycles. A derivative plot of the electrochemical profile at current density of 200 and 1000 mA g^{-1} in **Figure 34(b)** indicates that the extra capacity at low potential was substantially increased in both cases, suggesting higher contribution of electrolyte-derived surface layer formation reaction due to enlarged electrolyte contact area during cycling. Lastly, Li et al, showed growth of surface layer in Cu_2Se by observing changes in the EIS upon electrochemical cycling, which is correlated with the capacity increase in the anode.[267]

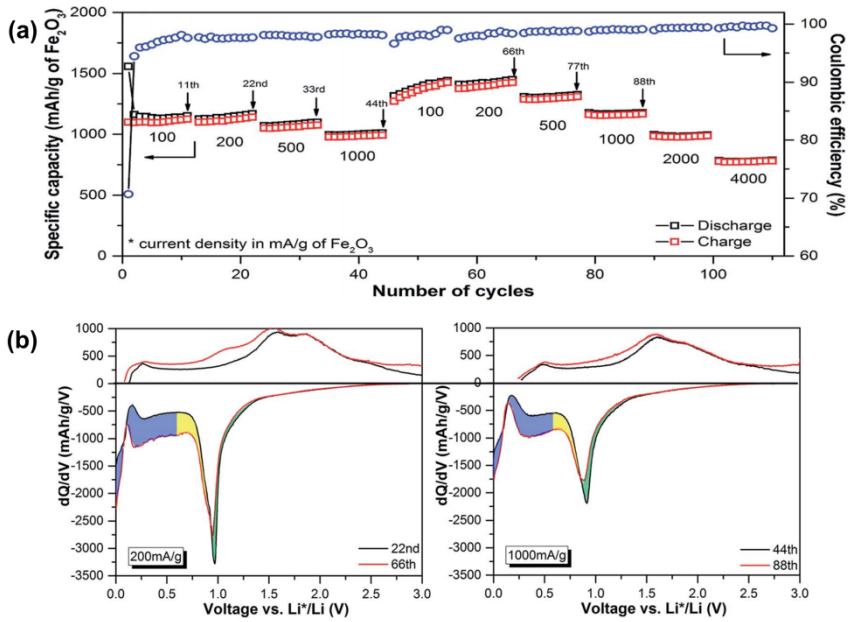

Figure 34. (a) Rate performance of γ-Fe_2O_3 nanoparticle electrodes. (b) dQ/dV plot of selected cycles at 200 and 1000 mA g^{-1}. (Reproduced with permission from Ref. xx, copyright (xxxx) xxxxx)

iii) **Changes in morphology**

When mechanical stress is applied due to rapid volume expansion during lithiation under

high current, internal gradients can result in fracture that changes porosity in the active materials and/or increases the surface area, both of which enhance reaction kinetics through transport, and, subsequently, the specific capacity. This morphology evolution during high rate cycling is referred to as a reactivation of the electrochemical reaction induced by high-rate lithiation, resulting in capacity increment.[257]

Sun et al. investigated the structural evolution of hollow mesoporous Co_3O_4 during high-rate cycling.[257] The reactivation followed the procedure as displayed in **Figure 35(a)**, and the corresponding changes in specific capacity are shown in **Figure 35(b)**. Initially, the reversible capacities decreased from ~827 mAh g^{-1} at the 2^{nd} cycle to ~246 mAh g^{-1} at the 90^{th} cycle. The scanning electron microscope (SEM) images of the electrode after 90 cycles shows the growth of surface layers with ~50 nm thickness as well as cracking and pore coalescing of hollow particles, which resulted in severe capacity degradation. During prolonged cycle, the capacity gradually increased and stabilized at ~927 mAh g^{-1} after 850 cycles. After 850 cycles, only a thin surface layer existed, and the pore size became bigger. The morphological evolution was proposed to be stemmed from the Kirkendall effect due to different diffusion rates in metallic Co and Li_2O. During lithiation, the formation of the Co/Li_2O nanocomposite involves a large volume expansion, and despite contraction during charge, the volume is still larger than in the initial spheres owing to slower diffusion kinetics in Li_2O phase. The enlarged particles generate free volume inside the materials and form larger pores and morphological re-organization, in this case, in the form of interconnected flower-like nanosheets, which could act as a robust structure to enhance kinetics, resulting in reactivation and, thus, negative fading.

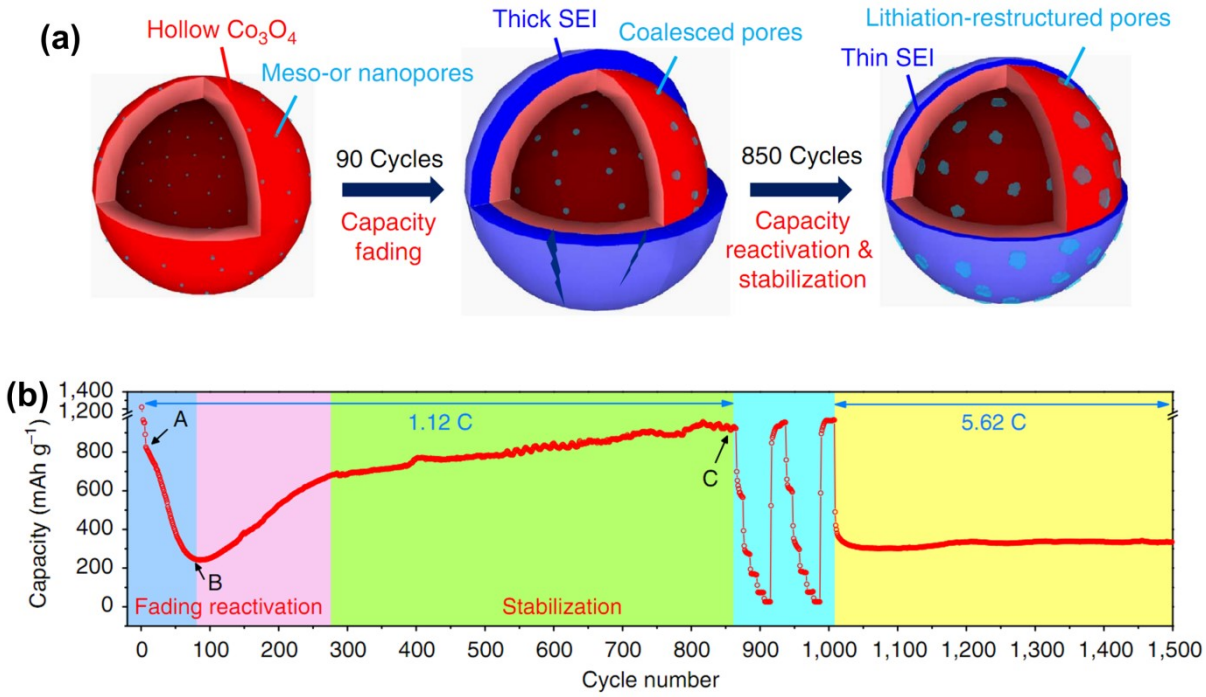

Figure 35. (a) Schematic diagram of evolution of mesoporous hollow spheres and surface layer formation upon long-term cycling. (b) Cycling performance showing reactivation induced by high-rate lithiation. (Reproduced with permission from Ref. xx, copyright (xxxx) xxxxx)

Similar morphological changes induced by lithiation at high rate were observed in double carbon layer-coated SnO_2 hollow spheres.[268] Under a high current density of 5 A g^{-1}, drastic capacity degradation occurs until initial 200 cycles, followed by notable recovery during further cycling. After 500 cycles, the initial hollow spheres split into hemispheres due to the high mechanical stress built during repeated volume changes and local gradients induced by high-rate cycling. The new hemispheres were proposed to expose the inner surface to the electrolyte, leading to enhanced performance. Zhang et al. suggested that the structural evolution in porous $Co_3V_2O_8$ nanosheets provides additional sites for interfacial reaction. As cycling proceeded, the nanosheets exfoliated into ultrathin layers with cracks and tiny pores, significantly enhancing the surface area.[269]

In the case of $FeMoO_4$ nanorods, changes in chemical composition induced an evolution of the morphology.[270] Testing of the cycling performance in **Figure 36(a)** shows that the initially high reversible capacities of ~1134 mAh g^{-1} decreased to ~451 mAh g^{-1} after 50

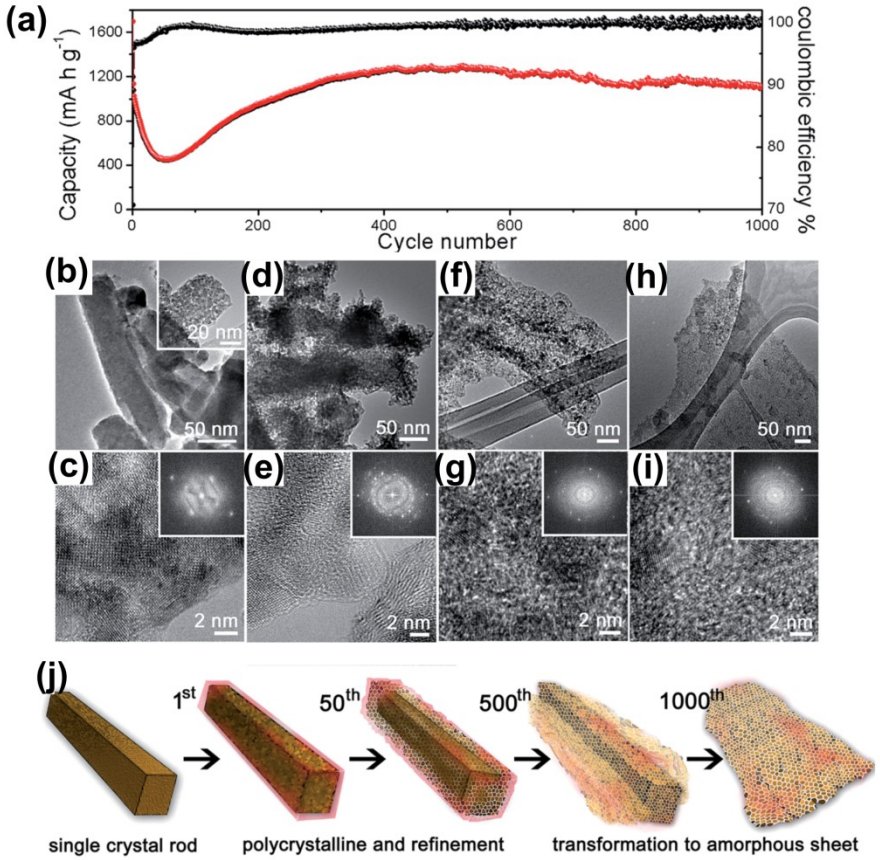

Figure 36. (a) Cycling performance of $FeMoO_4$ nanorod anode. HRTEM images of $FeMoO_4$ nanorod after (b),(c) 1st cycle, (d),(e) 50th cycle, (f),(g) 500th cycle, and (h),(i) 1000th cycle. (j) Schematic diagram of the morphology evolution of $FeMoO_4$ nanorods upon cycling. (Reproduced with permission from Ref. xx, copyright (xxxx) xxxxx)

cycles, and then increased gradually to reach ~1265 mAh g^{-1} at the 500th cycle, which is even higher than the initial value. The morphological changes in $FeMoO_4$ during cycling were investigated by HRTEM, in **Figure 36(b)–(i)**, and schematically described in **Figure 36(j)**. After the first cycle, the morphology did not change significantly but the crystallinity was reduced, with formation of discrete Fe_2O_3 and MoO_3 domains. Then, after 50 cycles, the surface was fragmented and a thick surface layer grew, explaining the capacity degradation. The portion of the porous and amorphous phase located at the surface became larger upon extensive cycling and the striking rearrangement led to a complete conversion from nanorod structures to porous nanosheets after 1000 cycles. The amorphous nanosheets contained domains of ~5 nm, providing more active sites and improved kinetic

properties, providing a pathway for the capacity increase.

4. STRATEGIES FOR EFFECTIVELY UTILIZING ABNORMAL CHARGE STORAGE

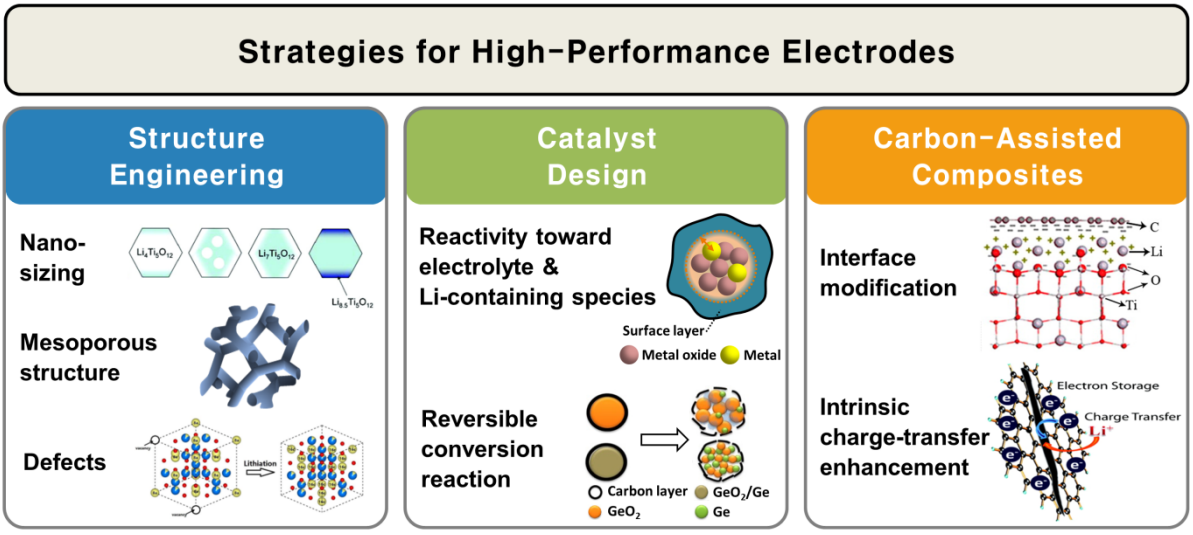

Figure 37. Proposed useful approaches to improve electrochemical performance of anode materials with high contribution of additional Li storage reaction. (Reproduced with permission from Ref. xx, copyright (xxxx) xxxxx)

Tapping into the additional mechanisms of charge storage discovered so far would be an effective way to increase the energy density of the corresponding batteries and to accelerate the advances toward next-generation devices, as well as to develop new electrode materials. To date, it is accepted that the morphological features and catalytic properties of the active materials play a crucial role in enabling unconventional extra charge storage, which could maximize the electrochemical performance. Additionally, the introduction of carbonaceous materials in electrode materials usually generates beneficial outcomes such as enhanced conductivity and additional interfacial charge storage. A series of strategies can be envisioned along these parameters, as summarized in **Figure 37**.

i. Structure engineering

Structural architectures having high specific surface area, developed porosity, and interconnected pore systems often exhibit additional charge storage as described in section

3.4. Thus, substantial efforts have been devoted to designing architectures with these unique attributes. In addition to the Li accommodation in defects, the structural engineering can also facilitate other abnormal Li storage mechanisms. The design features explored in the literature of this topic can be categorized as nanosizing,[159,238–240,260,271–277] introduction of mesoporosity,[57,95,159,265] and introduction of tailored defects.[160,278–281]

As nanoscience and nanotechnology develop, numerous researches have been conducted to fabricate electrode materials at the nanoscale in order to improve electrochemical performance.[62,67,68,282–285] Reducing the size of electrode materials to the nanoscale can not only deliver the electrical energy rapidly, but also redefine the theoretical limit of electrochemical storage. For TiO_2, the striking impact of particle size on Li solubility was described in 3.4.[238] In SnO_2, the theoretical reversible capacity was previously calculated to be 783 mAh g^{-1} based on the reversible alloying reaction between Sn and Li, and the conversion reaction of SnO_2 into Sn was considered as irreversible.[286–288] However, later studies have demonstrated that the oxidation of Sn with Li_2O is possible in SnO_2 anodes under certain conditions, leading to the partially reversible conversion to form SnO_x.[289,290] It was speculated that if the Sn particle size was controlled at 5 nm and the thickness of the diffusion layer between Sn metal and Li_2O was assumed to be 2 nm, a volume fraction as high as 99.2% could be re-oxidized during delithiation, possibly enabling the almost complete conversion back into SnO_2.[277] By unlocking previously considered as unfeasible reactions, the maximum theoretical capacities of TiO_2 and SnO_2 electrodes have been extended from 168 to 335 mAh g^{-1} and from 782 to 1494 mAh g^{-1}, respectively.

Nanosizing also affects other abnormal charge storage behaviors. As described in 3.5, reducing the size of electrode materials through pulverization induced electrochemical cycling could lead to negative fading from the enhanced contribution of reactions involving

the electrolyte-derived surface layer.[68,141,267] Cheng et al. observed that the higher capacity in nanosized NiO is originated from larger contribution of the reaction of electrolyte-derived surface layer as well as the redox reaction of NiO.[291] In addition, interfacial charge storage described in 3.2,[147,150] and reaction of LiOH at surface[27] and with Co clusters[92] in section 3.3 could be also correlated with the grain sizes. Accordingly, it seems that smaller sizes are advantageous in unconventional rechargeable Li chemistries. However, the capacity retention is also an important issue that should be addressed in nanosized electrode materials. After high Li accommodation in TiO_2, some of inserted Li is trapped in the crystal structure, leading to irreversible capacity loss.[292–294] In the SnO_2 film composed of 9.5 nm nanocrystals, although re-oxidation of Sn was reported up to 95.5% of coulombic efficiency, this desirable performance was limited to only the first cycle,[277] with the contribution of the additional reaction decreasing, and, thus, leading to capacity fading, due to the aggregation of particles during cycling.[295,296] Indeed, Huie et al. suggested that small particles tend to aggregate and form denser and tightly packed agglomerates, limiting the growth of electrolyte-derived surface layer as well as leading to higher polarization.[297] These observations lead to the conclusion that controlling the particle size is clearly a major factor for the initial Li uptake, but for stable capacity retention, it should be also integrated with additional designs such as morphology control and carbon coating.

In 1992, Kresge et al. first reported the synthesis of ordered mesoporous inorganic solids with regular arrays of uniform channels in dimensions of 1.6 to 10 nm, which has triggered tremendous research effort.[298] Especially in the field of energy conversion and storage, this mesoporous structure has attracted much attention due to the high resulting specific surface areas and the large portion of exposed active sites, which is known to be beneficial for electrochemical reactions. Ordered mesoporous RuO_2 delivered 1366 mAh g^{-1} during the first

cycle compared to 1060 mAh g^{-1} in the commercially available bulk RuO_2. The enhanced capacity was ascribed to the enhanced interfacial charge storage between nanosized Ru metal and Li_2O, owing to the mesoscopic structural effects such as high surface area, easy electron transport, and small particle domain.[57] In addition, mesoporous MoO_2 was reported to enable unconventional Li storage.[95] It was the first demonstration of two different mechanisms composed of intercalation and metallic Li storage being concurrent in a metal oxide. Therefore, it can be inferred that the mesoporous structure of metal oxide exhibits unexpected electrochemical charge storage beyond a simple conventional conversion reaction owing to the nanoscale pore engineering. For mesoporous SnO_2, a uniform pore structure not only relieves the severe volume changes during discharge and charge but also weakens the Sn-O bond strength, which facilitates a reversible conversion reaction in addition to the conventionally observed alloying reaction.[228] In short, engineered nanostructures with mesoporous networks could enable the realization of high-performance metal oxide anodes, by providing a source of additional Li accumulation.

The introduction of oxygen vacancies into metal oxides could be an effective way to modulate the intrinsic electrochemical properties of the metal oxides. The existence of oxygen vacancies effectively changes the electronic structure of the metal oxides and can reduce the energy requirement for electron transport and ion diffusion, which is beneficial to improve the electrochemical performances of the metal oxides.[160,280,281] For this reason, a large number of efforts have been devoted to the synthesis of electrode material with oxygen vacancies for enhanced electrochemical performance in LIBs.[232,278,281,299–303] In addition, amorphous structures could provide additional Li storage site by altering the energetic landscape of available sites, including new vacancies, in amorphous MoO_2, $FeMoO_4$ and V_2O_5 electrodes as mentioned in 3.4.[246,247] [270] In carbonaceous materials, reversible extra capacity can be also achieved by utilizing defects such as surface and pores, or by forming

Li-rich clusters.[6,7,211,216–223] Thus, it is reasonable to believe that structural defects can lead to the more Li storage, along with the superior rate capability from higher Li diffusivity.

ii. Catalyst design

In contrast to the traditional view that the surface film generated by electrolyte decomposition is quite inert during cell operation, the decomposition of electrolyte-derived surface layer was empirically observed in many researches and considered to be originated from the catalytic effects of metal nanoparticles. The metal nanoparticles formed upon electrochemical conversion reactions are exposed to, and, thus, can react with some components of the electrolyte-derived surface layer.[36,128] Consequently, intentionally embedding metal nanoparticles, which do not react with Li, in a carbon matrix significantly increases the reversible capacity from the additional contribution of electrolyte-derived surface layer formation.[126,304] In addition, the metal nanoparticle could facilitate the reaction of carbon in Li_2CO_3 formed after conversion reaction of metal carbonate compounds.[126,173,181] Here, the activity and reversibility of these reactions could be highly affected by the catalytic properties of each specific transition metal. In this aspect, one effective design to enhance catalytic activity in those reactions is to prepare atomically distributed binary metal compounds. With the complementary influences balancing the conductivity and stability between different kind of metals, the catalytic property of bimetallic nanoparticles could be improved compared to single transition metals, and exhibit better electrochemical performance, as empirically observed in the cases of $Mn_xCo_yCO_3$, $Co_xFe_yCO_3$, $Co_xNi_y(OH)_2$.[86,305–307]

The conversion reaction of SnO_2 is generally considered to be only partially reversible. To overcome the incomplete reversible conversion reaction in many other electrodes, various metal catalysts such as Co, Fe, Cu, Ni, and Ge are added to attain the complete re-oxidation of metal nanoparticles with decomposing Li_2O.[308–311] The addition of metal catalysts

correlates with a high and stable contribution of the reversible conversion reaction of SnO_2 and GeO_2, which were previously considered irreversible. As a relevant example discussed above, recovered capacity upon cycling involving the complete re-oxidation into SnO_2 was demonstrated in the Sn-doped ferrite ($Fe_{3-x}Sn_xO_4$) electrode.[43] Thus, compared to bare materials, the electrochemical performance of electrode materials with embedded metal catalysts, including cycle life, reversible capacity and coulombic efficiency, were significantly improved. The utilization of conversion reaction upon delithiation was also observed after repeated cycling in many iron and manganese oxides electrodes showing negative fading as introduced in 3.5.[263–266] Additionally, the research presents not only the recovered partial re-oxidation but also the phase transformation of conversion reaction-based host structure upon extended cycling, suggesting a variable working mechanism in the iron-based composite with the dynamic phases from iron oxide to iron oxyhydroxide in cycle life. These results constitute a notable body of knowledge that the catalytic effect of metal nanoparticles toward the surface layer could have dramatically beneficial effects in multiple ways upon repeated cycling.

iii. Carbon-assisted composites

The introduction of enormous amounts of Li in high-capacity anode materials inherently leads to large volume changes, causing pulverization of active materials, which, when uncontrolled, can lead to loss of electrical contact, eventually resulting in a poor capacity retention.[15,16] In addition to fabricating electrode materials at the nanoscale and deliberately introducing void spaces[312–316], substantial efforts have been devoted to addressing these volume changes by nanocompositing with carbonaceous materials, which enhance both structural stability and electrical conductivity.[249,317–319] The carbon-assisted design additionally provides new Li storage sites that improve the specific capacity of the

electrodes.[162,164,165,167] Aside from the benefit of carbonaceous materials that accommodate Li in pores and cavities, some authors posit that extra Li storage could also occur in the defects inherent to metal oxide/carbon composites,[320,321] such as storage via an electrostatic charge separation at both sides of the new interfaces where carbon serves as an electron acceptor. Based on first-principles calculations, interfacial oxygen atoms in TiO_2/C interfaces have an important contribution to charge storage, providing considerable additional capacity.[162] Similar effects have been proposed for Li_2S/C interfaces formed during cycling of MoS_2/C composites.[322–325] It is generally accepted that the design of composites of electrode materials with graphene (or rGO) can derive benefits from complementary features, such as preventing nanoparticle agglomeration and hindering restacking of separated graphene sheets by anchored nanoparticles, through the intimate bonds between graphene sheets and nanoparticles mediated by O,[326,327] which also facilitates rapid electron transport and enhanced ion diffusion.[249,326–330] Considering this possible additional charge storage behavior together with the stable and conductive matrices resulting from carbon-assisted composites, it is clear that this strategy should be very effective to realize high-performance electrode materials for next-generation batteries.

5. SUMMARY AND PERSPECTIVES

The explosion of methods of materials synthesis and assembly has led to a large diversity of designs of structure and chemistry of electrode materials for LIBs. Some of these highly tailored materials exhibit exceptionally high reversible capacity surpassing the theoretical value expected based on conventional Li storage mechanisms of insertion, alloying and conversion reactions. These unconventional observations call for a comprehensive and new perspective to understand such exceptional electrochemical charge storage behaviors. In this review, we have provided detailed insight into the origin of this additional storage capability including basic concepts, experimental evidences and some key issues remaining with our understanding of the proposed mechanisms. The most widely accepted explanation is the reversible formation/decomposition of electrolyte-derived surface layers. About half of the recent literature demonstrating extra capacity identified this mechanism as the origin of the behavior.[28] However, the information on the specific components that reversibly contribute to additional Li storage is still incomplete, even controversial. Since this reaction is highly affected by cell operating conditions such as the specific electrolyte, particle morphology and current densities, optimal conditions to fully leverage the novel reactivity are not yet apparent. Mechanisms of interfacial charge storage have also been considered as the reason for extra capacity. However, several reports suggest that this mechanism cannot account for the large capacities that are often measured. Lastly, there is emerging evidence that Li-containing species and structural defects, which were conventionally considered as electrochemically inactive, can accommodate Li in a manner distinct from the bulk of the material.

Another abnormal behavior associated with highly tailored nanomaterials is the increase in capacity upon cycling, termed here as negative fading. This behavior originates from changes in the electrode environment and architecture induced by the electrochemical reaction. Since

the negative fading is highly influenced by the electrode design and the catalytic activity of metals generated upon cycling, there is significant room to further exploit this capability through specially designed morphological features and optimization of catalytic activity by the metal. In this respect, the fabrication of composites with carbon has already demonstrated promise as an effective approach, as it can maximize electrolyte contact area and prohibit agglomeration of metal nanoparticles, which would reduce their catalytic power. Such strategy also brings about other potential enhancements driven by the fact that the carbonaceous materials can act as electron acceptor in a hypothetical interfacial charge storage mechanism and improve reaction kinetics.

These mechanisms open the door for a re-thinking of the rules of design of materials with high electrode performance, to generate vertical improvements. Based on the comprehensive understanding of abnormal Li storage behaviors and the new perspectives analyzed by this review, there are significant chances that the actual limits of the capacity beyond the theoretical values of bulk reactions will be probed and accomplished in the near future, through further breakthroughs in our ability to design materials in a way that strategically controls the associated electrochemical reactions. It is clear that the strategic utilization of anomalous charge storage can lead us to a solid pathway for fostering innovations in modern battery technologies.

AUTHOR INFORMATION

Corresponding authors

*E-mail: wsyoon@skku.edu.

Author contributions

Notes

The authors declare no competing financial interest.

Biographies

Hyunwoo Kim obtained his Bachelor's degree in chemical engineering from Sungkyunkwan University in 2016, and is currently a Ph. D. candidate in Department of Energy Science in same university under the supervision from Prof. Won-Sub Yoon. His work involves the synthesis of high-performance anode materials and investigation of the origins of the performance improvement.

Woosung Choi obtained his bachelor's degree in Advanced Material Science & Engineering from Sungkyunkwan university, Korea in 2015. He is currently working on his PhD at the Department of Energy Science in Sungkyunkwan university under the supervision of Prof. Won-Sub Yoon. His research interests focus on developing transition metal oxide and chalcogenide material for valuable energy-conversion and energy-storage application by handling Synchrotron based analytical technique including *in situ* XAS, XRD and SAXS.

Jaesang Yoon received his BS degree from Department of Chemical Engineering at Sungkyunkwan University, Korea in 2014. Presently, he is a Ph.D. candidate in Department of Energy Science at Sungkyunkwan University under the supervision of Prof. Won-Sub Yoon. His research interest focuses on the analysis of cathode and anode materials for lithium and sodium rechargeable batteries using X-ray based characterization techniques.

Ji Hyun Um graduated from Sungkyunkwan University in 2009 with B.S. in Chemical Engineering. She received M.S. in 2011 from School of Chemical and Biological Engineering at Seoul National University under the supervision of Prof. Ho-In Lee. Then, she received Ph.D. in 2015 at the same department of university under the supervision of Prof. Yung-Eun Sung. From 2015 to 2019, she joined Prof. Won-Sub Yoon's group as a postdoctoral researcher at Sungkyunkwan University with the research on electrode materials for lithium-ion battery and their electrochemistry. Her research interests focus on developing electrode materials for high energy-conversion and high energy-storage applications.

Wontae Lee received his B.S. degree from Department of Chemistry at Sungkyunkwan University in 2013. Presently, he is a Ph. D. candidate in Department of Energy Science at Sungkyunkwan Univerisity under the supervision of Prof. Won-Sub Yoon. His research interest focuses on reaction mechanism study in lithium and sodium rechargeable batteries by using X-ray based characterization techniques.

Jaeyeong Kim graduated from Sungkyunkwan University in 2017 with a Bachelor's of Chemical engineering. He is currently pursuing his Ph. D. in Department of Energy Science in Sungkyunkwan Univerisity under the guidance of Prof. Won-Sub Yoon. He studies the reaction mechanism of high-performance electrode materials for LIBs and solid state batteries.

Jordi Cabana is an Associate Professor at the Department of Chemistry of the University of Illinois at Chicago. Prior to his appointment at UIC, he was a Research Scientist at Lawrence Berkeley National Laboratory (USA), from 2008 until 2013. Prof. Cabana completed his Ph.D. in Materials Science at the Institut de Ciència de Materials de Barcelona (Spain) in 2004, followed by a postdoctoral appointment in the Department of Chemistry at Stony Brook University (USA). He is generally interested in the physical and inorganic chemistry of materials for electrochemical applications, with emphasis on redox and transport properties.

He was designated “Up-and-Coming” by Chemistry of Materials in 2017. He is currently a Scialog Fellow in Advanced Energy Storage, and he received a Scialog Award in 2018.

Won-Sub Yoon is a professor in Department of Energy Science at Sungkyunkwan University, Korea. He earned his Ph. D. in materials science and engineering from Yonsei University, Korea. He worked at Brookhaven National Laboratory as a principal investigator and Kookmin University as a faculty member. His research group is focused on electrode materials and the structural properties for energy conversion and storage systems including rechargeable batteries, fuel cells, and supercapacitors.

ACKNOWLEDGEMENT

This work was supported by a National Research Foundation of Korea (NRF) grant funded by the Korea government (MSIP) (2017R1A4A1015770). J.C. acknowledges the support of the National Science Foundation under Grant No. DMR-1809372.

ABBREVIATIONS USED

AFM	atomic force microscopy
AIMD	ab initio molecular dynamics
CNT	carbon nanotube
CV	cyclic voltammetry
DFT	density functional theory
EELS	electron energy loss spectroscopy
EIS	electrochemical impedance spectroscopy
EXAFS	extended X-ray absorption fine structure
FTIR	Fourier transform infrared spectroscopy
GITT	galvanostatic intermittent titration technique
HRTEM	high-resolution transmission electron microscopy
IR	infrared
IRRAS	infrared reflection absorption spectroscopy
LIB	lithium ion battery
MOF	metal organic framework
NMR	nuclear magnetic resonance
PDF	pair distribution function
PGF	polymeric/gel-like film
RDF	radial distribution function
rGO	reduced graphene oxide
SAED	selected area electron diffraction

SEI	solid electrolyte interphase
SEM	scanning electron microscope
SIMS	secondary ion mass spectrometry
Soft-XAS	soft X-ray absorption spectroscopy
TEM	transmission electron microscopy
TEY	total electron yield
TFY	total fluorescence yield
TG-MS	thermogravimetry and mass spectrometry
XANES	X-ray absorption near edge structure
XAS	X-ray absorption spectroscopy
XPS	X-ray photoelectron spectroscopy
XRD	X-ray diffraction

REFERENCES

(1) WHITTINGHAM, M. S. Electrical Energy Storage and Intercalation Chemistry. *Science (80-.).* **1976**, *192* (4244), 1126–1127.

(2) Yoshino, A.; Sanechika, K.; Nakajima., T. United States Patent. *Geothermics* **1987**, *14* (4), 595–599.

(3) Spahr, M. E.; Wilhelm, H.; Joho, F.; Panitz, J.-C.; Wambach, J.; Novák, P.; Dupont-Pavlovsky, N. Purely Hexagonal Graphite and the Influence of Surface Modifications on Its Electrochemical Lithium Insertion Properties. *J. Electrochem. Soc.* **2002**, *149* (8), A960.

(4) Momose, H.; Honbo, H.; Takeuchi, S.; Nishimura, K.; Horiba, T.; Muranaka, Y.; Kozono, Y.; Miyadera, H. X-Ray Photoelectron Spectroscopy Analyses of Lithium Intercalation and Alloying Reactions on Graphite Electrodes. *J. Power Sources* **1997**, *68* (2), 208–211.

(5) Nishimura, K.; Honbo, H.; Takeuchi, S.; Horiba, T.; Oda, M.; Koseki, M.; Muranaka, Y.; Kozono, Y.; Miyadera, H. Design and Performance of 10 Wh Rechargeable Lithium Batteries. *J. Power Sources* **1997**, *68* (2), 436–439.

(6) Liu, Y.; Xue, J. S.; Zheng, T.; Dahn, J. R. Mechanism of Lithium Insertion in Hard Carbons Prepared by Pyrolysis of Epoxy Resins. *Carbon N. Y.* **1996**, *34* (2), 193–200.

(7) Sato, K.; Noguchi, M.; Demachi, A.; Oki, N.; Endo, M. A Mechanism of Lithium Storage in Disordered Carbons. *Science (80-.).* **1994**, *264* (5158), 556–558.

(8) Qie, L.; Chen, W. M.; Wang, Z. H.; Shao, Q. G.; Li, X.; Yuan, L. X.; Hu, X. L.; Zhang, W. X.; Huang, Y. H. Nitrogen-Doped Porous Carbon Nanofiber Webs as Anodes for Lithium Ion Batteries with a Superhigh Capacity and Rate Capability. *Adv. Mater.* **2012**, *24* (15), 2047–2050.

(9) Poizot, P.; Laruelle, S.; Grugeon, S.; Dupont, L.; Tarascon, J. Nano-Sized Transition-Metal Oxides as Negative-Electrode Materials for Lithium-Ion Batteries. *Nature* **2000**, *407* (6803), 496–499.

(10) Wang, F.; Robert, R.; Chernova, N. A.; Pereira, N.; Omenya, F.; Badway, F.; Hua, X.; Ruotolo, M.; Zhang, R.; Wu, L.; et al. Conversion Reaction Mechanisms in Lithium Ion Batteries: Study of the Binary Metal Fluoride Electrodes. *J. Am. Chem. Soc.* **2011**, *133* (46), 18828–18836.

(11) Reddy, M. V.; Subba Rao, G. V.; Chowdari, B. V. R. Metal Oxides and Oxysalts as Anode Materials for Li Ion Batteries. *Chem. Rev.* **2013**, *113* (7), 5364–5457.

(12) Dey, A. N. Electrochemical Alloying of Lithium in Organic Electrolytes. *J. Electrochem. Soc.* **1971**, *118* (10), 1547.

(13) Wen, C. J.; Huggins, R. A. Chemical Diffusion in Intermediate Phases in the Lithium-Silicon System. *J. Solid State Chem.* **1981**, *37* (3), 271–278.

(14) Obrovac, M. N.; Chevrier, V. L. Alloy Negative Electrodes for Li-Ion Batteries. *Chem. Rev.* **2014**, *114* (23), 11444–11502.

(15) Su, Q.; Zhang, J.; Wu, Y.; Du, G. Revealing the Electrochemical Conversion Mechanism of Porous Co3O4 Nanoplates in Lithium Ion Battery by in Situ Transmission Electron Microscopy. *Nano Energy* **2014**, *9*, 264–272.

(16) Sun, Y.; Hu, X.; Luo, W.; Huang, Y. Ultrafine MoO 2 Nanoparticles Embedded in a Carbon Matrix as a High-Capacity and Long-Life Anode for Lithium-Ion Batteries. *J. Mater. Chem.* **2012**, *22* (2), 425–431.

(17) Lithiation, N. D.; Liu, X. H.; Zhong, L.; Huang, S.; Mao, S. X.; Zhu, T.; Huang, J. Y. Size-Dependent Fracture of Silicon. *ACS Nano* **2012**, No. 2, 1522–1531.

(18) Huang, J. Y.; Zhong, L.; Wang, C. M.; Sullivan, J. P.; Xu, W.; Zhang, L. Q.; Mao, S. X.; Hudak, N. S.; Liu, X. H.; Subramanian, A.; et al. In Situ Observation of the Electrochemical Lithiation of a Single SnO2 Nanowire Electrode. *Science (80-.).* **2010**, *330* (6010), 1515–1520.

(19) Wang, D.; Yu, Y.; He, H.; Wang, J.; Zhou, W.; Abruña, H. D. Template-Free Synthesis of Hollow-Structured Co 3 O 4 Nanoparticles as High-Performance Anodes for Lithium-Ion Batteries. *ACS Nano* **2015**, *9* (2), 1775–1781.

(20) Xu, S.; Hessel, C. M.; Ren, H.; Yu, R.; Jin, Q.; Yang, M.; Zhao, H.; Wang, D. α-Fe 2 O 3 Multi-Shelled Hollow Microspheres for Lithium Ion Battery Anodes with Superior Capacity and Charge Retention. *Energy Environ. Sci.* **2014**, *7* (2), 632–637.

(21) Park, G. O.; Yoon, J.; Park, S. Bin; Li, Z.; Choi, Y. S.; Yoon, W.-S.; Kim, H.; Kim, J. M. Nanostructural Uniformity of Ordered Mesoporous Materials: Governing Lithium Storage Behaviors. *Small* **2017**, *14* (43), 1702985.

(22) Jiang, Y.; Zhang, D.; Li, Y.; Yuan, T.; Bahlawane, N.; Liang, C.; Sun, W.; Lu, Y.; Yan, M. Amorphous Fe2O3 as a High-Capacity, High-Rate and Long-Life Anode Material for Lithium Ion Batteries. *Nano Energy* **2014**, *4*, 23–30.

(23) An, Y.; Fei, H.; Zeng, G.; Ci, L.; Xiong, S.; Feng, J.; Qian, Y. Green, Scalable, and Controllable Fabrication of Nanoporous Silicon from Commercial Alloy Precursors for High-Energy Lithium-Ion

Batteries. *ACS Nano* **2018**, *12* (5), 4993–5002.
(24) Hassoun, J.; Panero, S.; Simon, P.; Taberna, P. L.; Scrosati, B. High-Rate, Long-Life Ni–Sn Nanostructured Electrodes for Lithium-Ion Batteries. *Adv. Mater.* **2007**, *19* (12), 1632–1635.
(25) Chan, C. K.; Peng, H.; Liu, G.; McIlwrath, K.; Zhang, X. F.; Huggins, R. A.; Cui, Y. High-Performance Lithium Battery Anodes Using Silicon Nanowires. *Nat. Nanotechnol.* **2008**, *3* (1), 31–35.
(26) Cabana, J.; Monconduit, L.; Larcher, D.; Palacín, M. R. Beyond Intercalation-Based Li-Ion Batteries: The State of the Art and Challenges of Electrode Materials Reacting through Conversion Reactions. *Adv. Mater.* **2010**, *22* (35), 170–192.
(27) Hu, Y. Y.; Liu, Z.; Nam, K. W.; Borkiewicz, O. J.; Cheng, J.; Hua, X.; Dunstan, M. T.; Yu, X.; Wiaderek, K. M.; Du, L. S.; et al. Origin of Additional Capacities in Metal Oxide Lithium-Ion Battery Electrodes. *Nat. Mater.* **2013**, *12* (12), 1130–1136.
(28) Keppeler, M.; Srinivasan, M. Interfacial Phenomena/Capacities Beyond Conversion Reaction Occurring in Nano-Sized Transition-Metal-Oxide-Based Negative Electrodes in Lithium-Ion Batteries: A Review. *ChemElectroChem* **2017**, *4* (11), 2727–2754.
(29) Yu, S.-H.; Lee, S. H.; Lee, D. J.; Sung, Y.-E.; Hyeon, T. Conversion Reaction-Based Oxide Nanomaterials for Lithium Ion Battery Anodes. *Small* **2016**, *12* (16), 2146–2172.
(30) Luo, W.; Hu, X.; Sun, Y.; Huang, Y. Controlled Synthesis of Mesoporous MnO/C Networks by Microwave Irradiation and Their Enhanced Lithium-Storage Properties. *ACS Appl. Mater. Interfaces* **2013**, *5* (6), 1997–2003.
(31) Zhai, Y.; Ma, X.; Mao, H.; Shao, W.; Xu, L.; He, Y.; Qian, Y. Mn-Doped α-FeOOH Nanorods and α-Fe 2 O 3 Mesoporous Nanorods: Facile Synthesis and Applications as High Performance Anodes for LIBs. *Adv. Electron. Mater.* **2015**, *1* (6), 1400057.
(32) Dupont, L.; Laruelle, S.; Grugeon, S.; Dickinson, C.; Zhou, W.; Tarascon, J. M. Mesoporous Cr2O3 as Negative Electrode in Lithium Batteries: TEM Study of the Texture Effect on the Polymeric Layer Formation. *J. Power Sources* **2008**, *175* (1), 502–509.
(33) Xiao, Y.; Wang, X.; Wang, W.; Zhao, D.; Cao, M. Engineering Hybrid between MnO and N-Doped Carbon to Achieve Exceptionally High Capacity for Lithium-Ion Battery Anode. *ACS Appl. Mater. Interfaces* **2014**, *6* (3), 2051–2058.
(34) Chen, W. M.; Qie, L.; Shen, Y.; Sun, Y. M.; Yuan, L. X.; Hu, X. L.; Zhang, W. X.; Huang, Y. H. Superior Lithium Storage Performance in Nanoscaled MnO Promoted by N-Doped Carbon Webs. *Nano Energy* **2013**, *2* (3), 412–418.
(35) Sun, Y.; Hu, X.; Luo, W.; Xia, F.; Huang, Y. Reconstruction of Conformal Nanoscale MnO on Graphene as a High-Capacity and Long-Life Anode Material for Lithium Ion Batteries. *Adv. Funct. Mater.* **2013**, *23* (19), 2436–2444.
(36) Laruelle, S.; Grugeon, S.; Poizot, P.; Dollé, M.; Dupont, L.; Tarascon, J.-M. On the Origin of the Extra Electrochemical Capacity Displayed by MO/Li Cells at Low Potential. *J. Electrochem. Soc.* **2002**, *149* (5), A627.
(37) Article, R. In Situ Analyses for Ion Storage Materials. *Chem. Soc. Rev.* **2016**, 5717–5770.
(38) Bak, S.-M.; Shadike, Z.; Lin, R.; Yu, X.; Yang, X.-Q. In Situ/Operando Synchrotron-Based X-Ray Techniques for Lithium-Ion Battery Research. *NPG Asia Mater.* **2018**, *10* (7), 563–580.
(39) Zhu, H.; Huang, Y.; Zhu, H.; Wang, L.; Lan, S.; Xia, X.; Liu, Q. In Situ Probing Multiple-Scale Structures of Energy Materials for Li-Ion Batteries. *Small Methods* **2019**, *1900223*, 1900223.
(40) Hao, S.; Ouyang, B.; Li, C.; Zhang, B.; Feng, J.; Wu, J.; Srinivasan, M.; Huang, Y. Hollow Mesoporous Co(PO3)2@Carbon Polyhedra as High Performance Anode Materials for Lithium Ion Batteries. *J. Phys. Chem. C* **2019**, *123* (14), 8599–8606.
(41) Wang, Z.; Wang, Y.; Chen, Y.; Yousaf, M.; Wu, H.; Cao, A.; Han, R. P. S. Reticulate Dual-Nanowire Aerogel for Multifunctional Applications: A High-Performance Strain Sensor and a High Areal Capacity Rechargeable Anode. *Adv. Funct. Mater.* **2019**, *29* (11), 1–10.
(42) Yin, L.; Gao, Y. J.; Jeon, I.; Yang, H.; Kim, J. P.; Jeong, S. Y.; Cho, C. R. Rice-Panicle-like Γ-Fe 2 O 3 @C Nanofibers as High-Rate Anodes for Superior Lithium-Ion Batteries. *Chem. Eng. J.* **2019**, *356* (August 2018), 60–68.
(43) Um, J. H.; Palanisamy, K.; Jeong, M.; Kim, H.; Yoon, W. S. Phase Dynamics on Conversion-Reaction-Based Tin-Doped Ferrite Anode for Next-Generation Lithium Batteries. *ACS Nano* **2019**, *13* (5), 5674–5685.
(44) Wang, J.; Wang, H.; Li, F.; Xie, S.; Xu, G.; She, Y.; Leung, M. K. H.; Liu, T. Oxidizing Solid Co into Hollow Co 3 O 4 within Electrospun (Carbon) Nanofibers towards Enhanced Lithium Storage Performance. *J. Mater. Chem. A* **2019**, *7* (7), 3024–3030.
(45) Ruan, S.; Ma, C.; Wang, J.; Qiao, W.; Ling, L. Facile Synthesis of Graphene-Wrapped Porous MnCO3 Microspheres with Enhanced Surface Capacitive Effects for Superior Lithium Storage. *Chem. Eng. J.*

2019, *367* (December 2018), 64–75.
(46) Li, Y.; Huang, Y.; Zheng, Y.; Huang, R.; Yao, J. Facile and Efficient Synthesis of A-Fe 2 O 3 Nanocrystals by Glucose-Assisted Thermal Decomposition Method and Its Application in Lithium Ion Batteries. *J. Power Sources* **2019**, *416* (February), 62–71.
(47) Muhammad, S.; Yun, S.; Palanisamy, K.; Kim, H.; Yoon, W. S. Mechanistic Studies on Reversible Conversion Reaction in Li 2 MnO 3 -Carbon Nanotube Composite Anode. *J. Power Sources* **2019**, *423* (March), 323–330.
(48) Deng, J.; Yu, X.; Qin, X.; Li, B.; Kang, F. Carbon Sphere-Templated Synthesis of Porous Yolk-Shell ZnCo2O4 Spheres for High-Performance Lithium Storage. *J. Alloys Compd.* **2019**, *780*, 65–71.
(49) Ren, Q. Q.; Yu, F. Da; Zhang, S. W.; Yin, B. S.; Wang, Z. B.; Ke, K. Enhanced Electrochemical Performance by Size-Dependent SEI Layer Reactivation of NiCo 2 O 4 Anodes for Lithium Ion Batteries. *Electrochim. Acta* **2019**, *297*, 1011–1017.
(50) Kim, H.; Venugopal, N.; Yoon, J.; Yoon, W.-S. A Facile and Surfactant-Free Synthesis of Porous Hollow λ-MnO<inf>2</Inf> 3D Nanoarchitectures for Lithium Ion Batteries with Superior Performance. *J. Alloys Compd.* **2019**, *778*, 37–46.
(51) Wu, P.; Dong, X.; Gu, C.; Ge, S.; Su, Z.; Lu, Y.; Guo, C.; Shao, G.; Zhong, Y.; Liu, A. Designation of a Nano-Fe 3 O 4 Based Composite Electrode with Long Cycle Life for Lithium-Ion Batteries. *ChemElectroChem* **2019**, 3606–3614.
(52) Han, W.; Qin, X.; Wu, J.; Li, Q.; Liu, M.; Xia, Y.; Du, H.; Li, B.; Kang, F. Electrosprayed Porous Fe3O4/Carbon Microspheres as Anode Materials for High-Performance Lithium-Ion Batteries. *Nano Res.* **2018**, *11* (2), 892–904.
(53) Zhang, K.; Yang, H.; Lü, M.; Yan, C.; Wu, H.; Yuan, A.; Lin, S. Porous MoO2-Cu/C/Graphene Nano-Octahedrons Quadruple Nanocomposites as an Advanced Anode for Lithium Ion Batteries with Enhanced Rate Capability. *J. Alloys Compd.* **2018**, *731*, 646–654.
(54) Wang, Y.; Roller, J.; Maric, R. Novel Flame Synthesis of Nanostructured A-Fe2O3 Electrode as High-Performance Anode for Lithium Ion Batteries. *J. Power Sources* **2018**, *378* (December 2017), 511–515.
(55) He, Z.; Wang, K.; Zhu, S.; Huang, L. A.; Chen, M.; Guo, J.; Pei, S.; Shao, H.; Wang, J. MOF-Derived Hierarchical MnO-Doped Fe 3 O 4 @C Composite Nanospheres with Enhanced Lithium Storage. *ACS Appl. Mater. Interfaces* **2018**, *10* (13), 10974–10985.
(56) Wang, S.; Zhang, H.; Zhang, D.; Ma, Y.; Bi, X.; Yang, S. Vertically Oriented Growth of MoO3 Nanosheets on Graphene for Superior Lithium Storage. *J. Mater. Chem. A* **2018**, *6* (2), 672–679.
(57) Kim, Y.; Yoon, J.; Park, G. O.; Park, S. Bin; Kim, H.; Kim, J. M.; Yoon, W. S. Enhancement of the Interfacial Reaction on Mesoporous RuO 2 for next Generation Li Batteries. *J. Power Sources* **2018**, *396* (February), 749–753.
(58) Wang, X.; Zhang, M.; Zhao, J.; Huang, G.; Sun, H. Fe 3 O 4 @polyaniline Yolk-Shell Micro/Nanospheres as Bifunctional Materials for Lithium Storage and Electromagnetic Wave Absorption. *Appl. Surf. Sci.* **2018**, *427*, 1054–1063.
(59) Sun, D.; Tang, Y.; Ye, D.; Yan, J.; Zhou, H.; Wang, H. Tuning the Morphologies of MnO/C Hybrids by Space Constraint Assembly of Mn-MOFs for High Performance Li Ion Batteries. *ACS Appl. Mater. Interfaces* **2017**, *9* (6), 5254–5262.
(60) Su, L.; Hei, J.; Wu, X.; Wang, L.; Zhou, Z. Ultrathin Layered Hydroxide Cobalt Acetate Nanoplates Face-to-Face Anchored to Graphene Nanosheets for High-Efficiency Lithium Storage. *Adv. Funct. Mater.* **2017**, *27* (10).
(61) Guo, S. P.; Li, J. C.; Xiao, J. R.; Xue, H. G. Fe3S4 Nanoparticles Wrapped in an RGO Matrix for Promising Energy Storage: Outstanding Cyclic and Rate Performance. *ACS Appl. Mater. Interfaces* **2017**, *9* (43), 37694–37701.
(62) Islam, M.; Ali, G.; Jeong, M. G.; Choi, W.; Chung, K. Y.; Jung, H. G. Study on the Electrochemical Reaction Mechanism of NiFe2O4 as a High-Performance Anode for Li-Ion Batteries. *ACS Appl. Mater. Interfaces* **2017**, *9* (17), 14833–14843.
(63) Yoon, D.; Hwang, J.; Chang, W.; Kim, J. Uniform One-Pot Anchoring of Fe3O4 to Defective Reduced Graphene Oxide for Enhanced Lithium Storage. *Chem. Eng. J.* **2017**, *317*, 890–900.
(64) Yuan, T.; Jiang, Y.; Sun, W.; Xiang, B.; Li, Y.; Yan, M.; Xu, B.; Dou, S. Ever-Increasing Pseudocapacitance in RGO-MnO-RGO Sandwich Nanostructures for Ultrahigh-Rate Lithium Storage. *Adv. Funct. Mater.* **2016**, *26* (13), 2198–2206.
(65) Zhang, W.; Sheng, J.; Zhang, J.; He, T.; Hu, L.; Wang, R.; Mai, L.; Mu, S. Hierarchical Three-Dimensional MnO Nanorods/Carbon Anodes for Ultralong-Life Lithium-Ion Batteries. *J. Mater. Chem. A* **2016**, *4* (43), 16936–16945.
(66) Yan, C.; Chen, G.; Zhou, X.; Sun, J.; Lv, C. Template-Based Engineering of Carbon-Doped Co3O4 Hollow Nanofibers as Anode Materials for Lithium-Ion Batteries. *Adv. Funct. Mater.* **2016**, *26* (9),

1428–1436.
(67) Hao, S.; Zhang, B.; Ball, S.; Wu, J.; Srinivasan, M.; Huang, Y. Phase Transition of Hollow-Porous α-Fe 2 O 3 Microsphere Based Anodes for Lithium Ion Batteries during High Rate Cycling. *J. Mater. Chem. A* **2016**, *4*, 16569–16575.
(68) Tang, J.; Zavala Lugo, C. E.; Acuña Guzmán, S. F.; Daniel, G.; Kessler, V. G.; Seisenbaeva, G. A.; Pol, V. G. Pushing the Theoretical Capacity Limits of Iron Oxide Anodes: Capacity Rise of γ-Fe2O3nanoparticles in Lithium-Ion Batteries. *J. Mater. Chem. A* **2016**, *4* (46), 18107–18115.
(69) Binitha, G.; Ashish, A. G.; Ramasubramonian, D.; Manikandan, P.; Shaijumon, M. M. 3D Interconnected Networks of Graphene and Flower-Like Cobalt Oxide Microstructures with Improved Lithium Storage. *Adv. Mater. Interfaces* **2016**, *3* (1), 1–9.
(70) Wang, Z.; Chen, L.; Feng, J.; Liu, S.; Wang, Y.; Fan, Q.; Zhao, Y. In-Situ Grown SnO2 Nanospheres on Reduced GO Nanosheets as Advanced Anodes for Lithium-Ion Batteries. *ChemistryOpen* **2019**, *8* (6), 712–718.
(71) Zhao, Y.; Dong, W.; Riaz, M. S.; Ge, H.; Wang, X.; Liu, Z.; Huang, F. "electron-Sharing" Mechanism Promotes Co@Co 3 O 4 /CNTs Composite as the High-Capacity Anode Material of Lithium-Ion Battery. *ACS Appl. Mater. Interfaces* **2018**, *10* (50), 43641–43649.
(72) Ding, C.; Wang, L.; Zhou, W.; Wang, D.; Du, Y.; Wen, G. New Design on Li-Ion Battery Anode of Ternary Complex Metal/Metal Oxide@CNT: A Case Study of Hierarchical NiCo-NiCo2O4@CNTs. *Chem. Eng. J.* **2018**, *353* (May), 340–349.
(73) Sun, C.; Chen, S.; Li, Z. Controllable Synthesis of Fe 2 O 3 -Carbon Fiber Composites via a Facile Sol-Gel Route as Anode Materials for Lithium Ion Batteries. *Appl. Surf. Sci.* **2018**, *427*, 476–484.
(74) Zhang, J. P.; Wu, X. Y.; Wei, X.; Xu, S. M.; Ma, C.; Shu, M. H.; Wang, K. X.; Chen, J. S. Top-down Fabrication of Hierarchical Nanocubes on Nanosheets Composite for High-Rate Lithium Storage. *Dalt. Trans.* **2018**, *47* (45), 16155–16163.
(75) Cho, S. H.; Jung, J. W.; Kim, C.; Kim, I. D. Rational Design of 1-D Co3O4 Nanofibers@Low Content Graphene Composite Anode for High Performance Li-Ion Batteries. *Sci. Rep.* **2017**, *7* (November 2016), 1–9.
(76) Zhang, T.; Liang, H.; Xie, C.; Qiu, H.; Fang, Z.; Wang, L.; Yue, H.; Chen, G.; Wei, Y.; Wang, C.; et al. Morphology-Controllable Synthesis of Spinel Zinc Manganate with Highly Reversible Capability for Lithium Ion Battery. *Chem. Eng. J.* **2017**, *326*, 820–830.
(77) Li, Z.; Tang, B. Mn 3 O 4 /Nitrogen-Doped Porous Carbon Fiber Hybrids Involving Multiple Covalent Interactions and Open Voids as Flexible Anodes for Lithium-Ion Batteries. *Green Chem.* **2017**, *19* (24), 5862–5873.
(78) Wang, C.; Zhang, Y.; Li, Y.; Liu, J.; Wu, Q. H.; Jiang, J.; Li, Y. Y.; Lu, J. Synthesis of Fluorine-Doped α-Fe 2 O 3 Nanorods toward Enhanced Lithium Storage Capability. *Nanotechnology* **2017**, *28* (6), 065401.
(79) Yu, W. J.; Zhang, L.; Hou, P. X.; Li, F.; Liu, C.; Cheng, H. M. High Reversible Lithium Storage Capacity and Structural Changes of Fe 2 O 3 Nanoparticles Confined inside Carbon Nanotubes. *Adv. Energy Mater.* **2016**, *6* (3), 1–10.
(80) Sun, M.; Zhang, H.; Wang, Y. F.; Liu, W. L.; Ren, M. M.; Kong, F. G.; Wang, S. J.; Wang, X. Q.; Duan, X. L.; Ge, S. Z. Co/CoO@N-C Nanocomposites as High-Performance Anodes for Lithium-Ion Batteries. *J. Alloys Compd.* **2019**, *771*, 290–296.
(81) Zhao, Z.; Wang, Z.; Denis, D. K.; Sun, X.; Zhang, J.; Hou, L.; Zhang, X.; Yuan, C. Intrinsic Lithium Storage Mechanisms and Superior Electrochemical Behaviors of Monodispersed Hierarchical CoCO 3 Sub-Microspheroids as a Competitive Anode towards Li-Ion Batteries. *Electrochim. Acta* **2019**, *307*, 20–29.
(82) Liu, H.; Hu, Q. Novel Secondary Assembled Micro/Nano Porous Spheres ZnCo2O4 with Superior Electrochemical Performances as Lithium Ion Anode Material. *Nanotechnology* **2018**, *29* (32).
(83) Su, D.; Wang, J.; Yang, Z.; Liu, S.; Yang, J.; Yao, S.; Feng, X. Stability Electrochemical Performance of Self-Assembled Hierarchical MnCO 3 /MWCNT Nanocomposite as Anode Material for Lithium-Ion Batteries. *J. Solid State Electrochem.* **2018**, *22* (11), 3485–3491.
(84) Han, X.; Zhou, Y.; Liu, H. Porous MnCO3 Hierarchical Micro/Nano Cubes with Superior Lithium Storage Performances. *J. Mater. Sci. Mater. Electron.* **2018**, *29* (20), 17859–17864.
(85) Shi, S.; Zhang, M.; Liu, Y.; Hua, X.; Guo, H.; Yang, G. Efficient Construction of a CoCO3/Graphene Composite Anode Material for Lithium-Ion Batteries by Stirring Solvothermal Reaction. *Ceram. Int.* **2018**, *44* (4), 3718–3725.
(86) Li, J.; Xu, W.; Guo, C.; Li, M.; Zhang, L. Effect of Ni Content in Ni x Mn 1-x CO 3 (x = 0, 0.20, 0.25, 0.33) Submicrospheres on the Performances of Rechargeable Lithium Ion Batteries. *Electrochim. Acta* **2018**, *276*, 333–342.

(87) Zhou, J.; Cheng, S.; Jiang, Y.; Zheng, F.; Yang, L.; Rong, H.; Ou, X.; Wu, P.; Zhu, Y.; Liu, M. High Rate and High Capacity Lithiation of RGO-Coated Co2(OH)2CO3 Nanosheet Arrays for Lithium-Ion Batteries through the Involvement of CO32−. *Electrochim. Acta* **2017**, *235*, 98–106.
(88) Feng, X.; Shen, Q.; Shi, Y.; Zhang, J. Morphology-Controlled Hydrothermal Synthesis of Acanthosphere FeCO3 as an Excellent Performance Anode Material for Lithium Ion Batteries. *Ceram. Int.* **2016**, *42* (12), 14246–14251.
(89) Feng, X.; Shen, Q.; Shi, Y.; Zhang, J. One-Pot Hydrothermal Synthesis of Core-Shell Structured MnCO3@C as Anode Material for Lithium-Ion Batteries with Superior Electrochemical Performance. *Electrochim. Acta* **2016**, *220*, 391–397.
(90) Zhao, S.; Wang, Z.; He, Y.; Jiang, H.; Harn, Y. W.; Liu, X.; Su, C.; Jin, H.; Li, Y.; Wang, S.; et al. A Robust Route to Co 2 (OH) 2 CO 3 Ultrathin Nanosheets with Superior Lithium Storage Capability Templated by Aspartic Acid-Functionalized Graphene Oxide . *Adv. Energy Mater.* **2019**, *2*, 1901093.
(91) Chai, Y.; Wang, X.; Yu, Y.; Shi, X.; Zhang, Q.; Wang, N. Cooperation of Fe $_2$ O $_3$ @C and Co $_3$ O $_4$ /C Subunits Enhances the Cyclic Stability of Fe $_2$ O $_3$ @C/Co $_3$ O $_4$ Electrodes for Lithium-ion Batteries. *Int. J. Energy Res.* **2019**, No. April, er.4705.
(92) Kim, H.; Choi, W. I.; Jang, Y.; Balasubramanian, M.; Lee, W.; Park, G. O.; Park, S. Bin; Yoo, J.; Hong, J. S.; Choi, Y.-S.; et al. Exceptional Lithium Storage in a Co(OH) $_2$ Anode: Hydride Formation. *ACS Nano* **2018**, *12* (3), 2909–2921.
(93) Zhu, X.; Jiang, X.; Chen, X.; Liu, X.; Xiao, L.; Cao, Y. Fe2O3 Amorphous Nanoparticles/Graphene Composite as High-Performance Anode Materials for Lithium-Ion Batteries. *J. Alloys Compd.* **2017**, *711*, 15–21.
(94) Hao, S.; Zhang, B.; Feng, J.; Liu, Y.; Ball, S.; Pan, J.; Srinivasan, M.; Huang, Y. Nanoscale Ion Intermixing Induced Activation of Fe2O3/MnO2 Composites for Application in Lithium Ion Batteries. *J. Mater. Chem. A* **2017**, *5* (18), 8510–8518.
(95) Shon, J. K.; Lee, H. S.; Park, G. O.; Yoon, J.; Park, E.; Park, G. S.; Kong, S. S.; Jin, M.; Choi, J.-M.; Chang, H.; et al. Discovery of Abnormal Lithium-Storage Sites in Molybdenum Dioxide Electrodes. *Nat. Commun.* **2016**, *7* (1), 11049.
(96) Wang, L.; Zhang, Q.; Zhu, J.; Duan, X.; Xu, Z.; Liu, Y.; Yang, H.; Lu, B. Nature of Extra Capacity in MoS2 Electrodes: Molybdenum Atoms Accommodate with Lithium. *Energy Storage Mater.* **2019**, *16* (March 2018), 37–45.
(97) Edström, K.; Herstedt, M.; Abraham, D. P. A New Look at the Solid Electrolyte Interphase on Graphite Anodes in Li-Ion Batteries. *J. Power Sources* **2006**, *153* (2), 380–384.
(98) Bryngelsson, H.; Stjerndahl, M.; Gustafsson, T.; Edström, K. How Dynamic Is the SEI? *J. Power Sources* **2007**, *174* (2), 970–975.
(99) Yazami, R. Surface Chemistry and Lithium Storage Capability of the Graphite-Lithium Electrode. *Electrochim. Acta* **1999**, *45* (1), 87–97.
(100) Goodenough, J. B.; Park, K. S. The Li-Ion Rechargeable Battery: A Perspective. *J. Am. Chem. Soc.* **2013**, *135* (4), 1167–1176.
(101) Peled, E. The Electrochemical Behavior of Alkali and Alkaline Earth Metals in Nonaqueous Battery Systems—The Solid Electrolyte Interphase Model. *J. Electrochem. Soc.* **1979**, *126* (12), 2047.
(102) Verma, P.; Maire, P.; Novák, P. A Review of the Features and Analyses of the Solid Electrolyte Interphase in Li-Ion Batteries. *Electrochim. Acta* **2010**, *55* (22), 6332–6341.
(103) Fong, R. Studies of Lithium Intercalation into Carbons Using Nonaqueous Electrochemical Cells. *J. Electrochem. Soc.* **1990**, *137* (7), 2009.
(104) Aurbach, D. The Correlation Between the Surface Chemistry and the Performance of Li-Carbon Intercalation Anodes for Rechargeable 'Rocking-Chair' Type Batteries. *J. Electrochem. Soc.* **1994**, *141* (3), 603.
(105) Besenhard, J. O.; Winter, M.; Yang, J.; Biberacher, W. Filming Mechanism of Lithium-Carbon Anodes in Organic and Inorganic Electrolytes. *J. Power Sources* **1995**, *54* (2), 228–231.
(106) Zaghib, K.; Nadeau, G.; Kinoshita, K. Effect of Graphite Particle Size on Irreversible Capacity Loss. *J. Electrochem. Soc.* **2000**, *147* (6), 2110.
(107) Yazami, R.; Reynier, Y. F. Mechanism of Self-Discharge in Graphite-Lithium Anode. *Electrochim. Acta* **2002**, *47* (8), 1217–1223.
(108) Philippe, B.; Hahlin, M.; Edström, K.; Gustafsson, T.; Siegbahn, H.; Rensmo, H. Photoelectron Spectroscopy for Lithium Battery Interface Studies. *J. Electrochem. Soc.* **2016**, *163* (2), A178–A191.
(109) Aurbach, D. A Comparative Study of Synthetic Graphite and Li Electrodes in Electrolyte Solutions Based on Ethylene Carbonate-Dimethyl Carbonate Mixtures. *J. Electrochem. Soc.* **1996**, *143* (12), 3809.
(110) Aurbach, D.; Levi, M. D.; Levi, E.; Schechter, A. Failure and Stabilization Mechanisms of Graphite Electrodes. *J. Phys. Chem. B* **1997**, *101* (12), 2195–2206.

(111) Aurbach, D.; Zaban, A.; Gofer, Y.; Ely, Y. E.; Weissman, I.; Chusid, O.; Abramson, O. Recent Studies of the Lithium-Liquid Electrolyte Interface Electrochemical, Morphological and Spectral Studies of a Few Important Systems. *J. Power Sources* **1995**, *54* (1), 76–84.
(112) Andersson, A. M.; Henningson, A.; Siegbahn, H.; Jansson, U.; Edström, K. Electrochemically Lithiated Graphite Characterised by Photoelectron Spectroscopy. *J. Power Sources* **2003**, *119–121*, 522–527.
(113) Peled, E.; Bar Tow, D.; Merson, A.; Gladkich, A.; Burstein, L.; Golodnitsky, D. Composition, Depth Profiles and Lateral Distribution of Materials in the SEI Built on HOPG-TOF SIMS and XPS Studies. *J. Power Sources* **2001**, *97–98*, 52–57.
(114) Xu, K. Electrolytes and Interphases in Li-Ion Batteries and Beyond. *Chem. Rev.* **2014**, *114* (23), 11503–11618.
(115) Soto, F. A.; Ma, Y.; Martinez De La Hoz, J. M.; Seminario, J. M.; Balbuena, P. B. Formation and Growth Mechanisms of Solid-Electrolyte Interphase Layers in Rechargeable Batteries. *Chem. Mater.* **2015**, *27* (23), 7990–8000.
(116) Aurbach, D. Review of Selected Electrode-Solution Interactions Which Determine the Performance of Li and Li Ion Batteries. *J. Power Sources* **2000**, *89* (2), 206–218.
(117) An, S. J.; Li, J.; Daniel, C.; Mohanty, D.; Nagpure, S.; Wood, D. L. The State of Understanding of the Lithium-Ion-Battery Graphite Solid Electrolyte Interphase (SEI) and Its Relationship to Formation Cycling. *Carbon N. Y.* **2016**, *105*, 52–76.
(118) Poizot, P.; Laruelle, S.; Grugeon, S.; Dupont, L.; Tarascon, J. M. From the Vanadates to 3d-Metal Oxides Negative Electrodes. *Ionics (Kiel).* **2000**, *6* (5–6), 321–330.
(119) Grugeon, S.; Laruelle, S.; Herrera-Urbina, R.; Dupont, L.; Poizot, P.; Tarascon, J.-M. Particle Size Effects on the Electrochemical Performance of Copper Oxides toward Lithium. *J. Electrochem. Soc.* **2001**, *148* (4), A285.
(120) Wang, N.; Bai, Z.; Qian, Y.; Yang, J. Double-Walled Sb@TiO2-XNanotubes as a Superior High-Rate and Ultralong-Lifespan Anode Material for Na-Ion and Li-Ion Batteries. *Adv. Mater.* **2016**, *28* (21), 4126–4133.
(121) Barreca, D.; Cruz-Yusta, M.; Gasparotto, A.; Maccato, C.; Morales, J.; Pozza, A.; Sada, C.; Sánchez, L.; Tondello, E. Cobalt Oxide Nanomaterials by Vapor-Phase Synthesis for Fast and Reversible Lithium Storage. *J. Phys. Chem. C* **2010**, *114* (21), 10054–10060.
(122) Philippe, B.; Valvo, M.; Lindgren, F.; Rensmo, H.; Edström, K. Investigation of the Electrode/Electrolyte Interface of Fe2O3 Composite Electrodes: Li vs Na Batteries. *Chem. Mater.* **2014**, *26* (17), 5028–5041.
(123) Shaju, K. M.; Jiao, F.; Débart, A.; Bruce, P. G. Mesoporous and Nanowire Co3O4as Negative Electrodes for Rechargeable Lithium Batteries. *Phys. Chem. Chem. Phys.* **2007**, *9* (15), 1837–1842.
(124) Zhang, B.; Zhang, Y.; Miao, Z.; Wu, T.; Zhang, Z.; Yang, X. Micro/Nano-Structure Co3O4 as High Capacity Anode Materials for Lithium-Ion Batteries and the Effect of the Void Volume on Electrochemical Performance. *J. Power Sources* **2014**, *248*, 289–295.
(125) Long, H.; Shi, T.; Jiang, S.; Xi, S.; Chen, R.; Liu, S.; Liao, G.; Tang, Z. Synthesis of a Nanowire Self-Assembled Hierarchical ZnCo2O 4 Shell/Ni Current Collector Core as Binder-Free Anodes for High-Performance Li-Ion Batteries. *J. Mater. Chem. A* **2014**, *2* (11), 3741–3748.
(126) Su, L.; Zhong, Y.; Zhou, Z. Role of Transition Metal Nanoparticles in the Extra Lithium Storage Capacity of Transition Metal Oxides: A Case Study of Hierarchical Core-Shell Fe3O4@C and Fe@C Microspheres. *J. Mater. Chem. A* **2013**, *1* (47), 15158–15166.
(127) Débart, A.; Dupont, L.; Poizot, P.; Leriche, J.-B.; Tarascon, J. M. A Transmission Electron Microscopy Study of the Reactivity Mechanism of Tailor-Made CuO Particles toward Lithium. *J. Electrochem. Soc.* **2001**, *148* (11), A1266.
(128) Grugeon, S.; Laruelle, S.; Dupont, L.; Tarascon, J. M. An Update on the Reactivity of Nanoparticles Co-Based Compounds towards Li. *Solid State Sci.* **2003**, *5* (6), 895–904.
(129) Hu, J.; Li, H.; Huang, X.; Chen, L. Improve the Electrochemical Performances of Cr2O3 Anode for Lithium Ion Batteries. *Solid State Ionics* **2006**, *177* (26-32 SPEC. ISS.), 2791–2799.
(130) Zhong, K.; Xia, X.; Zhang, B.; Li, H.; Wang, Z.; Chen, L. MnO Powder as Anode Active Materials for Lithium Ion Batteries. *J. Power Sources* **2010**, *195* (10), 3300–3308.
(131) Zhang, J.; Wang, R.; Yang, X.; Lu, W.; Wu, X.; Wang, X.; Li, H.; Chen, L. Direct Observation of Inhomogeneous Solid Electrolyte Interphase on MnO Anode with Atomic Force Microscopy and Spectroscopy. *Nano Lett.* **2012**, *12* (4), 2153–2157.
(132) Martin, L.; Martinez, H.; Poinot, D.; Pecquenard, B.; Le Cras, F. Direct Observation of Important Morphology and Composition Changes at the Surface of the CuO Conversion Material in Lithium Batteries. *J. Power Sources* **2014**, *248*, 861–873.
(133) Tian, B.; Świątowska, J.; Maurice, V.; Zanna, S.; Seyeux, A.; Marcus, P. Binary Iron-Chromium Oxide

as Negative Electrode for Lithium-Ion Micro-Batteries - Spectroscopic and Microscopic Characterization. *Appl. Surf. Sci.* **2015**, *353*, 1170–1178.
(134) Tian, B.; Światowska, J.; Maurice, V.; Zanna, S.; Seyeux, A.; Klein, L. H.; Marcus, P. Aging-Induced Chemical and Morphological Modifications of Thin Film Iron Oxide Electrodes for Lithium-Ion Batteries. *Langmuir* **2014**, *30* (12), 3538–3547.
(135) Dedryvère, R.; Laruelle, S.; Grugeon, S.; Poizot, P.; Gonbeau, D.; Tarascon, J. M. Contribution of X-Ray Photoelectron Spectroscopy to the Study of the Electrochemical Reactivity of CoO toward Lithium. *Chem. Mater.* **2004**, *16* (6), 1056–1061.
(136) Li, J. T.; Maurice, V.; Swiatowska-Mrowiecka, J.; Seyeux, A.; Zanna, S.; Klein, L.; Sun, S. G.; Marcus, P. XPS, Time-of-Flight-SIMS and Polarization Modulation IRRAS Study of Cr2O3 Thin Film Materials as Anode for Lithium Ion Battery. *Electrochim. Acta* **2009**, *54* (14), 3700–3707.
(137) Tian, B.; Światowska, J.; Maurice, V.; Zanna, S.; Seyeux, A.; Klein, L. H.; Marcus, P. Combined Surface and Electrochemical Study of the Lithiation/Delithiation Mechanism of the Iron Oxide Thin-Film Anode for Lithium-Ion Batteries. *J. Phys. Chem. C* **2013**, *117* (42), 21651–21661.
(138) Rezvani, S. J.; Gunnella, R.; Witkowska, A.; Mueller, F.; Pasqualini, M.; Nobili, F.; Passerini, S.; Cicco, A. Di. Is the Solid Electrolyte Interphase an Extra-Charge Reservoir in Li-Ion Batteries? *ACS Appl. Mater. Interfaces* **2017**, *9* (5), 4570–4576.
(139) Rezvani, S. J.; Nobili, F.; Gunnella, R.; Ali, M.; Tossici, R.; Passerini, S.; Di Cicco, A. SEI Dynamics in Metal Oxide Conversion Electrodes of Li-Ion Batteries. *J. Phys. Chem. C* **2017**, *121* (47), 26379–26388.
(140) Wood, S. M.; Pham, C. H.; Heller, A.; Mullins, C. B. Formation of an Electroactive Polymer Gel Film upon Lithiation and Delithiation of PbSe. *J. Electrochem. Soc.* **2016**, *163* (8), A1666–A1671.
(141) Li, X.; Qiao, L.; Li, D.; Wang, X.; Xie, W.; He, D. Three-Dimensional Network Structured α-Fe<inf>2</Inf>O<inf>3</Inf> Made from a Stainless Steel Plate as a High-Performance Electrode for Lithium Ion Batteries. *J. Mater. Chem. A* **2013**, *1* (21), 6400–6406.
(142) Zeng, Y.; Li, L.; Li, H.; Huang, X.; Chen, L. TG-MS Analysis on Thermal Decomposable Components in the SEI Film on Cr2O3 Powder Anode in Li-Ion Batteries. *Ionics (Kiel).* **2009**, *15* (1), 91–96.
(143) Wu, X.; Guo, J.; McDonald, M. J.; Li, S.; Xu, B.; Yang, Y. Synthesis and Characterization of Urchin-like Mn0.33Co0.67C2O4 for Li-Ion Batteries: Role of SEI Layers for Enhanced Electrochemical Properties. *Electrochim. Acta* **2015**, *163*, 93–101.
(144) Gangaja, B.; Chandrasekharan, S.; Vadukumpully, S.; Nair, S. V.; Santhanagopalan, D. Surface Chemical Analysis of CuO Nanofiber Composite Electrodes at Different Stages of Lithiation/Delithiation. *J. Power Sources* **2017**, *340*, 356–364.
(145) Klein, F.; Pinedo, R.; Hering, P.; Polity, A.; Janek, J.; Adelhelm, P. Reaction Mechanism and Surface Film Formation of Conversion Materials for Lithium- and Sodium-Ion Batteries: An XPS Case Study on Sputtered Copper Oxide (CuO) Thin Film Model Electrodes. *J. Phys. Chem. C* **2016**, *120* (3), 1400–1414.
(146) Bock, D. C.; Waller, G. H.; Mansour, A. N.; Marschilok, A. C.; Takeuchi, K. J.; Takeuchi, E. S. Investigation of Solid Electrolyte Interphase Layer Formation and Electrochemical Reversibility of Magnetite, Fe3O4, Electrodes: A Combined X-Ray Absorption Spectroscopy and X-Ray Photoelectron Spectroscopy Study. *J. Phys. Chem. C* **2018**, *122* (26), 14257–14271.
(147) Balaya, P.; Li, H.; Kienle, L.; Maier, J. Fully Reversible Homogeneous and Heterogeneous Li Storage in RuO2with High Capacity. *Adv. Funct. Mater.* **2003**, *13* (8), 621–625.
(148) Li, H.; Richter, G.; Maier, J. Reversible Formation and Decomposition of LiF Clusters Using Transition Metal Fluorides as Precursors and Their Application in Rechargeable Li Batteries. *Adv. Mater.* **2003**, *15* (9), 736–739.
(149) Li, H.; Balaya, P.; Maier, J. Li-Storage via Heterogeneous Reaction in Selected Binary Metal Fluorides and Oxides. *J. Electrochem. Soc.* **2004**, *151* (11), A1878.
(150) Jamnik, J.; Maier, J. Nanocrystallinity Effects in Lithium Battery Materials. *Phys. Chem. Chem. Phys.* **2003**, *5* (23), 5215.
(151) Balaya, P.; Bhattacharyya, A. J.; Jamnik, J.; Zhukovskii, Y. F.; Kotomin, E. A.; Maier, J. Nano-Ionics in the Context of Lithium Batteries. *J. Power Sources* **2006**, *159* (1 SPEC. ISS.), 171–178.
(152) Zhukovskii, Y. F.; Balaya, P.; Kotomin, E. A.; Maier, J. Evidence for Interfacial-Storage Anomaly in Nanocomposites for Lithium Batteries from First-Principles Simulations. *Phys. Rev. Lett.* **2006**, *96* (5), 058302.
(153) Zhukovskii, Y. F.; Balaya, P.; Dolle, M.; Kotomin, E. A.; Maier, J. Enhanced Lithium Storage and Chemical Diffusion in Metal-LiF Nanocomposites: Experimental and Theoretical Results. *Phys. Rev. B - Condens. Matter Mater. Phys.* **2007**, *76* (23), 1–6.
(154) Hassan, A. S.; Navulla, A.; Meda, L.; Ramachandran, B. R.; Wick, C. D. Molecular Mechanisms for the Lithiation of Ruthenium Oxide Nanoplates as Lithium-Ion Battery Anode Materials: An Experimentally

Motivated Computational Study. *J. Phys. Chem. C* **2015**, *119* (18), 9705–9713.
(155) Bekaert, E.; Balaya, P.; Murugavel, S.; Maier, J.; Ménétrier, M. Li MAS NMR Investigation of Electrochemical Lithiation of RuO 2 : Evidence for an Interfacial Storage Mechanism. *Chem. Mater.* **2009**, *21* (5), 856–861.
(156) Yu, X. Q.; Sun, J. P.; Tang, K.; Li, H.; Huang, X. J.; Dupont, L.; Maier, J. Reversible Lithium Storage in LiF/Ti Nanocomposites. *Phys. Chem. Chem. Phys.* **2009**, *11* (41), 9497–9503.
(157) Guo, X.; Fang, X.; Mao, Y.; Wang, Z.; Wu, F.; Chen, L. Capacitive Energy Storage on Fe/Li 3 PO 4 Grain Boundaries. *J. Phys. Chem. C* **2011**, *115* (9), 3803–3808.
(158) Kim, Y.; Muhammad, S.; Kim, H.; Cho, Y.-H.; Kim, H.; Kim, J. M.; Yoon, W.-S. Probing the Additional Capacity and Reaction Mechanism of the RuO 2 Anode in Lithium Rechargeable Batteries. *ChemSusChem* **2015**, *8* (14), 2378–2384.
(159) Shin, J. Y.; Samuelis, D.; Maier, J. Sustained Lithium-Storage Performance of Hierarchical, Nanoporous Anatase TiO2 at High Rates: Emphasis on Interfacial Storage Phenomena. *Adv. Funct. Mater.* **2011**, *21* (18), 3464–3472.
(160) Balogun, M. S.; Zhu, Y.; Qiu, W.; Luo, Y.; Huang, Y.; Liang, C.; Lu, X.; Tong, Y. Chemically Lithiated TiO2 Heterostructured Nanosheet Anode with Excellent Rate Capability and Long Cycle Life for High-Performance Lithium-Ion Batteries. *ACS Appl. Mater. Interfaces* **2015**, *7* (46), 25991–26003.
(161) Li, X.; Lai, C.; Xiao, C. W.; Gao, X. P. Enhanced High Rate Capability of Dual-Phase Li4Ti5O12–TiO2 Induced by Pseudocapacitive Effect. *Electrochim. Acta* **2011**, *56* (25), 9152–9158.
(162) Liu, E.; Wang, J.; Shi, C.; Zhao, N.; He, C.; Li, J.; Jiang, J. Z. Anomalous Interfacial Lithium Storage in Graphene/TiO2 for Lithium Ion Batteries. *ACS Appl. Mater. Interfaces* **2014**, *6* (20), 18147–18151.
(163) Wu, Q.; Xu, J.; Yang, X.; Lu, F.; He, S.; Yang, J.; Fan, H. J.; Wu, M. Ultrathin Anatase TiO2 Nanosheets Embedded with TiO2-B Nanodomains for Lithium-Ion Storage: Capacity Enhancement by Phase Boundaries. *Adv. Energy Mater.* **2015**, *5* (7), 1–9.
(164) Chen, B.; Liu, E.; He, F.; Shi, C.; He, C.; Li, J.; Zhao, N. 2D Sandwich-like Carbon-Coated Ultrathin TiO2@defect-Rich MoS2 Hybrid Nanosheets: Synergistic-Effect-Promoted Electrochemical Performance for Lithium Ion Batteries. *Nano Energy* **2016**, *26*, 541–549.
(165) Wang, T.; Zhao, N.; Shi, C.; Ma, L.; He, F.; He, C.; Li, J.; Liu, E. Interface and Doping Effects on Li Ion Storage Behavior of Graphene/Li2O. *J. Phys. Chem. C* **2017**, *121* (36), 19559–19567.
(166) Jing, M.; Li, J.; Han, C.; Yao, S.; Zhang, J.; Zhai, H.; Chen, L.; Shen, X.; Xiao, K. Electrospinning Preparation of Oxygen-Deficient Nano TiO 2-x /Carbon Fibre Membrane as a Self-Standing High Performance Anode for Li-Ion Batteries. *R. Soc. Open Sci.* **2017**, *4* (7), 170323.
(167) Lv, Y.; Chen, B.; Zhao, N.; Shi, C.; He, C.; Li, J.; Liu, E. Interfacial Effect on the Electrochemical Properties of the Layered Graphene/Metal Sulfide Composites as Anode Materials for Li-Ion Batteries. *Surf. Sci.* **2016**, *651*, 10–15.
(168) Ponrouch, A.; Taberna, P. L.; Simon, P.; Palacín, M. R. On the Origin of the Extra Capacity at Low Potential in Materials for Li Batteries Reacting through Conversion Reaction. *Electrochim. Acta* **2012**, *61*, 13–18.
(169) Aragón, M. J.; Pérez-Vicente, C.; Tirado, J. L. Submicronic Particles of Manganese Carbonate Prepared in Reverse Micelles: A New Electrode Material for Lithium-Ion Batteries. *Electrochem. commun.* **2007**, *9* (7), 1744–1748.
(170) Aragón, M. J.; León, B.; Pérez Vicente, C.; Tirado, J. L. A New Form of Manganese Carbonate for the Negative Electrode of Lithium-Ion Batteries. *J. Power Sources* **2011**, *196* (5), 2863–2866.
(171) Aragón, M. J.; León, B.; Pérez Vicente, C.; Tirado, J. L. On the Use of Transition Metal Oxysalts as Conversion Electrodes in Lithium-Ion Batteries. *J. Power Sources* **2009**, *189* (1), 823–827.
(172) Mirhashemihaghighi, S.; Leoìn, B.; Pérez Vicente, C.; Tirado, J. L.; Stoyanova, R.; Yoncheva, M.; Zhecheva, E.; Sáez Puche, R.; Arroyo, E. M.; Romero De Paz, J. Lithium Storage Mechanisms and Effect of Partial Cobalt Substitution in Manganese Carbonate Electrodes. *Inorg. Chem.* **2012**, *51* (10), 5554–5560.
(173) Su, L.; Zhou, Z.; Qin, X.; Tang, Q.; Wu, D.; Shen, P. CoCO3 Submicrocube/Graphene Composites with High Lithium Storage Capability. *Nano Energy* **2013**, *2* (2), 276–282.
(174) Ding, Z.; Yao, B.; Feng, J.; Zhang, J. Enhanced Rate Performance and Cycling Stability of a CoCO 3 - Polypyrrole Composite for Lithium Ion Battery Anodes. *J. Mater. Chem. A* **2013**, *1* (37), 11200–11209.
(175) Zhang, C.; Cai, X.; Xu, D.; Chen, W.; Fang, Y.; Yu, X. Mn Doped FeCO 3 /Reduced Graphene Composite as Anode Material for High Performance Lithium-Ion Batteries. *Appl. Surf. Sci.* **2018**, *428*, 73–81.
(176) Lu, Z.; Wang, H.; Zhou, T.; Ma, C.; Yin, F.; Jiang, X.; Yang, G. CoCO3 Micrometer Particles Stabilized by Carbon Nanofibers Networks as Composite Electrode for Enhanced Rate and Cyclic Performance of Lithium-Ion Batteries. *Electrochim. Acta* **2018**, *270*, 22–29.

(177) Xu, D.; Liu, W.; Zhang, C.; Cai, X.; Chen, W.; Fang, Y.; Yu, X. Monodispersed FeCO 3 Nanorods Anchored on Reduced Graphene Oxide as Mesoporous Composite Anode for High-Performance Lithium-Ion Batteries. *J. Power Sources* **2017**, *364*, 359–366.
(178) Yin, J.; Ding, Z.; Lei, D.; Tang, L.; Deng, J.; Li, B.; He, Y. B. Zn-Substituted CoCO3embedded in Carbon Nanotubes Network as High Performance Anode for Lithium-Ion Batteries. *J. Alloys Compd.* **2017**, *712*, 605–612.
(179) Liu, X.; Yang, S.; Chen, X.; Zheng, H.; Guo, Z.; Feng, C. Synthesis and Electrochemical Properties of FeCO 3 with Different Morphology for Lithium-Ion Battery Application. *J. Alloys Compd.* **2017**, *698*, 87–93.
(180) Shao, L.; Ma, R.; Wu, K.; Shui, M.; Lao, M.; Wang, D.; Long, N.; Ren, Y.; Shu, J. Metal Carbonates as Anode Materials for Lithium Ion Batteries. *J. Alloys Compd.* **2013**, *581*, 602–609.
(181) Tian, N.; Hua, C.; Wang, Z.; Chen, L. Reversible Reduction of Li $_2$ CO $_3$. *J. Mater. Chem. A* **2015**, *3* (27), 14173–14177.
(182) Wang, L.; Tang, W.; Jing, Y.; Su, L.; Zhou, Z. Do Transition Metal Carbonates Have Greater Lithium Storage Capability than Oxides? A Case Study of Monodisperse CoCO3 and CoO Microspindles. *ACS Appl. Mater. Interfaces* **2014**, *6* (15), 12346–12352.
(183) Wu, S.; Lu, M.; Tian, X.; Jiang, C. A Facile Route to Graphene-Covered and Carbon-Encapsulated CoSO4 Nanoparticles as Anode Materials for Lithium-Ion Batteries. *Chem. Eng. J.* **2017**, *313*, 610–618.
(184) Shi, S.; Zhang, M.; Liu, Y.; Yang, G. Synthesis of Sandwich-like Co(CO3)0.5(OH)/Graphene Composite through Confined Growth and Self-Assemblies for Highly Reversible Lithium Storage. *J. Alloys Compd.* **2018**, *764*, 709–717.
(185) Zhou, X.; Zhong, Y.; Yang, M.; Zhang, Q.; Wei, J.; Zhou, Z. Co2(OH)2CO3 Nanosheets and CoO Nanonets with Tailored Pore Sizes as Anodes for Lithium Ion Batteries. *ACS Appl. Mater. Interfaces* **2015**, *7* (22), 12022–12029.
(186) Zhao, S.; Wang, Z.; He, Y.; Jiang, B.; Harn, Y.; Liu, X.; Yu, F.; Feng, F.; Shen, Q.; Lin, Z. Interconnected Ni(HCO3)2 Hollow Spheres Enabled by Self-Sacrificial Templating with Enhanced Lithium Storage Properties. *ACS Energy Lett.* **2017**, *2* (1), 111–116.
(187) Kong, F.; He, X.; Chen, J.; Tao, S.; Qian, B.; Jiang, X.; Luo, H. Hierarchical Ni(HCO3)2 Nanosheets Anchored on Carbon Nanofibers as Binder-Free Anodes for Lithium-Ion Batteries. *Energy Technol.* **2019**, *7* (6), 1–7.
(188) Dong, Y.; Ma, Y.; Li, D.; Liu, Y.; Chen, W.; Feng, X.; Zhang, J. Construction of 3D Architectures with Ni(HCO3)2 Nanocubes Wrapped by Reduced Graphene Oxide for LIBs: Ultrahigh Capacity, Ultrafast Rate Capability and Ultralong Cycle Stability. *Chem. Sci.* **2018**, *9* (46), 8682–8691.
(189) Maiti, S.; Pramanik, A.; Manju, U.; Mahanty, S. Reversible Lithium Storage in Manganese 1,3,5-Benzenetricarboxylate Metal-Organic Framework with High Capacity and Rate Performance. *ACS Appl. Mater. Interfaces* **2015**, *7* (30), 16357–16363.
(190) Xie, J.; Zhang, Q. Recent Progress in Rechargeable Lithium Batteries with Organic Materials as Promising Electrodes. *J. Mater. Chem. A* **2016**, *4* (19), 7091–7106.
(191) Li, C.; Lou, X.; Shen, M.; Hu, X.; Guo, Z.; Wang, Y.; Hu, B.; Chen, Q. High Anodic Performance of Co 1,3,5-Benzenetricarboxylate Coordination Polymers for Li-Ion Battery. *ACS Appl. Mater. Interfaces* **2016**, *8* (24), 15352–15360.
(192) Li, G.; Yang, H.; Li, F.; Cheng, F.; Shi, W.; Chen, J.; Cheng, P. A Coordination Chemistry Approach for Lithium-Ion Batteries: The Coexistence of Metal and Ligand Redox Activities in a One-Dimensional Metal-Organic Material. *Inorg. Chem.* **2016**, *55* (10), 4935–4940.
(193) Lee, H. H.; Lee, J. Bin; Park, Y.; Park, K. H.; Okyay, M. S.; Shin, D. S.; Kim, S.; Park, J.; Park, N.; An, B. K.; et al. Coordination Polymers for High-Capacity Li-Ion Batteries: Metal-Dependent Solid-State Reversibility. *ACS Appl. Mater. Interfaces* **2018**, *10* (26), 22110–22118.
(194) Saravanan, K.; Nagarathinam, M.; Balaya, P.; Vittal, J. J. Lithium Storage in a Metal Organic Framework with Diamondoid Topology-A Case Study on Metal Formates. *J. Mater. Chem.* **2010**, *20* (38), 8329–8335.
(195) Lee, H. H.; Park, Y.; Kim, S. H.; Yeon, S. H.; Kwak, S. K.; Lee, K. T.; Hong, S. Y. Mechanistic Studies of Transition Metal-Terephthalate Coordination Complexes upon Electrochemical Lithiation and Delithiation. *Adv. Funct. Mater.* **2015**, *25* (30), 4859–4866.
(196) He, S.; Zhou, X.; Li, Z.; Wang, J.; Ma, L.; Yang, S. Fluorine Doping Strengthens the Lithium-Storage Properties of the Mn-Based Metal-Organic Framework. *ACS Appl. Mater. Interfaces* **2017**, *9* (32), 26907–26914.
(197) Lee, H. H.; Nam, D.; Kim, C. K.; Kim, K.; Lee, Y.; Ahn, Y. J.; Lee, J. Bin; Kwak, J. H.; Choe, W.; Choi, N. S.; et al. Molecular Engineered Safer Organic Battery through the Incorporation of Flame Retarding Organophosphonate Moiety. *ACS Appl. Mater. Interfaces* **2018**, *10* (12), 10096–10101.

(198) Jiang, H.; Zhao, S.; Ma, X.; Liu, S.; Shen, Q. A Fast π-π Stacking Self-Assembly of Cobalt Terephthalate Dihydrate and the Twelve-Electron Lithiation-Delithiation of Anhydrous Cobalt Terephthalate. *J. Power Sources* **2019**, *426* (December 2018), 23–32.
(199) Kim, S. H.; Lee, H. H.; Kim, J. M.; Hong, S. Y.; Lee, S. Y. Heteromat-Framed Metal-Organic Coordination Polymer Anodes for High-Performance Lithium-Ion Batteries. *Energy Storage Mater.* **2019**, *19* (December 2018), 130–136.
(200) Lin, Y.; Zhang, Q.; Zhao, C.; Li, H.; Kong, C.; Shen, C.; Chen, L. An Exceptionally Stable Functionalized Metal-Organic Framework for Lithium Storage. *Chem. Commun.* **2015**, *51* (4), 697–699.
(201) Liu, Q.; Yu, L.; Wang, Y.; Ji, Y.; Horvat, J.; Cheng, M. L.; Jia, X.; Wang, G. Manganese-Based Layered Coordination Polymer: Synthesis, Structural Characterization, Magnetic Property, and Electrochemical Performance in Lithium-Ion Batteries. *Inorg. Chem.* **2013**, *52* (6), 2817–2822.
(202) Aragón, M. J.; León, B.; Vicente, C. P.; Tirado, J. L.; Chadwick, A. V.; Berko, A.; Beh, S. Y. Cobalt Oxalate Nanoribbons as Negative-Electrode Material for Lithium-Ion Batteries. *Chem. Mater.* **2009**, *21* (9), 1834–1840.
(203) Armand, M.; Grugeon, S.; Vezin, H.; Laruelle, S.; Ribière, P.; Poizot, P.; Tarascon, J. M. Conjugated Dicarboxylate Anodes for Li-Ion Batteries. *Nat. Mater.* **2009**, *8* (2), 120–125.
(204) Han, X.; Chang, C.; Yuan, L.; Sun, T.; Sun, J. Aromatic Carbonyl Derivative Polymers as High-Performance Li-Ion Storage Materials. *Adv. Mater.* **2007**, *19* (12), 1616–1621.
(205) Han, X.; Qing, G.; Sun, J.; Sun, T. How Many Lithium Ions Can Be Inserted onto Fused C 6 Aromatic Ring Systems? *Angew. Chemie - Int. Ed.* **2012**, *51* (21), 5147–5151.
(206) Wang, S.; Wang, L.; Zhang, K.; Zhu, Z.; Tao, Z.; Chen, J. Organic Li 4 C 8 H 2 O 6 Nanosheets for Lithium-Ion Batteries. *Nano Lett.* **2013**, *13* (9), 4404–4409.
(207) Walker, W.; Grugeon, S.; Vezin, H.; Laruelle, S.; Armand, M.; Wudl, F.; Tarascon, J. M. Electrochemical Characterization of Lithium 4,4′-Tolane-Dicarboxylate for Use as a Negative Electrode in Li-Ion Batteries. *J. Mater. Chem.* **2011**, *21* (5), 1615–1620.
(208) Tatsumi, K.; Kawamura, T.; Higuchi, S.; Hosotubo, T.; Nakajima, H.; Sawada, Y. Anode Characteristics of Non-Graphitizable Carbon Fibers for Rechargeable Lithium-Ion Batteries. *J. Power Sources* **1997**, *68* (2), 263–266.
(209) Yata, S.; Kinoshita, H.; Komori, M.; Ando, N.; Kashiwamura, T.; Harada, T.; Tanaka, K.; Yamabe, T. Structure and Properties of Deeply Li-Doped Polyacenic Semiconductor Materials beyond C6Li Stage. *Synth. Met.* **1994**, *62* (2), 153–158.
(210) Hara, M.; Satoh, A.; Takami, N.; Ohsaki, T. Structural and Electrochemical Properties of Lithiated Polymerized Aromatics. Anodes for Lithium-Ion Cells. *J. Phys. Chem.* **1995**, *99* (44), 16338–16343.
(211) Mabuchi, A. Charge-Discharge Characteristics of the Mesocarbon Miocrobeads Heat-Treated at Different Temperatures. *J. Electrochem. Soc.* **1995**, *142* (4), 1041.
(212) Zheng, T. Lithium Insertion in High Capacity Carbonaceous Materials. *J. Electrochem. Soc.* **1995**, *142* (8), 2581.
(213) Tatsumi, K. [Sup 7]Li-Nuclear Magnetic Resonance Observation of Lithium Insertion into Mesocarbon Microbeads. *J. Electrochem. Soc.* **1996**, *143* (6), 1923.
(214) Zheng, T. High-Capacity Carbons Prepared from Phenolic Resin for Anodes of Lithium-Ion Batteries. *J. Electrochem. Soc.* **1995**, *142* (11), L211.
(215) Xue, J. S. Dramatic Effect of Oxidation on Lithium Insertion in Carbons Made from Epoxy Resins. *J. Electrochem. Soc.* **1995**, *142* (11), 3668.
(216) J.R. Dahn; Tao Zheng; Yinghu Liu; J.S. Xue. Mechanisms for Lithium Insertion in Carbonaceous Materials. *Science (80-.).* **1995**, *270* (October), 590.
(217) Wang, S.; Matsumura, Y.; Maeda, T. A Model of the Interactions between Disordered Carbon and Lithium. *Synth. Met.* **1995**, *71* (1–3), 1759–1760.
(218) Peled, E. Improved Graphite Anode for Lithium-Ion Batteries Chemically. *J. Electrochem. Soc.* **1996**, *143* (1), L4.
(219) Menachem, C.; Peled, E.; Burstein, L.; Rosenberg, Y. Characterization of Modified NG7 Graphite as an Improved Anode for Lithium-Ion Batteries. *J. Power Sources* **1997**, *68* (2), 277–282.
(220) Zheng, T.; Xue, J. S.; Dahn, J. R. Lithium Insertion in Hydrogen-Containing Carbonaceous Materials. *Chem. Mater.* **1996**, *8* (2), 389–393.
(221) Dahn, J. R.; Xing, W.; Gao, Y. The "Falling Cards Model" for the Structure of Microporous Carbons. *Carbon N. Y.* **1997**, *35* (6), 825–830.
(222) Tokumitsu, K.; Fujimoto, H.; Mabuchi, A.; Kasuh, T. High Capacity Carbon Anode for Li-Ion Battery. *Carbon N. Y.* **1999**, *37* (10), 1599–1605.
(223) Yazami, R.; Deschamps, M. High Reversible Capacity Carbon-Lithium Negative Electrode in Polymer Electrolyte. *J. Power Sources* **1995**, *54* (2), 411–415.

(224) Pollak, E.; Geng, B.; Jeon, K. J.; Lucas, I. T.; Richardson, T. J.; Wang, F.; Kostecki, R. The Interaction of Li + with Single-Layer and Few-Layer Graphene. *Nano Lett.* **2010**, *10* (9), 3386–3388.
(225) Lee, E.; Persson, K. A. Li Absorption and Intercalation in Single Layer Graphene and Few Layer Graphene by First Principles. *Nano Lett.* **2012**, *12* (9), 4624–4628.
(226) Xing, W. Study of Irreversible Capacities for Li Insertion in Hard and Graphitic Carbons. *J. Electrochem. Soc.* **1997**, *144* (4), 1195.
(227) Lee, S.-H.; Kim, Y.-H.; Deshpande, R.; Parilla, P. A.; Whitney, E.; Gillaspie, D. T.; Jones, K. M.; Mahan, A. H.; Zhang, S.; Dillon, A. C. Reversible Lithium-Ion Insertion in Molybdenum Oxide Nanoparticles. *Adv. Mater.* **2008**, *20* (19), 3627–3632.
(228) Kim, H.; Yang, D. S.; Um, J. H.; Balasubramanian, M.; Yoo, J.; Kim, H.; Park, S. Bin; Kim, J. M.; Yoon, W. S. Comparative Study of Bulk and Nano-Structured Mesoporous SnO 2 Electrodes on the Electrochemical Performances for next Generation Li Rechargeable Batteries. *J. Power Sources* **2019**, *413* (June 2018), 241–249.
(229) Wang, Y.; Li, H.; He, P.; Hosono, E.; Zhou, H. Nano Active Materials for Lithium-Ion Batteries. *Nanoscale* **2010**, *2* (8), 1294.
(230) Li, A.; He, R.; Bian, Z.; Song, H.; Chen, X.; Zhou, J. Enhanced Lithium Storage Performance of Hierarchical CuO Nanomaterials with Surface Fractal Characteristics. *Appl. Surf. Sci.* **2018**, *443*, 382–388.
(231) Ge, H.; Hao, T.; Zhang, B.; Chen, L.; Cui, L.; Song, X. M. Nanoparticles-Constructed Spinel Li4Ti5O12 with Extra Surface Lithium Storage Capability towards Advanced Lithium-Ion Batteries. *Electrochim. Acta* **2016**, *211*, 119–125.
(232) Chen, L.; Jiang, X.; Wang, N.; Yue, J.; Qian, Y.; Yang, J. Surface-Amorphous and Oxygen-Deficient Li3VO4−δ as a Promising Anode Material for Lithium-Ion Batteries. *Adv. Sci.* **2015**, *2* (9), 2–6.
(233) Yan, Y.; Hao, B.; Wang, D.; Chen, G.; Markweg, E.; Albrecht, A.; Schaaf, P. Understanding the Fast Lithium Storage Performance of Hydrogenated TiO 2 Nanoparticles. *J. Mater. Chem. A* **2013**, *1* (46), 14507–14513.
(234) Kavan, L.; Kalbáč, M.; Zukalová, M.; Exnar, I.; Lorenzen, V.; Nesper, R.; Graetzel, M. Lithium Storage in Nanostructured TiO2 Made by Hydrothermal Growth. *Chem. Mater.* **2004**, *16* (3), 477–485.
(235) Liu, D.; Zhang, Y.; Xiao, P.; Garcia, B. B.; Zhang, Q.; Zhou, X.; Jeong, Y. H.; Cao, G. TiO 2 Nanotube Arrays Annealed in CO Exhibiting High Performance for Lithium Ion Intercalation. *Electrochim. Acta* **2009**, *54* (27), 6816–6820.
(236) Lai, C.; Dou, Y. Y.; Li, X.; Gao, X. P. Improvement of the High Rate Capability of Hierarchical Structured Li4Ti5O12 Induced by the Pseudocapacitive Effect. *J. Power Sources* **2010**, *195* (11), 3676–3679.
(237) Ge, H.; Chen, L.; Yuan, W.; Zhang, Y.; Fan, Q.; Osgood, H.; Matera, D.; Song, X. M.; Wu, G. Unique Mesoporous Spinel Li<inf>4</Inf>Ti<inf>5</Inf>O<inf>12</Inf> Nanosheets as Anode Materials for Lithium-Ion Batteries. *J. Power Sources* **2015**, *297*, 436–441.
(238) Wagemaker, M.; Borghols, W. J. H.; Mulder, F. M. Large Impact of Particle Size on Insertion Reactions. A Case for Anatase Li $_x$ TiO $_2$. *J. Am. Chem. Soc.* **2007**, *129* (14), 4323–4327.
(239) Wagemaker, M.; Mulder, F. M. Properties and Promises of Nanosized Insertion Materials for Li-Ion Batteries. *Acc. Chem. Res.* **2013**, *46* (5), 1206–1215.
(240) Borghols, W. J. H.; Wagemaker, M.; Lafont, U.; Kelder, E. M.; Mulder, F. M. Size Effects in the Li 4+ x Ti 5 O 12 Spinel. *J. Am. Chem. Soc.* **2009**, *131* (49), 17786–17792.
(241) Xu, H.; Chen, J.; Li, Y.; Guo, X.; Shen, Y.; Wang, D.; Zhang, Y.; Wang, Z. Fabrication of Li 4 Ti 5 O 12 -TiO 2 Nanosheets with Structural Defects as High-Rate and Long-Life Anodes for Lithium-Ion Batteries. *Sci. Rep.* **2017**, *7* (1), 1–10.
(242) Kavan, L.; Procházka, J.; Spitler, T. M.; Kalbáč, M.; Zukalová, M.; Drezen, T.; Grätzel, M. Li Insertion into Li[Sub 4]Ti[Sub 5]O[Sub 12] (Spinel). *J. Electrochem. Soc.* **2003**, *150* (7), A1000.
(243) Ge, H.; Li, N.; Li, D.; Dai, C.; Wang, D. Electrochemical Characteristics of Spinel Li4Ti5O12 Discharged to 0.01V. *Electrochem. commun.* **2008**, *10* (5), 719–722.
(244) Wang, F.; Wu, L.; Ma, C.; Su, D.; Zhu, Y.; Graetz, J. Excess Lithium Storage and Charge Compensation in Nanoscale Li 4+xTi5O12. *Nanotechnology* **2013**, *24* (42).
(245) Beaulieu, L. Y.; Larcher, D.; Dunlap, R. A.; Dahn, J. R. Reaction of Li with Grain-Boundary Atoms in Nanostructured Compounds. *J. Electrochem. Soc.* **2000**, *147* (9), 3206.
(246) Ku, J. H.; Ryu, J. H.; Kim, S. H.; Han, O. H.; Oh, S. M. Reversible Lithium Storage with High Mobility at Structural Defects in Amorphous Molybdenum Dioxide Electrode. *Adv. Funct. Mater.* **2012**, *22* (17), 3658–3664.
(247) Chae, O. B.; Kim, J.; Park, I.; Jeong, H.; Ku, J. H.; Ryu, J. H.; Kang, K.; Oh, S. M. Reversible Lithium Storage at Highly Populated Vacant Sites in an Amorphous Vanadium Pentoxide Electrode. *Chem.*

Mater. **2014**, *26* (20), 5874–5881.
(248) Guo, B.; Fang, X.; Li, B.; Shi, Y.; Ouyang, C.; Hu, Y. S.; Wang, Z.; Stucky, G. D.; Chen, L. Synthesis and Lithium Storage Mechanism of Ultrafine MoO 2 Nanorods. *Chem. Mater.* **2012**, *24* (3), 457–463.
(249) Tang, W.; Peng, C. X.; Nai, C. T.; Su, J.; Liu, Y. P.; Reddy, M. V. V.; Lin, M.; Loh, K. P. Ultrahigh Capacity Due to Multi-Electron Conversion Reaction in Reduced Graphene Oxide-Wrapped MoO<inf>2</Inf> Porous Nanobelts. *Small* **2015**, *11* (20), 2446–2453.
(250) Schipper, F.; Erickson, E. M.; Erk, C.; Shin, J.-Y.; Chesneau, F. F.; Aurbach, D. Review—Recent Advances and Remaining Challenges for Lithium Ion Battery Cathodes. *J. Electrochem. Soc.* **2017**, *164* (1), A6220–A6228.
(251) Vetter, J.; Novák, P.; Wagner, M. R.; Veit, C.; Möller, K.-C.; Besenhard, J. O.; Winter, M.; Wohlfahrt-Mehrens, M.; Vogler, C.; Hammouche, A. Ageing Mechanisms in Lithium-Ion Batteries. *J. Power Sources* **2005**, *147* (1–2), 269–281.
(252) Luo, J.; Liu, J.; Zeng, Z.; Ng, C. F.; Ma, L.; Zhang, H.; Lin, J.; Shen, Z.; Fan, H. J. Three-Dimensional Graphene Foam Supported Fe 3 O 4 Lithium Battery Anodes with Long Cycle Life and High Rate Capability. *Nano Lett.* **2013**, *13* (12), 6136–6143.
(253) Palanisamy, K.; Kim, Y.; Kim, H.; Kim, J. M.; Yoon, W.-S. Self-Assembled Porous MoO2/Graphene Microspheres towards High Performance Anodes for Lithium Ion Batteries. *J. Power Sources* **2015**, *275*, 351–361.
(254) Wang, X.; Wang, H.; Li, Q.; Li, H.; Xu, J.; Zhao, G.; Li, H.; Guo, P.; Li, S.; Sun, Y. K. Antimony Selenide Nanorods Decorated on Reduced Graphene Oxide with Excellent Electrochemical Properties for Li-Ion Batteries. *J. Electrochem. Soc.* **2017**, *164* (13), A2922–A2929.
(255) Lian, Q.; Zhou, G.; Liu, J.; Wu, C.; Wei, W.; Chen, L.; Li, C. Extrinsic Pseudocapacitve Li-Ion Storage of SnS Anode via Lithiation-Induced Structural Optimization on Cycling. *J. Power Sources* **2017**, *366*, 1–8.
(256) Su, P.; Liao, S.; Rong, F.; Wang, F.; Chen, J.; Li, C.; Yang, Q. Enhanced Lithium Storage Capacity of Co3O4 Hexagonal Nanorings Derived from Co-Based Metal Organic Frameworks. *J. Mater. Chem. A* **2014**, *2* (41), 17408–17414.
(257) Sun, H.; Xin, G.; Hu, T.; Yu, M.; Shao, D.; Sun, X.; Lian, J. High-Rate Lithiation-Induced Reactivation of Mesoporous Hollow Spheres for Long-Lived Lithium-Ion Batteries. *Nat. Commun.* **2014**, *5*, 1–8.
(258) Huang, Y.; Xu, Z.; Mai, J.; Lau, T. K.; Lu, X.; Hsu, Y. J.; Chen, Y.; Lee, A. C.; Hou, Y.; Meng, Y. S.; et al. Revisiting the Origin of Cycling Enhanced Capacity of Fe 3 O 4 Based Nanostructured Electrode for Lithium Ion Batteries. *Nano Energy* **2017**, *41* (July), 426–433.
(259) Larcher, D.; Sudant, G.; Leriche, J.-B.; Chabre, Y.; Tarascon, J.-M. The Electrochemical Reduction of Co[Sub 3]O[Sub 4] in a Lithium Cell. *J. Electrochem. Soc.* **2002**, *149* (3), A234.
(260) Larcher, D.; Masquelier, C.; Bonnin, D.; Chabre, Y.; Masson, V.; Leriche, J.-B.; Tarascon, J.-M. Effect of Particle Size on Lithium Intercalation into α-Fe[Sub 2]O[Sub 3]. *J. Electrochem. Soc.* **2003**, *150* (1), A133.
(261) Yao, H. R.; Yin, Y. X.; Guo, Y. G. Size Effects in Lithium Ion Batteries. *Chinese Phys. B* **2015**, *25* (1), 1–7.
(262) Dylla, A. G.; Henkelman, G.; Stevenson, K. J. Lithium Insertion in Nanostructured TiO2(B) Architectures. *Acc. Chem. Res.* **2013**, *46* (5), 1104–1112.
(263) Lv, X.; Deng, J.; Wang, B.; Zhong, J.; Sham, T. K.; Sun, X.; Sun, X. γ-Fe2O3@CNTs Anode Materials for Lithium Ion Batteries Investigated by Electron Energy Loss Spectroscopy. *Chem. Mater.* **2017**, *29* (8), 3499–3506.
(264) Chu, Y.; Guo, L.; Xi, B.; Feng, Z.; Wu, F.; Lin, Y.; Liu, J.; Sun, D.; Feng, J.; Qian, Y.; et al. Embedding MnO@Mn3O4 Nanoparticles in an N-Doped-Carbon Framework Derived from Mn-Organic Clusters for Efficient Lithium Storage. *Adv. Mater.* **2018**, *30* (6), 1–12.
(265) Jiang, Y.; Yue, J. L.; Guo, Q.; Xia, Q.; Zhou, C.; Feng, T.; Xu, J.; Xia, H. Highly Porous Mn3O4Micro/Nanocuboids with In Situ Coated Carbon as Advanced Anode Material for Lithium-Ion Batteries. *Small* **2018**, *14* (19), 1–9.
(266) Li, S.; Zhao, Y.; Liu, Z.; Yang, L.; Zhang, J.; Wang, M.; Che, R. Flexible Graphene-Wrapped Carbon Nanotube/Graphene@MnO23D Multilevel Porous Film for High-Performance Lithium-Ion Batteries. *Small* **2018**, *14* (32), 1–12.
(267) Li, X.; Zhang, Z.; Liu, C.; Lin, Z. Capacity Increase Investigation of Cu2Se Electrode by Using Electrochemical Impedance Spectroscopy. *Front. Chem.* **2018**, *6* (June), 1–7.
(268) Cao, B.; Liu, Z.; Xu, C.; Huang, J.; Fang, H.; Chen, Y. High-Rate-Induced Capacity Evolution of Mesoporous C@SnO 2 @C Hollow Nanospheres for Ultra-Long Cycle Lithium-Ion Batteries. *J. Power Sources* **2019**, *414* (November 2018), 233–241.
(269) Zhang, Q.; Pei, J.; Chen, G.; Bie, C.; Sun, J.; Liu, J. Porous Co 3 V 2 O 8 Nanosheets with Ultrahigh

Performance as Anode Materials for Lithium Ion Batteries. *Adv. Mater. Interfaces* **2017**, *4* (13), 1–7.
(270) Zhang, Z.; Li, W.; Ng, T.-W.; Kang, W.; Lee, C.-S.; Zhang, W. Iron(<scp>ii</Scp>) Molybdate (FeMoO $_4$) Nanorods as a High-Performance Anode for Lithium Ion Batteries: Structural and Chemical Evolution upon Cycling. *J. Mater. Chem. A* **2015**, *3* (41), 20527–20534.
(271) Maier, J. Nanoionics: Ion Transport and Electrochemical Storage in Confined Systems. *Nat. Mater.* **2005**, *4* (11), 805–815.
(272) Lim, J.; Um, J. H.; Lee, K. J.; Yu, S. H.; Kim, Y. J.; Sung, Y. E.; Lee, J. K. Simple Size Control of TiO 2 Nanoparticles and Their Electrochemical Performance: Emphasizing the Contribution of the Surface Area to Lithium Storage at High-Rates. *Nanoscale* **2016**, *8* (10), 5688–5695.
(273) Lee, D. H.; Lee, B. H.; Sinha, A. K.; Park, J. H.; Kim, M. S.; Park, J.; Shin, H.; Lee, K. S.; Sung, Y. E.; Hyeon, T. Engineering Titanium Dioxide Nanostructures for Enhanced Lithium-Ion Storage. *J. Am. Chem. Soc.* **2018**, *140* (48), 16676–16684.
(274) Sudant, G.; Baudrin, E.; Larcher, D.; Tarascon, J. M. Electrochemical Lithium Reactivity with Nanotextured Anatase-Type TiO 2. *J. Mater. Chem.* **2005**, *15* (12), 1263–1269.
(275) Baudrin, E.; Cassaignon, S.; Koelsch, M.; Jolivet, J. P.; Dupont, L.; Tarascon, J. M. Structural Evolution during the Reaction of Li with Nano-Sized Rutile Type TiO2 at Room Temperature. *Electrochem. commun.* **2007**, *9* (2), 337–342.
(276) Rai, A. K.; Anh, L. T.; Gim, J.; Mathew, V.; Kang, J.; Paul, B. J.; Song, J.; Kim, J. Simple Synthesis and Particle Size Effects of TiO 2 Nanoparticle Anodes for Rechargeable Lithium Ion Batteries. *Electrochim. Acta* **2013**, *90*, 112–118.
(277) Hu, R.; Ouyang, Y.; Zhu, M.; Chen, D.; Waller, G.; Chen, Y.; Zhao, B.; Rainwater, B.; Liu, M.; Yang, C. Dramatically Enhanced Reversibility of Li2O in SnO2-Based Electrodes: The Effect of Nanostructure on High Initial Reversible Capacity. *Energy Environ. Sci.* **2016**, *9* (2), 595–603.
(278) Yang, C.; Liu, X.; Yang, Z.; Gu, L.; Yu, Y. Improvement of Lithium Storage Performance of Molybdenum Trioxide by a Synergistic Effect of Surface Coating and Oxygen Vacancies. *Adv. Mater. Interfaces* **2016**, *3* (22), 1–10.
(279) Wang, Y.; Xiao, X.; Li, Q.; Pang, H. Synthesis and Progress of New Oxygen-Vacant Electrode Materials for High-Energy Rechargeable Battery Applications. *Small* **2018**, *14* (41), 1–23.
(280) Zhu, J.; Chen, J.; Xu, H.; Sun, S.; Xu, Y.; Zhou, M.; Gao, X.; Sun, Z. Plasma-Introduced Oxygen Defects Confined in Li 4 Ti 5 O 12 Nanosheets for Boosting Lithium-Ion Diffusion. *ACS Appl. Mater. Interfaces* **2019**, *11* (19), 17384–17392.
(281) Shin, J. Y.; Joo, J. H.; Samuelis, D.; Maier, J. Oxygen-Deficient TiO 2-δ Nanoparticles via Hydrogen Reduction for High Rate Capability Lithium Batteries. *Chem. Mater.* **2012**, *24* (3), 543–551.
(282) Cao, Z.; Chen, X.; Xing, L.; Liao, Y.; Xu, M.; Li, X.; Liu, X.; Li, W. Nano-MnO2@TiO2 Microspheres: A Novel Structure and Excellent Performance as Anode of Lithium-Ion Batteries. *J. Power Sources* **2018**, *379* (February), 174–181.
(283) Wang, S.; He, M.; Walter, M.; Krumeich, F.; Kravchyk, K. V.; Kovalenko, M. V. Monodisperse CoSn2 and FeSn2 Nanocrystals as High-Performance Anode Materials for Lithium-Ion Batteries. *Nanoscale* **2018**, *10* (15), 6827–6831.
(284) Tang, X.; Huang, X.; Huang, Y.; Gou, Y.; Pastore, J.; Yang, Y.; Xiong, Y.; Qian, J.; Brock, J. D.; Lu, J.; et al. High-Performance Ga2O3 Anode for Lithium-Ion Batteries. *ACS Appl. Mater. Interfaces* **2018**, *10* (6), 5519–5526.
(285) Cherian, C. T.; Sundaramurthy, J.; Reddy, M. V.; Suresh Kumar, P.; Mani, K.; Pliszka, D.; Sow, C. H.; Ramakrishna, S.; Chowdari, B. V. R. Morphologically Robust NiFe2O4 Nanofibers as High Capacity Li-Ion Battery Anode Material. *ACS Appl. Mater. Interfaces* **2013**, *5* (20), 9957–9963.
(286) I. A. Courtney, J. R. D. Electrochemical and In Situ X-Ray Diffraction Studies of the Reaction of Uthium with Tin Oxide Composites. *J. Electrochem. Soc.* **1997**, *144* (6), 2045–2052.
(287) Courtney, I. A. Key Factors Controlling the Reversibility of the Reaction of Lithium with SnO[Sub 2] and Sn[Sub 2]BPO[Sub 6] Glass. *J. Electrochem. Soc.* **1997**, *144* (9), 2943.
(288) Brousse, T. Thin-Film Crystalline SnO[Sub 2]-Lithium Electrodes. *J. Electrochem. Soc.* **1998**, *145* (1), 1.
(289) Demir-Cakan, R.; Hu, Y.; Antonietti, M.; Maier, J.; Titirici, M. Facile One-Pot Synthesis of Mesoporous SnO 2 Microspheres via Nanoparticles Assembly and Lithium Storage Properties. *Chem. Mater.* **2008**, *20* (4), 1227–1229.
(290) Kim, H.; Park, G. O.; Kim, Y.; Muhammad, S.; Yoo, J.; Yoon, W.-S.; Balasubramanian, M.; Cho, Y.-H.; Kim, M.-G.; Lee, B.; et al. New Insight into the Reaction Mechanism for Exceptional Capacity of Ordered Mesoporous SnO2 Electrodes via Synchrotron-Based X-Ray Analysis. *Chem. Mater.* **2014**, *26* (22), 6361–6370.
(291) Cheng, M. Y.; Ye, Y. S.; Chiu, T. M.; Pan, C. J.; Hwang, B. J. Size Effect of Nickel Oxide for Lithium

Ion Battery Anode. *J. Power Sources* **2014**, *253*, 27–34.
(292) Borghols, W. J. H.; Wagemaker, M.; Lafont, U.; Kelder, E. M.; Mulder, F. M. Impact of Nanosizing on Lithiated Rutile TiO2. *Chem. Mater.* **2008**, *20* (9), 2949–2955.
(293) Armstrong, G.; Armstrong, A. R.; Canales, J.; Bruce, P. G. TiO[Sub 2](B) Nanotubes as Negative Electrodes for Rechargeable Lithium Batteries. *Electrochem. Solid-State Lett.* **2006**, *9* (3), A139.
(294) Brutti, S.; Gentili, V.; Menard, H.; Scrosati, B.; Bruce, P. G. TiO 2-(B) Nanotubes as Anodes for Lithium Batteries: Origin and Mitigation of Irreversible Capacity. *Adv. Energy Mater.* **2012**, *2* (3), 322–327.
(295) Pan, D.; Wan, N.; Ren, Y.; Zhang, W.; Lu, X.; Wang, Y.; Hu, Y. S.; Bai, Y. Enhanced Structural and Electrochemical Stability of Self-Similar Rice-Shaped SnO2 Nanoparticles. *ACS Appl. Mater. Interfaces* **2017**, *9* (11), 9747–9755.
(296) Dixon, D.; Ávila, M.; Ehrenberg, H.; Bhaskar, A. Difference in Electrochemical Mechanism of SnO2 Conversion in Lithium-Ion and Sodium-Ion Batteries: Combined in Operando and Ex Situ XAS Investigations. *ACS Omega* **2019**, *4* (6), 9731–9738.
(297) Huie, M. M.; Bock, D. C.; Bruck, A. M.; Tallman, K. R.; Housel, L. M.; Wang, L.; Thieme, J.; Takeuchi, K. J.; Takeuchi, E. S.; Marschilok, A. C. Isothermal Microcalorimetry: Insight into the Impact of Crystallite Size and Agglomeration on the Lithiation of Magnetite, Fe 3 O 4. *ACS Appl. Mater. Interfaces* **2019**, *11* (7), 7074–7086.
(298) C. T. Kresge; M. E. Leonowicz; W. J. Roth; J. C. Vartuli; J. S. Beck. Ordered Mesoporous Molecular Sieves Synthesized by a Liquid-Crystal Template Mechanism. *Nature* **1992**, *359* (22), 710–712.
(299) Zhang, Z.; Zhou, Z.; Nie, S.; Wang, H.; Peng, H.; Li, G.; Chen, K. Flower-like Hydrogenated TiO2(B) Nanostructures as Anode Materials for High-Performance Lithium Ion Batteries. *J. Power Sources* **2014**, *267*, 388–393.
(300) Li, N.; Du, K.; Liu, G.; Xie, Y.; Zhou, G.; Zhu, J.; Li, F.; Cheng, H. M. Effects of Oxygen Vacancies on the Electrochemical Performance of Tin Oxide. *J. Mater. Chem. A* **2013**, *1* (5), 1536–1539.
(301) Meduri, P.; Clark, E.; Kim, J. H.; Dayalan, E.; Sumanasekera, G. U.; Sunkara, M. K. MoO 3-x Nanowire Arrays as Stable and High-Capacity Anodes for Lithium Ion Batteries. *Nano Lett.* **2012**, *12* (4), 1784–1788.
(302) Deng, X.; Wei, Z.; Cui, C.; Liu, Q.; Wang, C.; Ma, J. Oxygen-Deficient Anatase TiO2@C Nanospindles with Pseudocapacitive Contribution for Enhancing Lithium Storage. *J. Mater. Chem. A* **2018**, *6* (9), 4013–4022.
(303) Zou, Y.; Zhang, W.; Chen, N.; Chen, S.; Xu, W.; Cai, R.; Brown, C. L.; Yang, D.; Yao, X. Generating Oxygen Vacancies in MnO Hexagonal Sheets for Ultralong Life Lithium Storage with High Capacity. *ACS Nano* **2019**, *13* (2), 2062–2071.
(304) Su, L.; Zhou, Z.; Shen, P. Ni/C Hierarchical Nanostructures with Ni Nanoparticles Highly Dispersed in N-Containing Carbon Nanosheets: Origin of Li Storage Capacity. *J. Phys. Chem. C* **2012**, *116* (45), 23974–23980.
(305) Zhao, S.; Wang, Y.; Liu, R.; Yu, Y.; Wei, S.; Yu, F.; Shen, Q. Full-Molar-Ratio Synthesis and Enhanced Lithium Storage Properties of Co<inf>x</Inf>Fe<inf>1-X</Inf>CO<inf>3</Inf> Composites with an Integrated Lattice Structure and an Atomic-Scale Synergistic Effect. *J. Mater. Chem. A* **2015**, *3* (33), 17181–17189.
(306) Zhang, R.; Huang, X.; Wang, D.; Hoang, T. K. A.; Yang, Y.; Duan, X.; Chen, P.; Qin, L. C.; Wen, G. Single-Phase Mixed Transition Metal Carbonate Encapsulated by Graphene: Facile Synthesis and Improved Lithium Storage Properties. *Adv. Funct. Mater.* **2018**, *28* (10), 1–11.
(307) Shi, L.; Chen, Y.; He, R.; Chen, X.; Song, H. Graphene-Wrapped CoNi-Layered Double Hydroxide Microspheres as a New Anode Material for Lithium-Ion Batteries. *Phys. Chem. Chem. Phys.* **2018**, *20* (24), 16437–16443.
(308) Wang, Y.; Huang, Z. X.; Shi, Y.; Wong, J. I.; Ding, M.; Yang, H. Y. Designed Hybrid Nanostructure with Catalytic Effect: Beyond the Theoretical Capacity of SnO2 Anode Material for Lithium Ion Batteries. *Sci. Rep.* **2015**, *5* (1), 9164.
(309) Kim, C. H.; Jung, Y. S.; Lee, K. T.; Ku, J. H.; Oh, S. M. The Role of in Situ Generated Nano-Sized Metal Particles on the Coulombic Efficiency of MGeO3(M = Cu, Fe, and Co) Electrodes. *Electrochim. Acta* **2009**, *54* (18), 4371–4377.
(310) Guo, Z. P.; Liu, H. K.; Cho, J.; Seng, K. H.; Park, M. Catalytic Role of Ge in Highly Reversible GeO 2 /Ge/C Nanocomposite Anode Material for Lithium Batteries . *Nano Lett.* **2013**, *13* (3), 1230–1236.
(311) Wan, N.; Lu, X.; Wang, Y.; Zhang, W.; Bai, Y.; Hu, Y.-S.; Dai, S. Improved Li Storage Performance in SnO2 Nanocrystals by a Synergetic Doping. *Sci. Rep.* **2016**, *6* (1), 18978.
(312) Um, J. H.; Park, H.; Cho, Y.-H.; Glazer, M. P. B.; Dunand, D. C.; Choe, H.; Sung, Y.-E. 3D Interconnected SnO 2 -Coated Cu Foam as a High-Performance Anode for Lithium-Ion Battery

Applications. *RSC Adv.* **2014**, *4* (101), 58059–58063.
(313) Um, J. H.; Choi, M.; Park, H.; Cho, Y.-H.; Dunand, D. C.; Choe, H.; Sung, Y.-E. 3D Macroporous Electrode and High-Performance in Lithium-Ion Batteries Using SnO2 Coated on Cu Foam. *Sci. Rep.* **2016**, *6* (1), 18626.
(314) Zhang, H.; Yu, X.; Braun, P. V. Three-Dimensional Bicontinuous Ultrafast-Charge and-Discharge Bulk Battery Electrodes. *Nat. Nanotechnol.* **2011**, *6* (5), 277–281.
(315) Li, X.; Dhanabalan, A.; Gu, L.; Wang, C. Three-Dimensional Porous Core-Shell Sn@carbon Composite Anodes for High-Performance Lithium-Ion Battery Applications. *Adv. Energy Mater.* **2012**, *2* (2), 238–244.
(316) Fu, Y.; Yang, Z.; Li, X.; Wang, X.; Liu, D.; Hu, D.; Qiao, L.; He, D. Template-Free Synthesized Ni Nanofoams as Nanostructured Current Collectors for High-Performance Electrodes in Lithium Ion Batteries. *J. Mater. Chem. A* **2013**, *1* (34), 10002–10007.
(317) Chen, J. S.; Lou, X. W. SnO2-Based Nanomaterials: Synthesis and Application in Lithium-Ion Batteries. *Small* **2013**, *9* (11), 1877–1893.
(318) Wang, Z.; Zhou, L.; Lou, X. W. Metal Oxide Hollow Nanostructures for Lithium-Ion Batteries. *Adv. Mater.* **2012**, *24* (14), 1903–1911.
(319) Cui, G.; Hu, Y. S.; Zhi, L.; Wu, D.; Lieberwirth, I.; Maier, J.; Müllen, K. A One-Step Approach towards Carbon-Encapsulated Hollow Tin Nanoparticles and Their Application in Lithium Batteries. *Small* **2007**, *3* (12), 2066–2069.
(320) Wu, Z. S.; Zhou, G.; Yin, L. C.; Ren, W.; Li, F.; Cheng, H. M. Graphene/Metal Oxide Composite Electrode Materials for Energy Storage. *Nano Energy* **2012**, *1* (1), 107–131.
(321) Chang, P. Y.; Huang, C. H.; Doong, R. A. Ordered Mesoporous Carbon-TiO 2 Materials for Improved Electrochemical Performance of Lithium Ion Battery. *Carbon N. Y.* **2012**, *50* (11), 4259–4268.
(322) Zhang, L.; Wu, H. Bin; Yan, Y.; Wang, X.; Lou, X. W. Hierarchical MoS 2 Microboxes Constructed by Nanosheets with Enhanced Electrochemical Properties for Lithium Storage and Water Splitting. *Energy Environ. Sci.* **2014**, *7* (10), 3302–3306.
(323) Liu, H.; Su, D.; Zhou, R.; Sun, B.; Wang, G.; Qiao, S. Z. Highly Ordered Mesoporous MOS2 with Expanded Spacing of the (002) Crystal Plane for Ultrafast Lithium Ion Storage. *Adv. Energy Mater.* **2012**, *2* (8), 970–975.
(324) Hwang, H.; Kim, H.; Cho, J. MoS2 Nanoplates Consisting of Disordered Graphene-like Layers for High Rate Lithium Battery Anode Materials. *Nano Lett.* **2011**, *11* (11), 4826–4830.
(325) Wang, P. P.; Sun, H.; Ji, Y.; Li, W.; Wang, X. Three-Dimensional Assembly of Single-Layered Mos2. *Adv. Mater.* **2014**, *26* (6), 964–969.
(326) Zhou, G.; Wang, D. W.; Yin, L. C.; Li, N.; Li, F.; Cheng, H. M. Oxygen Bridges between Nio Nanosheets and Graphene for Improvement of Lithium Storage. *ACS Nano* **2012**, *6* (4), 3214–3223.
(327) Shan, X.-Y.; Zhou, G.; Yin, L.-C.; Yu, W.-J.; Li, F.; Cheng, H.-M. Visualizing the Roles of Graphene for Excellent Lithium Storage. *J. Mater. Chem. A* **2014**, *2* (42), 17808–17814.
(328) Radich, J. G.; Kamat, P. V. Origin of Reduced Graphene Oxide Enhancements in Electrochemical Energy Storage. *ACS Catal.* **2012**, *2* (5), 807–816.
(329) Miao, L.; Wu, J.; Jiang, J.; Liang, P. First-Principles Study on the Synergistic Mechanism of SnO 2 and Graphene As a Lithium Ion Battery Anode. *J. Phys. Chem. C* **2013**, *117*, 23–27.
(330) Zhu, X.; Zhu, Y.; Murali, S.; Stoller, M. D.; Ruoff, R. S. Nanostructured Reduced Graphene Oxide/Fe 2 O 3 Composite As a High-Performance Anode Material for Lithium Ion Batteries. *ACS Nano* **2011**, *5* (4), 3333–3338.